The Electron Distribution in HERA and the Consequences for the H1 Detector after the Luminosity Upgrade

Dissertation
zur Erlangung des Doktorgrades
des Fachbereichs Physik
der Universität Hamburg

vorgelegt von
Atoosa Meseck
aus Teheran

Hamburg
August 2000

Gutachter der Dissertation	:	Prof.Dr. P.Schmüser
		Prof.Dr. W.Bartel
Gutachter der Disputation	:	Prof.Dr. W.Bartel
		Prof.Dr. E.Lohrmann
Datum der Disputation	:	21.09.2000
Dekan des Fachbereichs		
Physik und Vorsitzender		
des Promotionsausschusses	:	Prof.Dr. F.-W.Büßer

Kurzfassung

Die Kollision der beiden Strahlen im HERA-Speicherring wird durch das Hinführen des Elektronstrahls zum Protonstrahl ermöglicht. Dabei entsteht in den dafür nötigen Ablenk- und Fokussierungsmagneten Synchrotronstrahlung.

Um eine Beeinträchtigung der Datennahme und Auswertung der Experimente zu vermeiden, werden die Detektoren mit Hilfe von Kollimatoren, die vor und hinter diesen angebracht sind, vor Synchrotronstrahlung geschützt. Da nach dem Luminositätserhöhungsprojekt eine Kollimation des Synchrotronstrahlungsfächers nach dem heutigen Schema nicht mehr möglich sein wird, müssen die Experimentdetektoren so konstruiert werden, daß der direkte Synchrotronstrahlungsfächer sie ungehindert passieren kann. Ein Teil dieser Arbeit beschäftigt sich mit der Konstruktion eines entsprechenden zentralen Strahlrohrs und eines Kollimationssystems für den H1-Detektor.

Da die Photonen an der Kante des Synchrotronstrahlungsfächers von den Elektronen in den Schwänzen der Elektronenverteilung emittiert werden, ist die Kenntnis der Elektronenverteilung für die Konstruktion des zentralen Strahlrohrs und des Kollimationssytems des H1-Detektors unentbehrlich. Die Untersuchung der Schwänze der Elektronenverteilung ist ein weiterer Gegenstand dieser Arbeit.

Bei diesen Untersuchungen sind Abtastexperimente an dem Elektronenstrahl für verschiedene Optiken sowohl mit als auch ohne die Strahl-Strahl-Wechsel-wirkung vorgenommen worden. Während der Kern der Verteilung bis ca. sechs Standardabweichungen stets einer Gaußkurve folgte, waren die Schwänze der Verteilung nichtgaußisch. Die Existenz der nichtgaußischen Schwänze konnte zum einen durch analytische Untersuchungen auf Streuprozesse, vor allem an dem Restgas, und zum anderen durch Simulationen auf die nichtlinearen Kräfte zurückgeführt werden.

Abstract

The collision of both beams in the HERA storage ring is performed by the guidance of the electron beam to the proton beam. Thereby synchrotron radiation is generated in the bending and focussing magnets.

In order to avoid a deterioration of the data accumulation by the radiation background, the experiments are protected from the synchrotron radiation by collimators which are installed in front of and behind the detectors. Since after the luminosity upgrade, a collimation of the synchrotron radiation in front of the experiments will no longer be possible, the detectors have to be designed such, that the direct synchrotron radiation fan passes through the detectors. The first part of this thesis is concerned with the design of a suitable central beam pipe and collimation system for the H1 detector.

The photons on the edge of the radiation fan are emitted by the electrons in the tails of the electron distribution. Therefore the knowledge of the electron distribution in HERA is for the design of the central beam pipe and collimation system of H1 detector very important. The investigation of the electron tails in HERA is the second topic of this work.

For these investigations tail scan experiments were carried out with several optics and with and without the beam-beam- interaction. The core of the electron distribution was always a Gaussian until about six standard deviations, whereas the tails were non Gaussian. The non Gaussian tails can be explained by the combined effects of scattering processes and nonlinear forces. The influence of the scattering processes on the electron tails was investigated analytically. Simulation programs were used to investigate the influence of the nonlinear forces on the tails.

Contents

1 Introduction **6**

2 Synchrotron Radiation and Electron Distribution **8**

2.1 Properties of Synchrotron Radiation 9

2.1.1 Radiated Power 9

2.1.2 Radiated Spectrum 10

2.2 Interaction of Synchrotron Radiation with Matter 12

2.2.1 Attenuation Coefficient 13

2.2.2 Photo Electric Effect 13

2.2.3 Compton Effect 15

2.2.4 Pair Production 16

2.3 Electron Distribution 17

2.3.1 Radiation Damping 17

2.3.2 Quantum Excitation 19

2.3.3 Equilibrium Distribution 20

2.3.4 Quantum Lifetime 21

2.4 Scattering processes 21

2.4.1 Touschek Scattering 22

2.4.2 Beam-Gas Scattering 24

2.5 Nonlinear Forces 29

2.5.1 Beam-Beam Interaction 29

2.5.2 Nonlinear Resonances 31

3 HERA and H1 Detector **35**

3.1 The HERA Storage Ring 36

3.2 The H1 Detector 38

3.2.1 Tracking System 38

3.2.2 Calorimetry 40

3.2.3 Central Muon Detector 42
3.3 Synchrotron Radiation Collimation System 43

4 HERA Upgrade Project and the New H1 Detector 45
4.1 Magnet Structure at the H1 Interaction Region 46
4.2 Simulation Program and the Results of the Simulation 48
4.3 The H1 Radiation Shielding 50
4.4 The Contribution of the Tails of the Electron Distribution to the Radiation Fan 52

5 Tail Scan Experiments at the HERA Electron Ring 59
5.1 Measuring Equipment 60
5.1.1 The Scrapers 60
5.1.2 The Beam Lifetime 60
5.1.3 The Beam Loss Monitors 62
5.1.4 Measurement Device 63
5.2 Results and the Measurement Errors 64
5.3 Evaluation 73

6 Estimation of Radiation Background after the Luminosity Upgrade 87
6.1 Electron Distribution 87
6.2 Radiation Background 88

7 Conclusion and Outlook 92

A The Fokker-Planck Equation 94

B Non Gaussian Tails of Electron Distribution 98

C Basic Notions of Accelerator Physics 102

D The Measured Data 104

Chapter 1

Introduction

The electron proton colliding beam facility HERA consists of two independent accelerator rings, an electron and a proton ring which are brought together in two points - interaction points north and south - to allow the collision of the beams. The high beam energies of 27.5 GeV for the electrons and 920 GeV for the protons during the collisions ensure very high center of mass energies, which are required to investigate the high momentum transfer regime of deep inelastic electron proton scattering. These processes are explored by the experiments H1 and ZEUS which are installed in the interaction points north and south.

In order to enhance the number of useful events, the beam induced background at the detectors has to be minimized. A source of the beam induced background is synchrotron radiation which is emitted by electrons in the quadrupoles and bending magnets. In the present HERA configuration, special collimators in front of and behind the detectors shield the experiments from the direct and the backscattered synchrotron radiation.

The rate of events divided by the cross section is called *luminosity*. An increase in HERA luminosity enables the experiments to make sensitive tests for QCD and the Standard Model and to look for new physics beyond the Standard Model. For this reason an upgrade of the HERA storage ring to achieve an increase in luminosity by a factor of 4.7 to about $7 \cdot 10^{31}\, cm^{-2} s^{-1}$ is planned. The increase of the luminosity will be achieved by the reduction of the electron emittance and the beta functions of both beams at the interaction points. In order to reduce the beta functions of both beams, modifications of the magnet structure in the interaction regions are necessary, which have the undesirable consequence that the collimation of the

direct synchrotron radiation in front of the detectors is no longer possible.

In scope of this thesis, the synchrotron radiation in the H1 interaction region after the HERA luminosity upgrade and its consequences for the upgraded H1 detector are investigated by simulation programs. Further a collimation system to shield the detector from the backscattered radiation is designed. The distribution of the electrons in HERA, which emit the synchrotron radiation, is investigated by tail scan experiments.

In the second chapter of this work, the theoretical foundations of synchrotron radiation and electron distribution are discussed. The third chapter discribes the present HERA layout and the H1 detector. The luminosity upgrade and the upgraded H1 detector are the topics of the fourth chapter. The fifth chapter treats the tail scan experiments. The expected radiation background in the H1 detector after the luminosity upgrade is discussed in the sixth chapter. The conclusions and an outlook are the topics of the seventh chapter. A short description of the basic notions of the accelerator physics can be found in the appendix.

Chapter 2

Synchrotron Radiation and Electron Distribution

The electromagnetic radiation emitted by a charged particle beam on a curved trajectory in a circular accelerator is called *synchrotron radiation*. Synchrotron radiation is of major importance in the design of electron synchrotrons and storage rings. The HERA electron ring is an example for such an accelerator.

The emission of synchrotron radiation exerts a strong influence on the electron beam dynamics. The loss of energy due to the emission of synchrotron radiation, and its replacement by the RF cavities, leads to a damping of the oscillations in energy and transverse displacement, a process known as *radiation damping*. The energy is lost in discrete units or *quanta*, i.e. photons, whose energy and time of emission vary randomly. The fluctuation in the emission of synchrotron radiation gives rise to an excitation of the oscillations. This process is called *quantum excitation*.

Not only the influence of synchrotron radiation on the electron beam dynamics but also the background due to the synchrotron radiation in the HERA experiments ZEUS and H1 is a point of interest for the operation of the HERA electron ring. The properties of synchrotron radiation and the interaction of synchrotron radiation with matter are described in the first two section of present chapter. The combined effects of quantum excitation and radiation damping leads to an equilibrium distribution of the electrons. The equilibrium distribution is Gaussian if there is no perturbation due to nonlinear forces and scattering processes. The equilibrium distribution and its perturbation due to nonlinear forces and scattering processes are treated

in the last three sections of this chapter.

2.1 Properties of Synchrotron Radiation

The emission of synchrotron radiation has implications for the design of a circular accelerator. The energy loss due to synchrotron radiation affects the size of the accelerator required to reach a given energy of the stored particle beam as well as the RF system needed to replace the energy loss. In addition the design of the vacuum system must take into account the heat generated and the large amount of gas desorbed when synchrotron radiation impinges on the vacuum chamber walls. The basic properties of synchrotron radiation are treated briefly in this section.

2.1.1 Radiated Power

The instantaneous power radiated by a relativistic electron is given by the Lienard formula [17]:

$$P = \frac{2}{3}\frac{e^2\gamma^6}{4\pi\varepsilon_0 c}(\dot{\vec{\beta}}^2 - (\vec{\beta}\times\dot{\vec{\beta}})^2),$$

where $\vec{\beta}c$ is the velocity, ε_0 is the dielectric constant, e is the electron charge, and $\gamma = \frac{1}{\sqrt{1-\beta^2}}$ is the Lorentz factor.

In the case of circular motion, the instantaneous rate of emitted power is given by:

$$P = \frac{2}{3}\frac{e^2 c\beta^4\gamma^4}{4\pi\varepsilon_0\rho^2}, \tag{2.1}$$

where ρ is the bending radius of the particle trajectory. Integration of the radiated power along the circumference of the accelerator yields the energy loss per turn [3]:

$$U_0 = \oint P\frac{1}{\beta c}ds = \frac{2}{3}\frac{e^2\beta^3\gamma^4}{4\pi\varepsilon_0}\oint\frac{ds}{\rho^2(s)}.$$

For an isomagnetic lattice (uniform bending radius in the bending magnets), which is a good approximation for most of the storage rings, the results simplifies to:

$$U_0 = \frac{e^2\beta^3\gamma^4}{3\epsilon_0\rho}. \tag{2.2}$$

The total power emitted by an electron beam is given by:

$$P_{beam} = U_0 N_e f_{rev} = \frac{U_0 I_{beam}}{e}, \tag{2.3}$$

where N_e is the number of electrons in the beam, f_{rev} is the revolution frequency, and I_{beam} is the beam current.

In order to make up for the losses due to synchrotron radiation the RF system has to provide the total radiated power P_{beam}. Since the total radiated power scales like the fourth power of the beam energy and is inversely proportional to the bending radius, there are practical limitations on the maximum achievable particle energy and on the minimum needed bending radius in a circular accelerator.

2.1.2 Radiated Spectrum

Synchrotron radiation caused by relativistic charged particles is emitted over a wide spectrum of photon energies. The photons are radiated in the forward direction with an rms angle of about $\theta_{rms} \approx \frac{1}{\gamma}$. In the case of a bunched particle beam in a circular accelerator, it appears to an observer as a series of equidistant light flashes as bunches of particles orbit in the accelerator.

As shown in figure 2.1, the synchrotron light flash cannot be observed before it has reached the point p_0, where one edge of the radiation cone at an angle of $-\frac{1}{\gamma}$ appears. And the last visible photons are emitted from the point p_1 at an angle of $\frac{1}{\gamma}$. Accordingly the deflection angle between the point p_0 and the point p_1 amounts to $\frac{2}{\gamma}$.

The duration of the light pulse Δt at the location of the observer is given by [12, 13]:

$$\Delta t = \frac{2\rho}{\beta c}\frac{1}{\gamma} - \frac{2\rho \sin(\frac{1}{\gamma})}{c}. \tag{2.4}$$

The sine function can be expanded for small angles. After some manipulation and with $\beta \approx 1$ one obtains:

$$\Delta t = \frac{4\rho}{3c\gamma^3}. \tag{2.5}$$

The critical frequency of synchrotron radiation

$$\omega_c = \frac{2}{\Delta t} = \frac{3c\gamma^3}{2\rho} \tag{2.6}$$

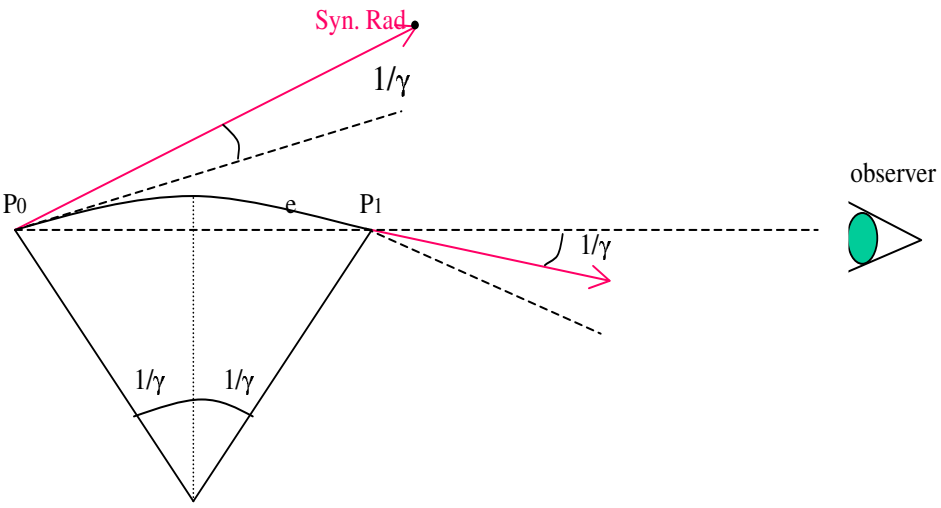

Figure 2.1: *Observed synchrotron radiation*

is a convenient mathematical scaling parameter.

The spectral photon density is given by the Schwinger formula [5]:

$$\frac{d\dot{N}}{d\epsilon/\epsilon} = \frac{P_{beam}}{E_c} S(\xi) \tag{2.7}$$

where $\dot{N}$ is the number of the emitted photons per unit time, ϵ is the energy of the emitted photons, and the function $S(\xi)$ (fig. 2.2) is defined as

$$S(\xi) = \frac{9\sqrt{3}}{8\pi} \xi \int_{\xi}^{\infty} K_{5/3}(x) dx \tag{2.8}$$

where $\xi = \frac{\omega}{\omega_c}$, and $K_{5/3}(x)$ is a modified Bessel function. The function $S(\xi)$ is normalized:

$$\int_0^{\infty} S(\xi) d\xi = 1$$

and integration up to $\xi = 1$, i.e. $\omega = \omega_c$, yields:

$$\int_0^{1} S(\xi) d\xi = \frac{1}{2}.$$

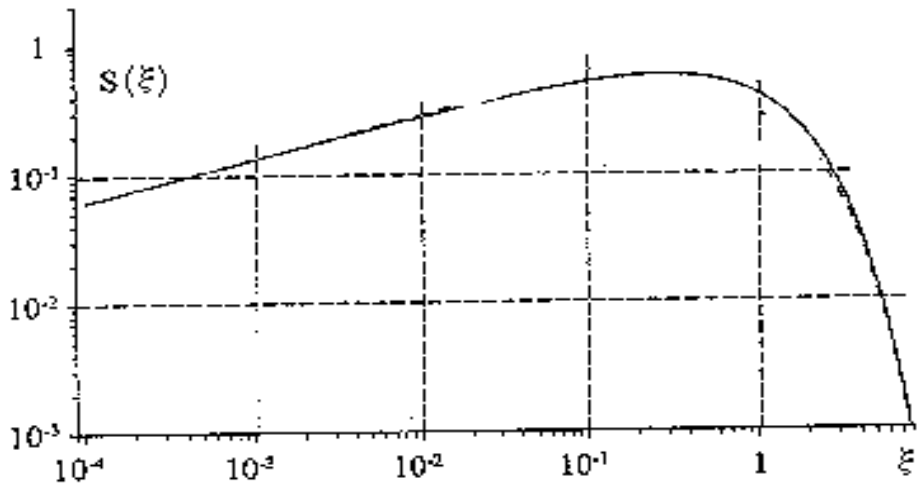

Figure 2.2: *The function* $S(\xi)$.

The above formula implies that the critical frequency ω_c divides the power spectrum into two equal halves. The corresponding critical energy is given by

$$E_c = \hbar\omega_c. \tag{2.9}$$

2.2 Interaction of Synchrotron Radiation with Matter

As mentioned before, the background due to synchrotron radiation in the experiments is of importance for the operation of HERA. At high particle energies it becomes necessary to shield the detectors from the radiation. Therefore a system of absorbers and collimators protects the experiments in HERA.

The interaction of synchrotron radiation with absorber material is treated in the present section. This interaction depends on the energy of synchrotron radiation photons. In the case of photon energies up to 1 MeV, the interaction of photons with matter can be described by two relevant effects : the

Compton scattering and the photo electric effect (see figure 2.3). In the case of photon energies of more than 1 MeV, pair production has to be taken into account as well.

The efficiency of an absorber can be described by the attenuation coefficient of the absorber material.

2.2.1 Attenuation Coefficient

By passing through an absorber, synchrotron radiation suffers an attenuation caused by interactions with the absorber material. The number of remaining photons after passing a distance x in the absorber is given by [18, 19]:

$$N(x) = N_0 \exp(-\mu x)$$

where N_0 is the initial number of photons and μ is the attenuation coefficient of the absorber material. The attenuation coefficient can be obtained as follows:

$$\mu = \mu_P + \mu_C + \mu_F = \sigma_P \cdot n + \sigma_C \cdot n + \sigma_F \cdot n$$

where n is the number of scattering centers per unit volume, μ_P and σ_P are the attenuation coefficient and the cross section of pair production, μ_F and σ_F are the attenuation coefficient and the cross section of the photo electric effect, and μ_C and σ_C are the attenuation coefficient and the cross section of the Compton effect.

The mean free path of a photon in matter τ_μ is defined as:

$$\tau_\mu = \frac{1}{\mu}.$$

2.2.2 Photo Electric Effect

The process in which an atomic electron leaves the electron shell of the atom due to the absorption of a photon is called *photo electric effect.* The kinetic energy of the released electron is given by [19]:

$$E_{el} = E_\gamma - E_B^i, \qquad i = K, L, M$$

where $E_\gamma = h\nu$ is the energy of the absorbed photon, and E_B^i is the binding energy of the electron on the i-th shell.

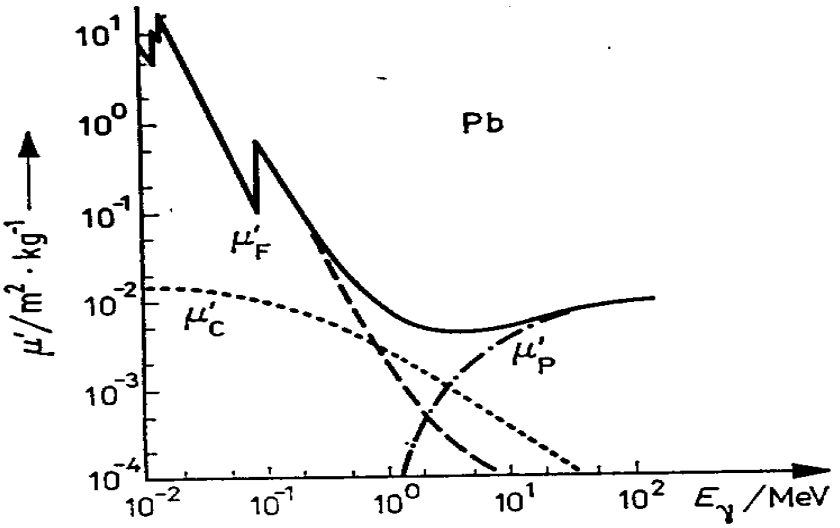

Figure 2.3: *Compton (μ'_C), photo electric (μ'_F), pair production (μ'_P) and total mass attenuation coefficient ($\mu' = \mu/\rho(density)$) of lead as a function of incident photon energy. Since less than 1% of the photons emitted in HERA electron ring have an energy more than 1 MeV, the pair production from synchrotron radiation can be neglected in HERA.*

In Figure 2.4 the photo absorption cross section is shown as a function of the incident photon energy. The cross section has strong maxima for the cases, where the energy of the photon is equal to the binding energy of an electron on the i-th shell ($E_\gamma = E_B^i$). If the energy of the absorbed photon is far away from the binding energy, the photo absorption cross section is given by:

$$\sigma_F = \frac{8\pi r_e^2}{3} 4\sqrt{2} Z^5 \alpha^4 \left(\frac{m_e c^2}{E_\gamma}\right)^{7/2}, \tag{2.10}$$

assuming that $E_\gamma \ll m_e c^2$.
Here m_e is the electron rest mass, Z is the atomic number, $r_e = 2.8179\dot{1}0^{-15}$m is the classical electron radius, and $\alpha = \frac{1}{137.036}$ is the fine-structure constant.

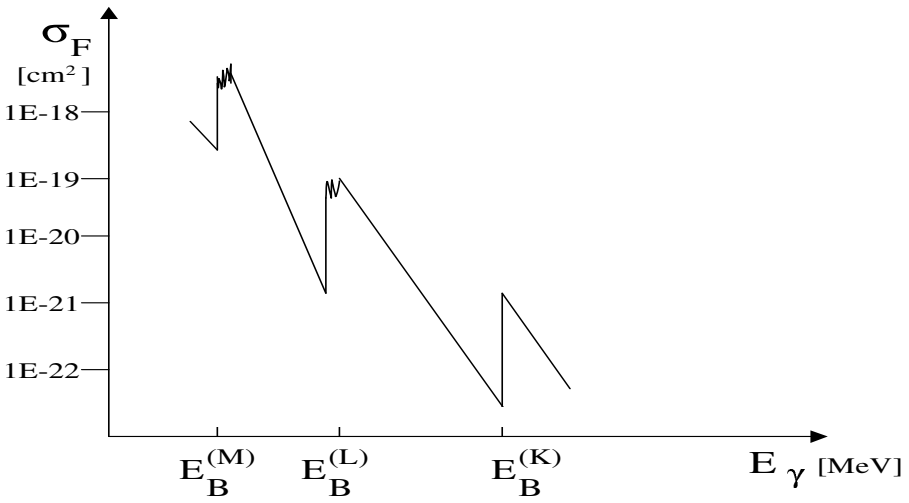

Figure 2.4: *Typical photo absorption cross section as a function of incident photon energy, schematically.*

2.2.3 Compton Effect

The process in which a photon is scattered by a free electron is called *Compton scattering*. At high photon energies, the binding energy of an atomic electron can be ignored, so that the atomic electron can be considered as free and at rest. The energy of a photon after scattering at a free and resting electron is a function of the initial photon energy E_γ and the scattering angle θ [18]:

$$E'_\gamma = \frac{E_\gamma}{1 + \left(\frac{E_\gamma}{m_e c^2}\right)(1 - \cos(\theta))}.$$

The differential cross section of Compton scattering is given by the Klein-Nishina formula [19]:

$$\frac{d\sigma_C}{d\Omega} = \frac{\alpha^2}{2m_e c^2}\left(\frac{E'_\gamma}{E_\gamma}\right)^2\left(\frac{E'_\gamma}{E_\gamma} + \frac{E_\gamma}{E'_\gamma} - \sin(\theta)\right). \tag{2.11}$$

where Ω is the solid angle. For very low photon energy ($E_\gamma \ll m_e c^2$), the

total cross section of Compton scattering is given by:

$$\sigma_C = \frac{8\pi}{3} r_e^2 .$$

At low photon energy ($E_\gamma < m_e c^2$), the total cross section is given by [19]:

$$\sigma_C = \frac{8\pi}{3} r_e^2 Z \left(1 - 2\frac{E_\gamma}{m_e c^2} + \frac{26}{5}\frac{E_\gamma^2}{m_e^2 c^4} + ... \right)$$

If the photon energy is high ($E_\gamma \gg m_e c^2$), the total cross section of Compton scattering is given by:

$$\sigma_C = \pi r_e^2 \frac{m_e c^2}{E_\gamma} \left(\ln\left(\frac{2E_\gamma}{m_e c^2} \right) + \frac{1}{2} \right).$$

At very high photon energies ($E_\gamma \gg 2m_e c^2$) the probability of the Compton effect decreases. In this region pair production is the most relevant effect.

2.2.4 Pair Production

A photon with an energy of more than $2m_e c^2$ can produce an electron-positron pair, supposing that there is a charged particle, e.g. atomic nucleus, to absorb the recoil momentum and energy (which is negligible in most cases):

$$\gamma + A \rightarrow A + e^+ + e^- .$$

Pair production cross section starts at an energy threshold of $E_\gamma = 2m_e c^2$, and increases logarithmically with the photon energy up to energies of $E_\gamma \sim 50 m_e c^2$,

$$\sigma_p \sim Z^2 \ln(E_\gamma). \tag{2.12}$$

For photon energies higher than $50 m_e c^2$, it increases slower and reaches a roughly constant value for $E_\gamma > 10^3 m_e c^2$,

$$\sigma_p \cong 12\alpha Z^2 r_e^2 . \tag{2.13}$$

Only less than 1% of the synchrotron radiation photons emitted in the HERA electron ring have an energy of more than $2m_e c^2$. Therefore the pair production from synchrotron radiation photons is not relevant for the HERA electron ring.

2.3 Electron Distribution

The influence of synchrotron radiation on the electron beam dynamics is an important aspect for the operation of circular electron accelerators. The equilibrium distribution of electrons results from the combined effect of quantum excitation and radiation damping. If the electron distribution reaches the acceptance given by the vacuum chamber walls, the electrons are lost. This leads to a finite lifetime of the beam, which is called *quantum lifetime*. Radiation damping, quantum excitation, and the resulting electron distribution and quantum lifetime are discussed in this section.

2.3.1 Radiation Damping

In a circular accelerator the electrons which are not on the nominal orbit, execute transverse oscillations around it. These oscillations are called *betatron oscillations*. Similarly electrons with energy deviations oscillate under influence of the RF system about the nominal energy. These oscillations are known as *synchrotron oscillations*. Due to the energy loss caused by synchrotron radiation the oscillations can be damped.

In the case of a separated function lattice, where the lattice consists of pure dipoles and quadrupoles, as it is the case in the HERA electron ring, the damping of energy oscillations is due to the fact that the radiated power is energy dependent, i.e. an electron with a higher energy than the nominal energy radiates more and an electron with less energy radiates less. This leads to a reduction, *damping*, of the energy oscillation of the electrons.

An important parameter of the damping of oscillations is the damping decrement. The damping decrement α_s of synchrotron oscillation depends on the change $\frac{\partial U}{\partial E}$ of the energy loss due to synchrotron radiation with the particle energy E [1, 2, 3]:

$$\alpha_s = \frac{1}{2T_0}\left(\frac{\partial U}{\partial E}\right)_{E_0} = \frac{U_0}{2T_0 E_0}(2+\mathcal{D}). \tag{2.14}$$

where T_0 is the revolution time, and E_0 is the nominal energy. The $\mathcal{D}$-parameter depends on the particular lattice and is defined by [12, 13]:

$$\mathcal{D} = \frac{\oint \eta\left(\frac{1}{\rho^3}+\frac{2k}{\rho}\right)ds}{\oint \frac{ds}{\rho^2}} \tag{2.15}$$

where η is the dispersion function, and k is the focusing strength. The first term in the above formula $\frac{\eta}{\rho^3}$ is a consequence of a longer path length in curved systems like sector magnets. For $\rho > 0$ and $\eta > 0$ this term increases the synchrotron oscillation damping, because an electron with a higher energy travels a longer path for positive dispersion and therefore radiates a longer time loosing an extra amount of energy. Conversely an electron with a lower energy than the nominal energy travels a shorter path and looses less energy compared to the electron with the nominal energy. The second term, which is caused by the changes of the magnetic field with the transverse position of the electron beam in the magnet, occurs only for combined function magnets. Such changes do not occur for lattices of pure dipoles and quadrupoles (separated function lattices), so that $|\mathcal{D}| \ll 1$. In a FODO lattice, the dispersion is typically largest in focusing quadrupoles, where $k > 0$, therefore there is an additional damping in this case.

For a separated function lattice like the HERA electron ring, the damping of betatron oscillations is a combined effect of synchrotron radiation emission and the energy replacement by the RF system. The photons of synchrotron radiation are emitted into the direction of the electron motion which has not only longitudinal but also transverse components. Therefore a part of the energy loss is correlated to a loss in transverse momentum. But the restored energy by the accelerating fields has only longitudinal components. This fact gives rise to a loss of transverse momentum on the average, which leads to a reduction in the transverse oscillation amplitude, known as betatron oscillation damping. The damping decrement α_x of horizontal betatron oscillation is given by:

$$\alpha_x = \frac{U_0}{2T_0E_0}(1 - \mathcal{D}). \tag{2.16}$$

Assuming that there is no bending in the vertical plane, the damping decrement of vertical betatron oscillation simplifies to:

$$\alpha_y = \frac{U_0}{2T_0E_0}. \tag{2.17}$$

The sum of all the damping decrements is a constant, a result known as the Robinson theorem:

$$\begin{aligned}\alpha_s + \alpha_x + \alpha_y &= \frac{U_0}{2T_0E_0}((2 + \mathcal{D}) + (1 - \mathcal{D}) + 1) \\ &= \frac{U_0}{2T_0E_0}(J_s + J_x + J_y) = \frac{2U_0}{T_0E_0}\end{aligned}$$

where $J_x = 1 - \mathcal{D}$, $J_y = 1$, $J_s = 2 + \mathcal{D}$ are the damping partition numbers.

The Robinson theorem implies that an additional damping in one plane, e.g. higher J_x, causes less damping, e.g. lower J_s, in another plane. For a separated function lattice, $J_s = 2$, $J_x = 1$, and $J_y = 1$, the betatron oscillations as well as the synchrotron oscillation are damped. The damping time of the oscillations are given by:

$$\tau_i = \frac{1}{\alpha_i}$$

where $i = s, x, y$.

2.3.2 Quantum Excitation

The stochastic emission of photons causes primarily a change of the electron energy leading to an energy spread within the beam. An electron with nominal energy loses energy by the emission of a photon at the time t_0 and starts to oscillate about the nominal energy:

$$\Delta E = \epsilon \cos(\Omega(t - t_0)) \tag{2.18}$$

where ϵ is the photon energy, and Ω is the synchrotron frequency.

The sudden change of electron energy causes a change in the transverse electron motion. The position and the direction of the electron are not changed during the forward emission of the photon (the small transverse perturbation due to the finite opening angle of the radiation of $(\pm\frac{1}{\gamma})$ can be neglected). But particles with different energies travel on different closed orbits, about which the particle oscillate. Two electrons with energies E_0 (nominal energy) and $E = E_0 - \epsilon$ oscillate about two spatially separated closed orbits. The distance between the orbits at the position s is given by:

$$\Delta x = \eta(s)\frac{E_0 - E}{E_0} = \eta(s)\frac{\epsilon}{E_0}. \tag{2.19}$$

The sudden energy change leads to sudden changes in the betatron and synchrotron oscillation amplitudes of the electron. The energy and the time of emission of a photon vary randomly. Therefore the quantum excitation undergoes statistical fluctuation.

The growth of the oscillation amplitudes due to quantum excitation is balanced by radiation damping. In order to obtain the electron distribution a partial differential equation, the so called Fokker-Planck equation, which takes into account the statistical excitation, can be used.

2.3.3 Equilibrium Distribution

In the stationary case, where the damping and excitation of oscillations are in equilibrium, the density distribution ψ of electrons is described by the Fokker-Planck equation in phase space:

$$\frac{\partial\psi}{\partial t} + \omega p\frac{\partial\psi}{\partial q} - (\omega q + 2\alpha p)\frac{\partial\psi}{\partial p} = 2\alpha\psi + D\frac{\partial^2\psi}{\partial p^2} \tag{2.20}$$

where p and q are normalized canonical coordinates, α is the damping decrement, and D is the diffusion coefficient. The stationary solution ψ_0 of the above equation for electrons under the influence of damping and statistical excitation is a Gaussian distribution [10]:

$$\psi_0(q,p) = \frac{\alpha}{\pi D}\exp\left(\frac{-\alpha}{D}(q^2+p^2)\right), \tag{2.21}$$

with a standard width σ of :

$$\sigma = \sqrt{\frac{D}{2\alpha}}.$$

The projection of this electron distribution onto the transverse coordinate axes x and y is a Gaussian too [10, 12, 13]:

$$\psi(z) = \frac{1}{\sqrt{2\pi}\sigma_z}\exp\left(\frac{-z^2}{2\sigma_z^2}\right), \tag{2.22}$$

where $z = x, y$ and

$$\sigma_z = \sqrt{\frac{D\beta_z}{\alpha}} = \sqrt{\beta_z\varepsilon_z},$$

with the beta function β_z, and the emittance ε_z in the horizontal or vertical plane.

The energy distribution becomes with $\delta = \epsilon/E_0$:

$$\psi(\delta) = \frac{1}{\sqrt{2\pi}\sigma_\delta}\exp\left(\frac{-\delta^2}{2\sigma_\delta^2}\right), \tag{2.23}$$

where the standard deviation of the energy spread in the electron beam is defined by:

$$\frac{\sigma_\epsilon}{E_0} = \sqrt{\frac{D_s}{\alpha_s}}.$$

2.3.4 Quantum Lifetime

In a real storage ring one has to consider the presence of vacuum chamber walls, which cut off the Gaussian tails of the particle distribution. Due to quantum excitation, there is a continuous flow of electrons from the core of the distribution into the tails and back by damping towards the core. A reduction of the aperture absorbs therefore not only those electrons which populate these tails at a particular moment but also all electrons which reach occasionally large oscillation amplitudes due to the emission of a high energy photon. The absorption of electrons due to this effect causes a finite beam lifetime, which is called the quantum lifetime. Supposing that the cutting of Gaussian tails at large amplitudes will not affect the core of the Gaussian distribution, for a given aperture limit A the quantum lifetime τ_q is given by [10]:

$$\tau_{qz} = \frac{\sigma_z^2}{\alpha_z} \frac{e^{\frac{A_z^2}{2\sigma_z^2}}}{A_z^2}, \tag{2.24}$$

where $z = x, y$. Figure 2.5 shows the quantum lifetime τ_{qx} as a function of the horizontal aperture for a Gaussian electron distribution.

Other processes which also cause electron losses and therefore limit the beam lifetime are the scattering processes. These processes are treated in the next section.

2.4 Scattering processes

Particles in a bunch circulating in a storage ring experience two fundamentally different scattering processes: scattering between particles inside the bunch and scattering by residual gas, so called *beam-gas scattering*.

The Coulomb scattering inside the bunch leads to immediate loss of both particles involved in the collision, in the case of sufficiently large momentum transfer. This process is known as *Touschek scattering*. In the case of the Coulomb scattering inside the bunch with only small exchange of momentum, the particles are not lost immediately. The particles might experience many such collisions during a damping time. This process is called *intrabeam scattering*. In high energy electron accelerators, like the HERA electron ring, the influence of the intrabeam scattering on the beam lifetime and the particle distribution is negligible.

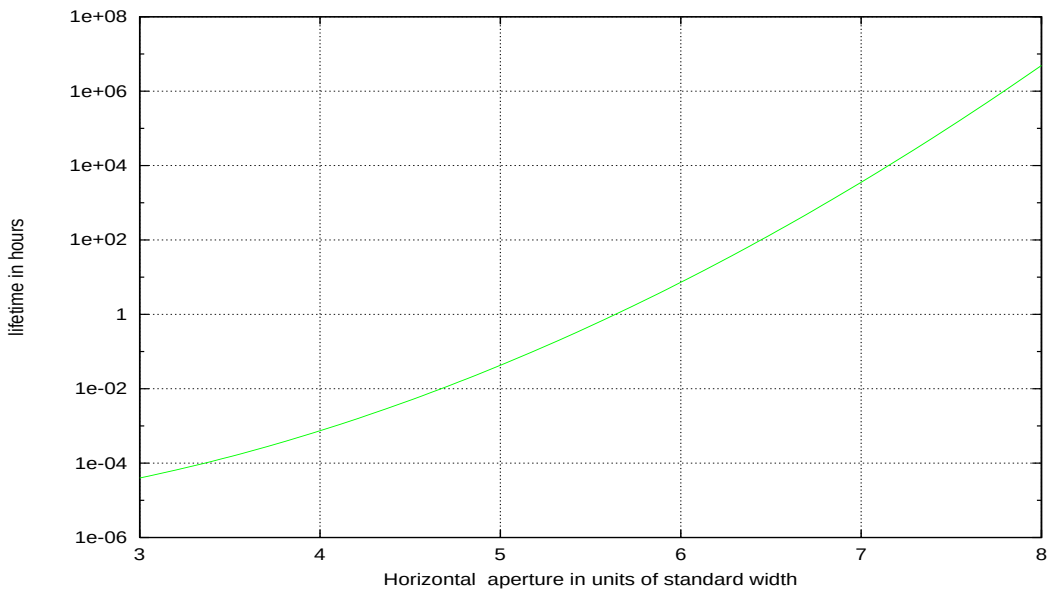

Figure 2.5: *The quantum lifetime in hours versus the horizontal aperture in units of the horizontal standard width in the case of a Gaussian electron distribution*

In this section the Touschek and the beam-gas scattering and their contributions to the beam lifetime and the beam distribution are treated.

2.4.1 Touschek Scattering

Touschek scattering is an elastic scattering process where a large momentum transfer leads to the loss of both colliding particles.

In an accelerator, the particles perform transverse betatron oscillations as well as longitudinal synchrotron oscillations. The collision process during which the two colliding particles perform synchrotron oscillations and collide head-on such that their longitudinal momenta are transferred into transverse momenta can be neglected since the longitudinal motion includes not enough momentum to increase the betatron oscillations amplitude significantly for particle loss, whereas the transverse betatron oscillations include large momenta and a transfer into longitudinal momenta can lead to the loss of both colliding particles. The particles get lost if their longitudinal momenta are outside the momentum acceptance of the accelerator, i.e. if their energy

deviation is larger than the energy acceptance.

The differential cross section for Coulomb scattering of two particles with equal but opposite momenta in the center of mass system is given by [9]:

$$\frac{d\sigma_{Tou}}{d\Omega} = \frac{4r_e^2}{(v/c)^2}\left[\frac{4}{\sin^4\theta} - \frac{3}{\sin^2\theta}\right], \tag{2.25}$$

where v is the relative velocity in the center of mass system, and θ is the scattering angle. The total cross section expressed in the center of mass system is:

$$\sigma_{Tou} = \frac{8\pi r_e^2}{(v/c)^4}\left[\frac{(|q|\gamma)^2}{(\Delta p_{rf})^2} - 1 + \ln\frac{\Delta p_{rf}}{|q|\gamma}\right], \tag{2.26}$$

where $q = \frac{p_{trans.}}{m_e c}$ is the normalized transverse momentum, and Δp_{rf} is the maximum momentum deviation accepted by the RF system.

The contribution of the Touschek scattering to the beam lifetime τ_{Tou} is given by [9, 42]:

$$\tau_{Tou} = \frac{2^{3/2}\pi\gamma^3\sigma'_x\sigma_x\sigma_y\sigma_l\delta_{max}^2}{r_e^2 c N_b}\frac{1}{\ln\frac{\gamma^2\sigma_x'^2}{1.78\delta_{max}^2}}, \tag{2.27}$$

where $\delta_{max} = \Delta p_{rf}/p$ is the momentum acceptance, σ_l is the longitudinal standard deviation, σ'_x is the horizontal angular standard deviation, and N_b is the number of particles per bunch.

In general, the momentum acceptance in a storage ring is limited by the RF system. But since particles which experience a momentum change Δp in a location with non-zero dispersion function are excited to betatron oscillations with the amplitude [40, 41]

$$\Delta x = D_{eff}^2\frac{\Delta p}{p},$$

a small transverse aperture can also limit the momentum acceptance if the effective dispersion D_{eff} in the ring is large enough. The effective dispersion characterize the excitation of the betatron oscillations averaged over the ring circumference. The connection between the horizontal aperture x, the effective dispersion and the relative momentum acceptance δ_{max} is:

$$\delta_{max}^2 = \frac{x^2}{D_{eff}^2}\frac{\bar{\beta}_x}{\beta_x^\star}, \tag{2.28}$$

where $\bar{\beta}_x$ is the average beta function, and $\beta_x^\star$ is the beta function at the tightest transverse location of the ring.

2.4.2 Beam-Gas Scattering

In a storage ring the particle beam is confined within evacuated chambers, where the residual gas pressure has to be as low as possible to avoid beam losses by the beam-gas scattering.

The particles of the stored beam suffer energy losses or deflections during collisions with gas molecules. There are two different effects: the elastic and the inelastic scattering. Elastic and inelastic scattering can occur on the electrons as well as on the nuclei of the gas molecules. In the case of elastic scattering on a nucleus, the scattered electron is transversally deflected and increases its betatron oscillation amplitude. If the change is large enough, the electron is lost at the physical or dynamic aperture. The elastic and the inelastic scattering on the electrons and as well as the inelastic scattering on the nuclei of the gas atoms, cause energy losses of the scattered electron, which can lead to electron losses at the RF acceptance limit or at the off-momentum dynamic aperture.

The electron losses due to the scattering effects lead to a reduction of the beam lifetime. After collisions with the gas molecules the electrons which are not lost have larger oscillation amplitudes. This effect causes changes in the electron distribution. In particular the tails of the electron distribution are additionally populated.

Elastic Scattering on the Nucleus

The elastic scattering of an electron at the nucleus of a gas atom is described by the Rutherford scattering formula. The differential cross section of the scattering process is given by [9]:

$$\frac{d\sigma_e}{d\Omega} = \left(\frac{2Ze^2}{m_e c^2 \gamma}\right)^2 \frac{1}{(\theta^2 + \theta_l^2)^2} \tag{2.29}$$

where Ω is the solid angle, Z is the atomic number of the gas atom, θ is the scattering angle, and $\theta_l = Z^{1/3}/(192\gamma)$ is the minimum scattering angle due to electron shielding. Electrons with scattering angles larger than a maximum value θ_{max}, which is determined by the acceptance of the accelerator, get lost. Integration of the differential cross section over all angles greater than θ_{max} up to the maximum possible scattering angle, i.e. π, yields the total cross

section for lost electrons in HERA electron ring :

$$\sigma_e = \frac{2\pi Z^2 r_e^2}{\gamma^2} \frac{1}{\theta_{max}^2} \tag{2.30}$$

where θ_l is ignored (since $\theta_l \ll \theta$).

The maximum betatron oscillation amplitude $A(s)$ generated by a deflection θ_{max} depends on the beta function $\beta(s)$ at the position where the scattering occurred and the maximum beta function β_{max}:

$$A(s) = \theta_{max} \sqrt{\beta(s)\beta_{max}} \tag{2.31}$$

The electron is lost if the amplitude $A(s)$ reaches the half aperture H of the beam pipe:

$$A(s) \geq H.$$

Hence it follows for the cross section of lost electrons after averaging over all positions s of the ring:

$$\sigma_e = \frac{2\pi Z^2 r_e^2}{\gamma^2} \frac{\beta_{ave}\beta_{max}}{H^2} \tag{2.32}$$

where β_{ave} is the average beta function.

Inelastic Scattering on the Nucleus

Bremsstrahlung on the nucleus is an inelastic scattering process, in which the scattered electron emits a photon and the nucleus is left unexcited. The scattered electron gets lost if its energy deviation exceeds the RF acceptance. For high energy electrons, the total cross section of the Bremsstrahlung process is given by [42, 9]

$$\sigma_{brem} = \frac{4\alpha Z^2 r_e^2}{3} 4 \left(\ln \frac{183}{Z^{1/3}} \right) \left(\ln \frac{1}{\delta_{max}} - \frac{5}{8} \right), \tag{2.33}$$

where δ_{max} is the relative energy acceptance, i.e. the maximum relative energy deviation, α is the fine-structure constant, and Z is the atomic number of the gas.

Notice that the total cross section is practically independent of the particle energy. It depends logarithmically on the relative energy acceptance of the accelerator. For the HERA electron ring, it amounts to $\sigma_{brem} = 2.97 \cdot 10^{-28}\, m^2$.

Elastic Scattering on the Electrons

In the case of the elastic scattering on the electrons of the gas atom, the scattered electron can transfer a part of its energy to the electrons of the gas. If the resulting energy deviation of the scattered electron is larger than δ_{max}, the electron gets lost. The total cross section σ_{inee} of this process is given by [42, 9]:

$$\sigma_{inee} = \frac{2\pi Z r_e^2}{\gamma} \frac{1}{\delta_{max}}. \tag{2.34}$$

The total cross section of this process is inversely proportional to the particle energy. It amounts to $\sigma_{inee} = 8.25 \cdot 10^{-31}\, m^2$ in the case of the HERA electron ring, where $\gamma = 53816$.

Inelastic Scattering on the Electrons

During the inelastic scattering on the electrons of the gas atom, the scattered electron emits photons. The total cross section σ_{inen} of the inelastic scattering on the electrons is given by [42]

$$\sigma_{inen} = \frac{4\alpha_f Z r_e^2}{3} \left(\ln \frac{2.5\gamma}{\delta_{max}} - 1.4 \right) \left(\ln \frac{1}{\delta_{max}} - \frac{5}{8} \right). \tag{2.35}$$

The total cross section of this process is logarithmically dependent on the particle energy and on the relative energy acceptance and amounts to $1.28 \cdot 10^{-29}\, m^2$ for the HERA electron ring.

Lifetime

The number of the lost electrons dn after passing a distance dx through a volume with N residual gas atoms is given by [9, 42]:

$$-dn = n_0 \sigma N dx$$

where n_0 is the initial number of electrons, and σ is the cross section for the scattering. Hence it follows for the loss rate due to the residual gas:

$$\frac{1}{\tau_{gas}} = \frac{-1}{n_0} \frac{dn}{dt} = c\sigma N \tag{2.36}$$

where τ_{gas} is the lifetime due to the beam-gas scattering.

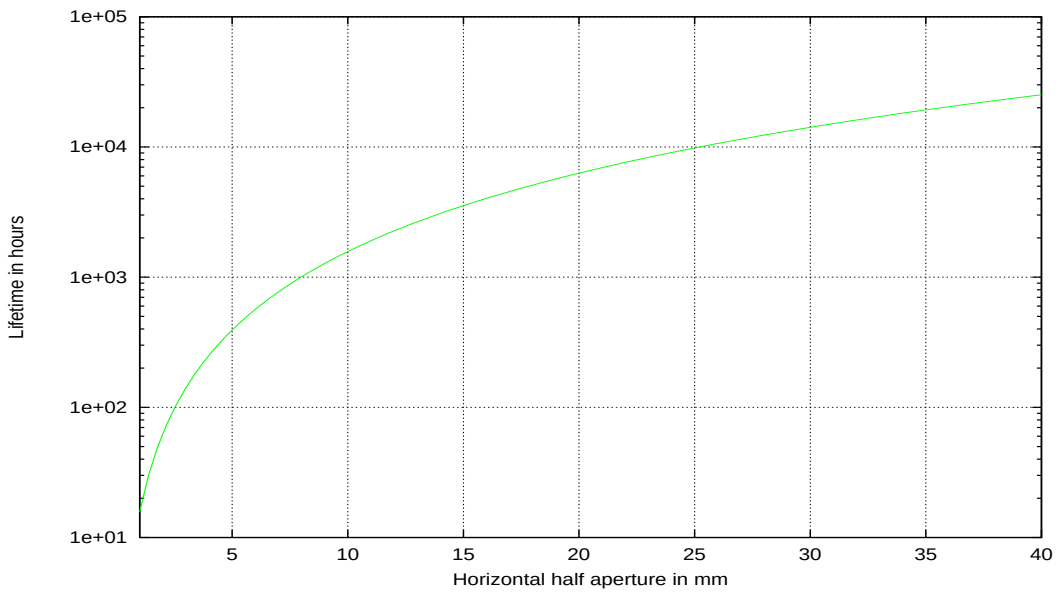

Figure 2.6: *Lifetime due to the residual gas in hours versus horizontal position in mm. The typical gas pressure in HERA amounts to* 10^{-7} *Pa.*

In the case of the elastic scattering on the nucleus, the loss rate due to residual gas is a function of the half aperture H of the accelerator. Using the equations 2.32 and 2.36 and the ideal gas law, the corresponding lifetime can be obtained:

$$\tau_{gas} = \frac{\gamma^2 k_b T}{2\pi Z^2 r_e^2 c P} \frac{H^2}{\beta_{ave}\beta_{max}}, \tag{2.37}$$

where k_b is the Boltzmann constant, T is the temperature, and P is the gas pressure which amounts typically to 10^{-7} Pa in the HERA electron ring.

The contribution of the other beam-gas scattering processes to the beam lifetime can be neglected in the HERA electron ring as well as in the most high energy storage rings.

The Change of Electron Distribution

The density distribution of electrons can be considered as consisting of two regions: the core region with small oscillation amplitudes and the tail region with large oscillation amplitudes.

The beam-gas scattering events cause discrete changes in the betatron oscillation amplitudes of the electrons. The excitation of betatron oscillations due to the beam-gas scattering differs from the quantum excitation in that the beam-gas scattering events occur very infrequently but the expected amplitude changes due to the beam-gas scattering events are much greater than those resulting from the quantum excitation. Therefore the excitation of the betatron oscillation due to the beam-gas scattering can not be treated simply as an addition diffusion term in the Fokker-Planck equation 2.20 [53].

The probability to be scattered on a gas atom is the same for all electrons in the distribution, but the chance to be scattered into the tails of the distribution is much greater than the chance to be backscattered into the core. Since for the typical gas pressure in accelerators, the changes in the core population due to the beam-gas scattering are negligible compared with the changes in the tails, the beam-gas scattering affects mainly the tail region of the distribution.

The total electron distribution under the influence of beam-gas scattering can be described by the sum of a Gaussian distribution ψ_0 and an additional tail distribution ψ_1 which is determined by the beam-gas scattering.

The beam-gas scattering gives rise to a growth of the tail population, because scattered electrons, whose scattering angles are less than the limitation angle θ_{max}, populate additionally the tail region. To get the total cross section for these electrons the differential cross section of the elastic scattering on a nucleus has to be integrated over all angles greater than $\theta_l = Z^{1/3}/(192\gamma)$ up to θ_{max}:

$$\sigma_e = \frac{4\pi Z^2 r e^2}{\gamma^2} \frac{1}{\theta_l^2}. \tag{2.38}$$

Using the effective method of Hirata and Yokoya, one obtains for the additional tail distribution ψ_1 in phase space [11]:

$$\psi_1(I) = \frac{N}{\alpha \cdot 2I} \left(1 - \frac{\sqrt{(\sigma')^2 2I}}{\sqrt{\sigma' 2I + \theta_l^2}} \right), \tag{2.39}$$

where I is the action normalized by the nominal emittance, α is the betatron damping rate, and $\sigma' = \sigma/\beta$ is the normalized standard width, see Appendex B.

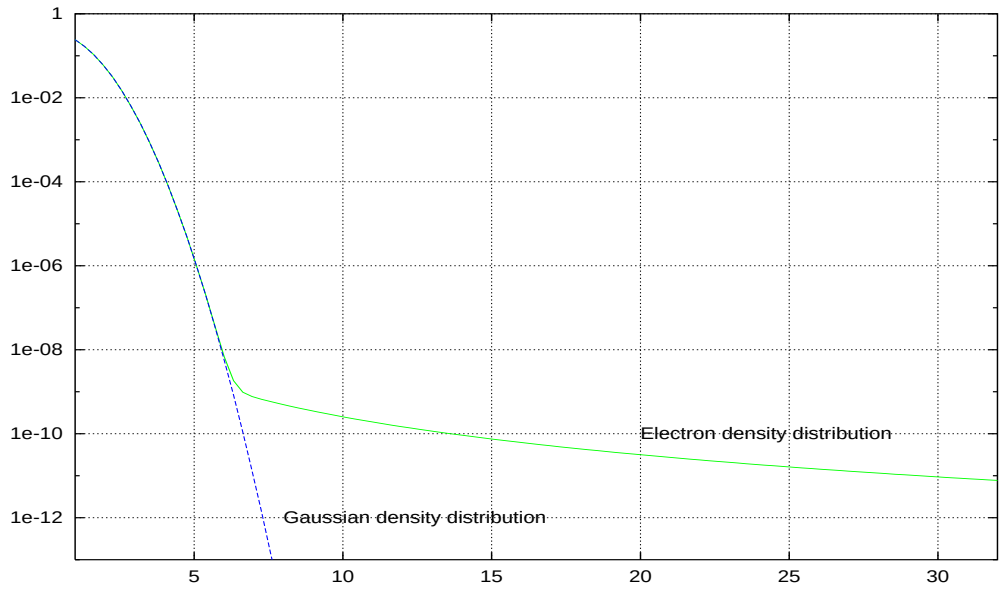

Figure 2.7: *Electron density distribution*

2.5 Nonlinear Forces

Nonlinear forces lead to perturbations in the equilibrium distribution of the electrons in a storage ring. In a real accelerator, like HERA, several sources of nonlinear forces exist. Deviations from the desired field configurations caused by transverse or longitudinal misplacements of magnets with respect to the design orbit, errors in the magnetic field strength, higher order multi pole fields and the beam-beam perturbations are some of the sources of nonlinear forces. In this section the nonlinear forces which are relevant for the HERA electron ring and their influence on the electron distribution are discussed.

2.5.1 Beam-Beam Interaction

In HERA, the counter rotating beams encounter each other in two interaction points, North and South.

During the collision the electrons experience the electromagnetic field from the proton bunch and vice versa. The transverse sizes of the beams at the interaction points are matched. The Gaussian proton distribution is therefore flat and elliptical. The proton charge distribution $\rho(x, y)$ at the

interaction point is given by :

$$\rho(x,y) = \frac{ne}{2\pi\sigma_{x,p}\sigma_{y,p}} \exp\left(-\frac{x^2}{2\sigma_{x,p}^2} - \frac{y^2}{2\sigma_{y,p}^2}\right), \tag{2.40}$$

where $n = N_p/L$ is the longitudinal density of protons in the bunch.

The Lorentz force due to the electromagnetic field of the proton bunch on an electron at x, y is given by:

$$\vec{F} = -e\vec{\nabla}\Phi(x,y),$$

where $\Phi(x,y)$ is the generalized electromagnetic potential:

$$\Phi(x,y) = \frac{ne}{4\pi\varepsilon_0}\int_{t=0}^{\infty} dt \frac{exp\left(-\frac{x^2}{2(\sigma_{x,p}^2+t)} - \frac{y^2}{2(\sigma_{y,p}^2+t)}\right) - 1}{\sqrt{(\sigma_{x,p}^2+t)(\sigma_{y,p}^2+t)}}. \tag{2.41}$$

The horizontal kick on the electron due to the electromagnetic field of the proton bunch is given by:

$$\Delta x'(x,y) = \frac{2N_p r_e}{\gamma} x \int_{t=0}^{\infty} dt \frac{exp\left(-\frac{x^2}{2(\sigma_{x,p}^2+t)} - \frac{y^2}{2(\sigma_{y,p}^2+t)}\right)}{\sqrt{(\sigma_{x,p}^2+t)(\sigma_{y,p}^2+t)}}, \tag{2.42}$$

where γ is the Lorentz factor of the electron. The vertical kick can be obtained by substituting $x, \sigma_{x,p}$ by $y, \sigma_{y,p}$.

For small amplitudes, $x \ll \sigma_{x,p}$, $y \ll \sigma_{y,p}$ the above integral can be evaluated by approximating the exponential function by 1. In this case the kick increases linearly with the amplitude:

$$\Delta x' \approx \frac{2N_p r_e}{\gamma\sigma_{x,p}(\sigma_{x,p}+\sigma_{y,p})} x. \tag{2.43}$$

The linear kick $\Delta x'$ due to the electromagnetic field of the proton bunch causes changes in the betatron phase of the electron. The proton bunch acts like a focussing quadrupole on the small amplitude electrons, and produces therefore a tune shift [4, 5, 12]. The so called *linear beam-beam tune shift* for the electrons depends on the transverse dimensions of the proton bunch $\sigma_{x,p}, \sigma_{y,p}$:

$$\Delta Q_x = \frac{\beta_{x,e} N_p r_e}{2\pi\gamma\sigma_{x,p}(\sigma_{x,p}+\sigma_{y,p})}, \tag{2.44}$$

$$\Delta Q_y = \frac{\beta_{y,e} N_p r_e}{2\pi\gamma\sigma_{y,p}(\sigma_{x,p} + \sigma_{y,p})}, \tag{2.45}$$

where $\beta_{x,e}, \beta_{y,e}$ are the electron beta function at the interaction point.

For large amplitudes, $x > \sigma_{x,p}$, $y > \sigma_{y,p}$ the connection between the kick and the amplitude is nonlinear. The nonlinear component of the beam-beam force can excite resonances up to very high order. Theoretical treatments of the electron distribution in the phase space under the influence of the beam-beam force can be found in [35, 47]. It is shown that the nonlinear component of the beam-beam force can cause deformations of the electron distribution in the phase space, e.g. island structure.

2.5.2 Nonlinear Resonances

The perturbation due to nonlinear terms in the guide fields of a circular accelerator can lead to nonlinear resonances. In general each resonance is driven by a particular pattern of field errors, which occurs periodically at every turn. If any of the harmonics of the perturbation terms coincides with the eigenfrequency of the particles a resonance can occur. The resonant condition for a resonance of the order n is given by:

$$nQ = m,$$

where n, m are integers, and Q is one of the betatron tunes, Q_x or Q_y.

The nonlinear resonances are those of third order and above, driven by the nonlinear multipoles. Their strength is amplitude dependent, so that they become more important for particles at large amplitudes. A powerful tool for the theoretical treatment of the resonances in a circular accelerator is the Hamiltonian formalism. Applying perturbation theory to the Hamiltonian of the stored particles, the nonlinear resonances can be investigated [48, 49, 13, 4]. This theoretical treatment is complicated and goes beyond the scope of this thesis. Only some results of it are therefore presented here.

In the presence of resonances, the perturbed Hamiltonian H_1 of a stored particle can be split in an unperturbed Hamiltonian H_0 and small perturbations [49]:

$$H_1(J_1, \theta, \psi_1) = H_0(J_1) + \sum_n RU_n(J_1, \theta) \exp(in\psi_1), \tag{2.46}$$

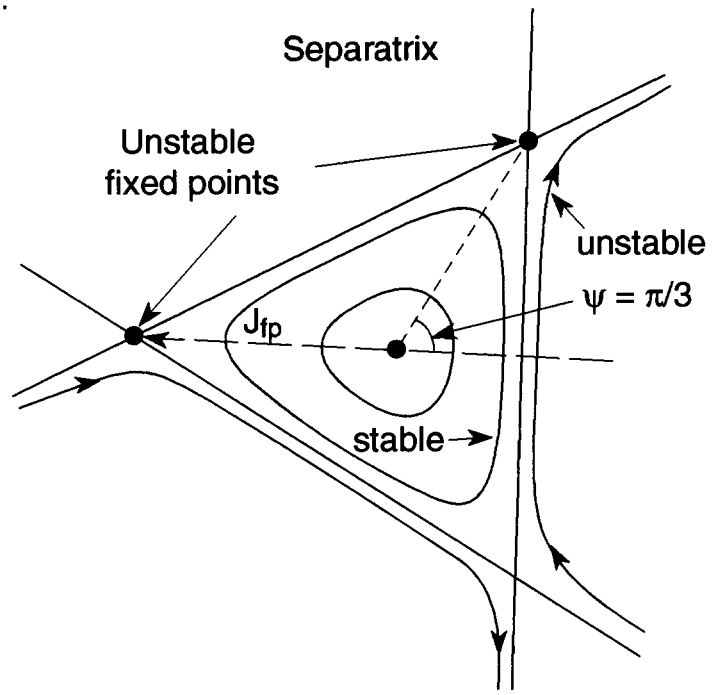

Figure 2.8: *Particle trajectory in the phase space,*(ψ_2, J_2)*, close to the third order resonance. The unstable fixed points are given by the* $\psi_2 = \pi/3,\ 3\pi/3,$ *and* $5\pi/3$.

where J_1 is the action, R is the radius of the orbit, s is the path along the particle's trajectory, $\theta = s/R$ is the azimuthal angle, $U_n(J_1, \theta)$ is the driving perturbation of the order n, and ψ_1 is the angle variable.

Close to a resonance, $nQ = m$, the Hamiltonian H_1 can be transformed to [49]:

$$H_2(J_2, \psi_2) = (Q - \frac{m}{n})J_2 + RU_{0,0}(J_2) + RU_{mn}\exp(in\psi_2), \tag{2.47}$$

where J_2, ψ_2 are the new action and angle variables. H_2 is independent of θ and defines a closed contour in its phase space (J_2, ψ_2).

The third order resonances plays a special role in accelerator physics and so for the HERA electron ring, since the sextupole magnets, which are necessary for the chromaticity correction, introduce third order resonances. In the case of the third order resonance, the U_{00} term in the equation 2.47 is zero for m=odd multipoles and the Hamiltonian is given by [49]:

$$H_2(J_2, \psi_2) = (Q - \frac{m}{3})J_2 + RU_{m3}\cos(3\psi_2), \tag{2.48}$$

Defining constants $\delta = Q - m/3$ and $\varepsilon = RU_{3m}/J_2^{3/2}$, the Hamiltonian in equation 2.48 can be rewritten :

$$H_2(J_2, \psi_2) = \delta J_2 + \varepsilon J_2^{3/2}(\cos(3\psi_2)), \tag{2.49}$$

If ε is small, either because the amplitude is small or the driving strength is weak, the contour defined by H_2 is close to a circle. This is also the case, if δ is large. In the cases of large ε or small δ, the circle will be distorted inwards $\psi_2 = 0, 2\pi/3, 4\pi/3$ and outwards in between to become somewhat triangular, like in figure 2.8. This triangle does not rotate but is frozen in (ψ_2, J_2) space. The edges of this triangular trajectory in the phase space are called *fixed points*. They are given by:

$$\psi_2 = \pi/3, \;\; 3\pi/3, \;\; and \;\; 5\pi/3.$$

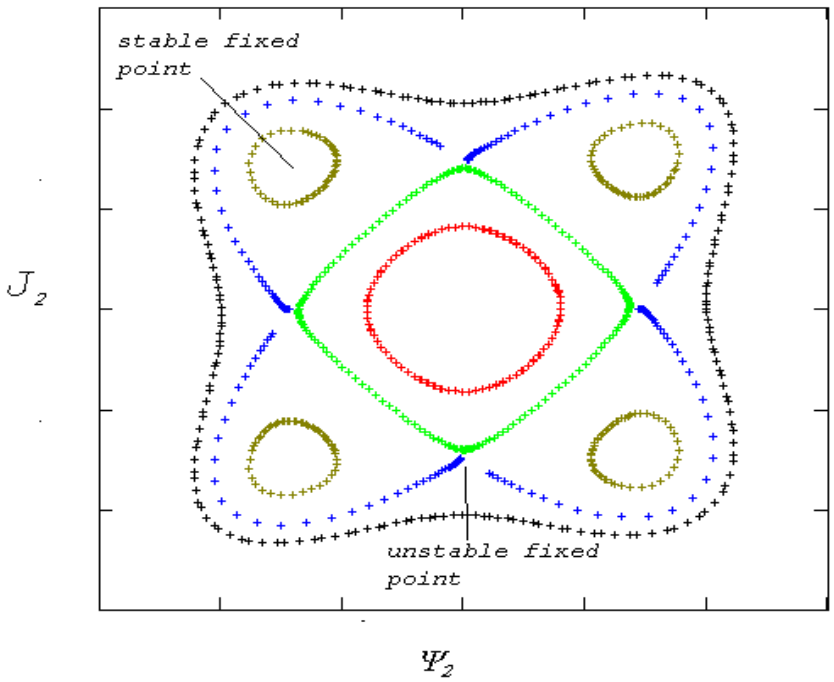

Figure 2.9: *Particle trajectory in the phase space,(ψ_2, J_2), close to the fourth order resonance.*

An octupole leads to an extra term in the Hamiltonian which corresponds to a nonlinear variation of frequency with amplitude. This is characteristic of even m multipoles and defines quite a different topology of phase space [49, 4, 13]. Figure 2.9 shows the effect of an octupole in the phase space (ψ_2, J_2). The existence of *stable fixed points*, which are the centers of an archipelago of stable islands, is only the case for even order resonances. The particle trajectory will remain contained within the islands unless there is some way in which particles may leak out.

Chapter 3

HERA and H1 Detector

The experiments H1 and ZEUS at the HERA storage ring employ the inelastic electron-proton scattering with high momentum transfer to explore the structure of the proton.

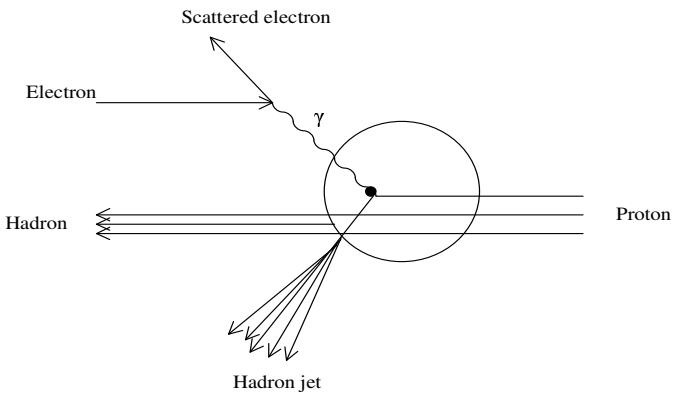

Figure 3.1: *Inelastic electron-proton scattering in the QCD representation for the HERA interactions*

For the HERA proton energies of 920 GeV, a proton can be considered as a parallel current of free massless partons in the lab system which have zero transverse momenta(fig 3.1). During the scattering process, a virtual photon interacts with a parton which is scattered and fragments into a hadron jet. The other partons also transform into a hadron jet.

The detailed analysis of the scattered electron and the hadron jet in the H1 detector makes it possible to get information about the nature of the partons in the proton or fragmentation processes respectively. In order to optimize the analysis, the background in the detector due to the synchrotron radiation has to be minimized. Therefore a collimation system protects the H1 detector from the synchrotron radiation. The first section of this chapter describes the HERA beam facility. The second section deals with the H1 detector. The present synchrotron radiation collimation system of H1 is discussed in the last section of this chapter.

3.1 The HERA Storage Ring

The Hadron Electron Ring Accelerator, HERA, consists of two independent circular accelerators- the electron ring and the proton ring- which are brought together in only two points: interaction points North and South. The experiment H1 is installed in the interaction point North and the experiment ZEUS is installed in the interaction point South. A schematic overview of the HERA storage ring is shown in fig. 3.2a.

In HERA, the counter rotating beams collide at a center of mass energy of 300 GeV. Here the proton beam has an energy of 920 GeV, a beam current of about 100 mA and a lifetime in the order of 100 h whereas the electron beam has an energy of 27,5 GeV, a beam current of about 40 mA and a lifetime of 15 h. HERA is operated with a head-on collision geometry at each of the two interaction points.

The acceleration chain of the proton beam consists of a linear accelerator LINAC III, a proton synchrotron DESY III, the former e^+/e^- storage ring PETRA used now as a booster to accelerate the protons to the injection energy of the HERA proton ring, and finally the HERA proton ring, see fig. 3.2b. In order to obtain the proton beam a H^- ion source is used. The H^- ions which are first focused and accelerated in a radio frequency quadrupol, RFQ, reach in the LINAC III a final kinetic energy of 50 MeV. After transferring to the DESY III the H^- ions lose electrons on the so called carbon stripping foils. Before transferring to PETRA the proton beam is accelerated to 7.5 GeV in the DESY III. 60 proton bunches corresponding to 6 cycles at the DESY III are required to fill PETRA. These bunches are accelerated up to 40 GeV and injected into the HERA proton ring. After 3 such cycles, the HERA proton ring is filled with 180 proton bunches at

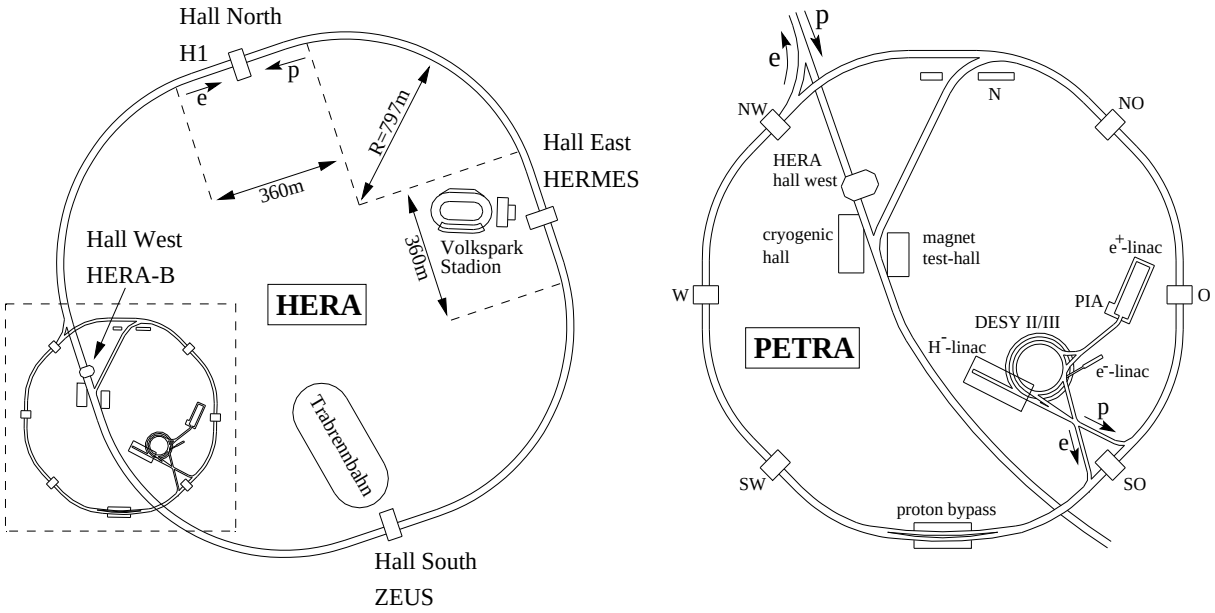

Figure 3.2: *a) A View of the HERA storage ring (left) b) And the HERA pre-accelerators (right)*

40 GeV.

The acceleration chain of the electron beam is composed of a linear accelerator LINAC II, an electron synchrotron DESY II, the former e^+/e^- storage ring PETRA and finally the HERA electron ring, see fig. 3.2b. The electrons from the LINAC II injected are accelerated to 7 GeV in DESY II. After transferring into PETRA the beam is accelerated up to 12 GeV and injected to the HERA electron ring. In order to fill the HERA electron ring with 189 bunches, 4.5 PETRA fill cycles are required.

The current distribution in HERA contains 15 non-colliding electron bunches, so called pilot bunches, and 6 non-colliding proton bunches. The electron pilot bunches are used to study beam induced background arising from interactions of the beam with residual gas. The bunches are spaced by 96 ns.

3.2 The H1 Detector

The H1 detector is composed of several sub detectors. It's enhanced instrumentation in the proton direction takes into account the asymmetric HERA beam energies. Figure 3.3 shows a schematic view of the H1 detector. In the top right corner of the figure, the H1 coordinate system is shown. It is right handed and chosen such that the z-axis is pointing into the direction of the outgoing proton beam, called forward direction. In this section the main components of the H1 detector are briefly described.

3.2.1 Tracking System

The H1 tracking system is shown in figure 3.4. It consists of drift chambers, multiwire proportional chambers and silicon detectors. The tracking system is separated into a Forward Track Detector (FTD) and a Central Track Detector (CTD).

The Central Track Detector is composed of the Central Silicon Tracker (CST), the Central Inner Proportional Chamber (CIP), the Central Inner z-Drift Chamber (CIZ), the inner Central Jet Chamber (CJC1), the Central Outer z-Drift Chamber (COZ), the Central Outer Proportional Chamber (COP), and the outer Central Jet Chamber (CJC2).

The silicon strip microvertex detector CST is used to obtain a separation of primary and secondary vertices in an event. The CST consist of two layers of silicon strip detectors mounted cylindrically around the beam pipe at radii of $R = 57.5\,\mathrm{mm}$ and $R = 97\,\mathrm{mm}$ respectively. The CST is centered at the nominal interaction point and has an effective length of 358 mm. Its polar angle acceptance is $30° < \theta, 150°$.

The chambers CJC1, CJC2, CIZ,and COZ are used for track reconstruction. The information of the inner and outer central jet chamber CJC1 and CJC2 are used mainly to perform the track reconstruction in the transverse projection of the H1 detector, while the inner and outer z-drift chamber CIZ and COZ are used to improve the z resolution. The CJC1 is built of 30 drift cells with 24 radial sense wires each, the CJC2 has 60 drift cells with 32 radial sense wires each (see fig. 3.6). The active length of the central jet chambers in z is 220cm and the radial dimensions are 22.4cm (CJC1) and 29.6cm (CJC2) respectively. The CIZ consist of 15, and the COZ of 24 similar rings, where each ring contains 4 sense wires. The rings are arranged along the beam axis.

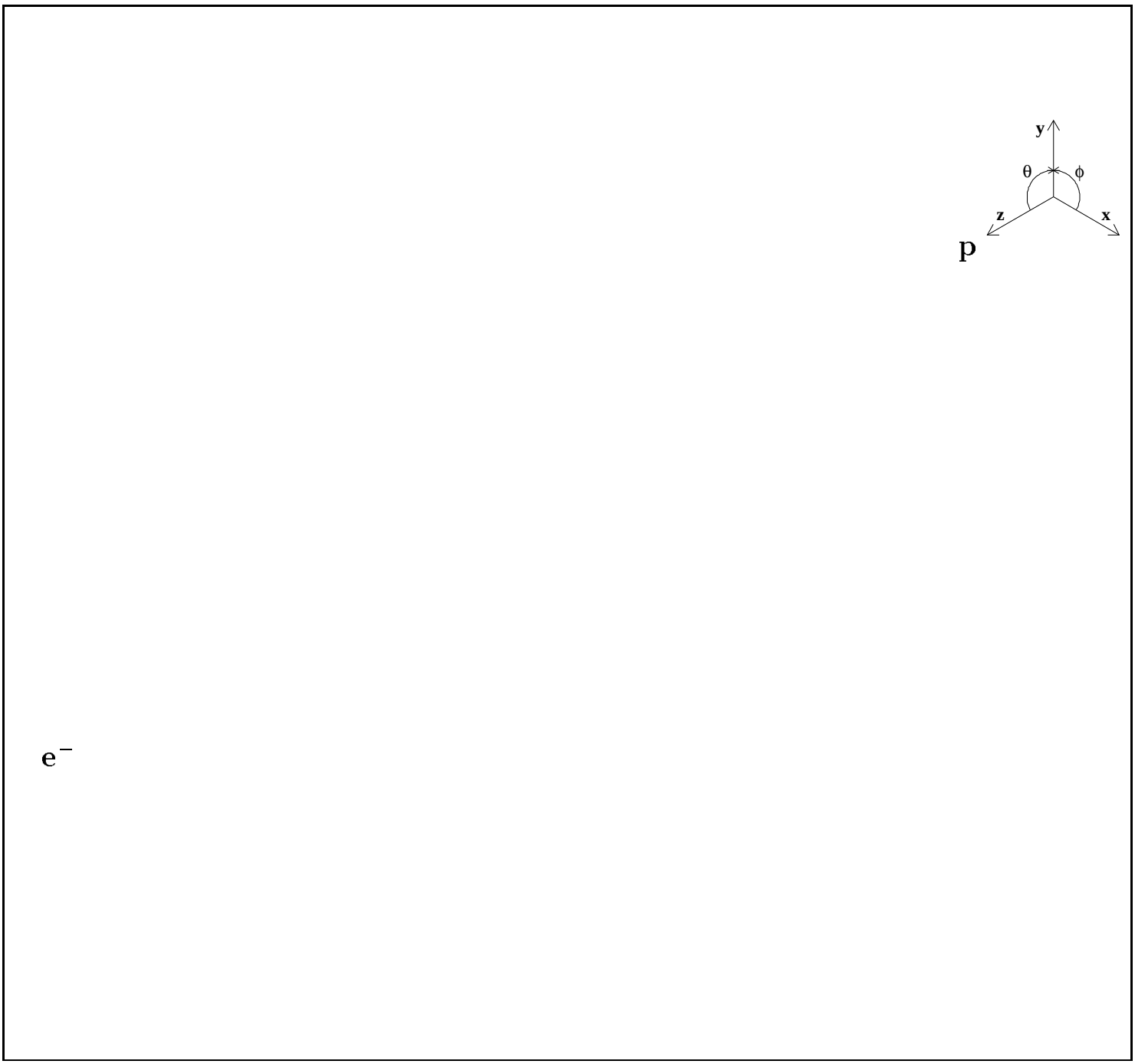

1	Beam pipe and beam magnets	9	Muon chambers
2	Central tracking device	10	Instrumented iron yoke
3	Forward tracking device	11	Forward muon toroid
4	Electromagnetic LAr calorimeter	12	Backw. electromagn. calorimeter (BEMC)
5	Hadronic LAr calorimeter	13	PLUG calorimeter
6	Superconducting coil (1.15 T)	14	Concrete shielding
7	Compensating magnet	15	Liquid argon cryostat
8	Helium supply for 7		

Figure 3.3: *A schematic view of the H1 detector.*

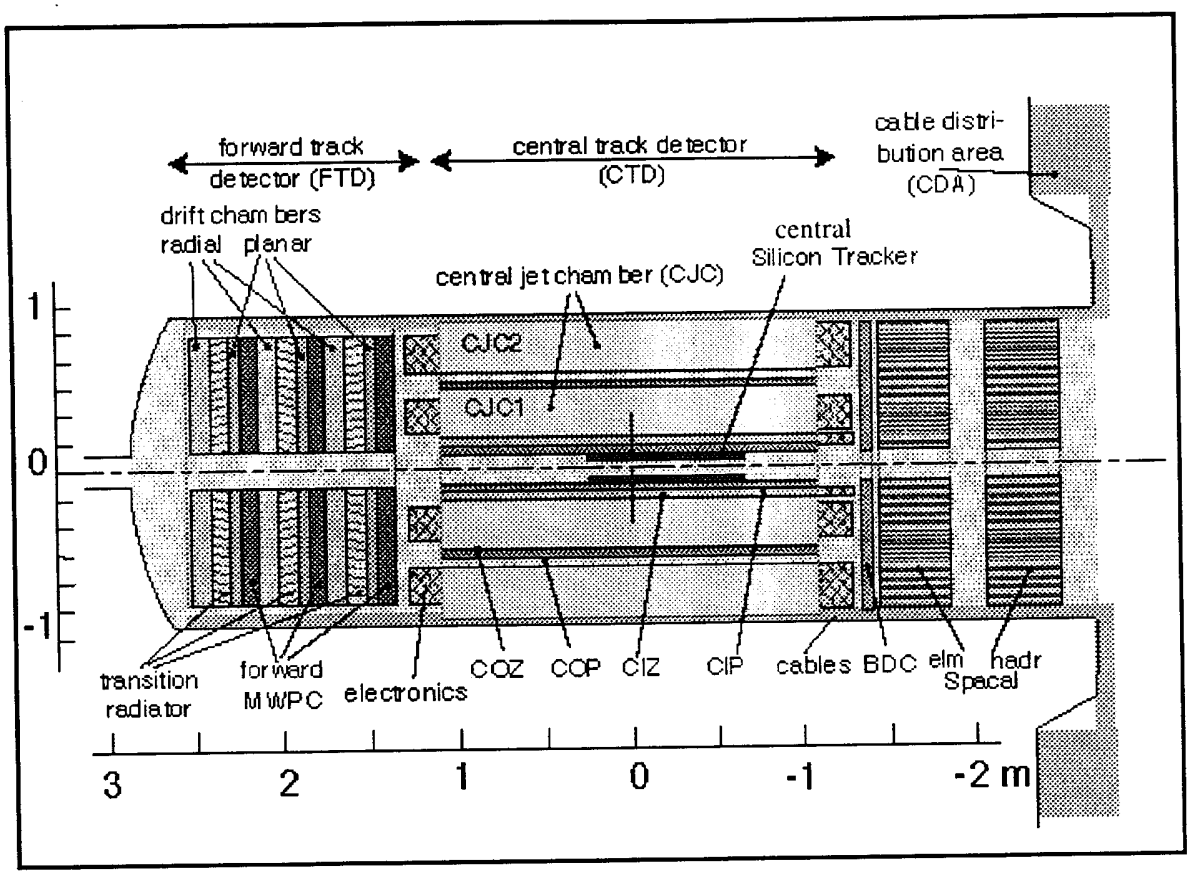

Figure 3.4: *A schematic view of the H1 tracking system.*

The central multiwire proportional chambers CIP and COP provide information for trigger purposes.

3.2.2 Calorimetry

The Liquid Argon, LAr, calorimeter consists of an electromagnetic and a hadronic part with lead or high grade steel absorbers respectively. It covers a large polar angle region ($4^o \leq \vartheta \leq 153^o$) and is complemented in the backward direction by a spaghetti type backward calorimeter (SpaCal) which is divided into an electromagnetic and a hadronic section. The depth of the LAr electromagnetic calorimeter varies with ϑ between 20 and 30 radiation

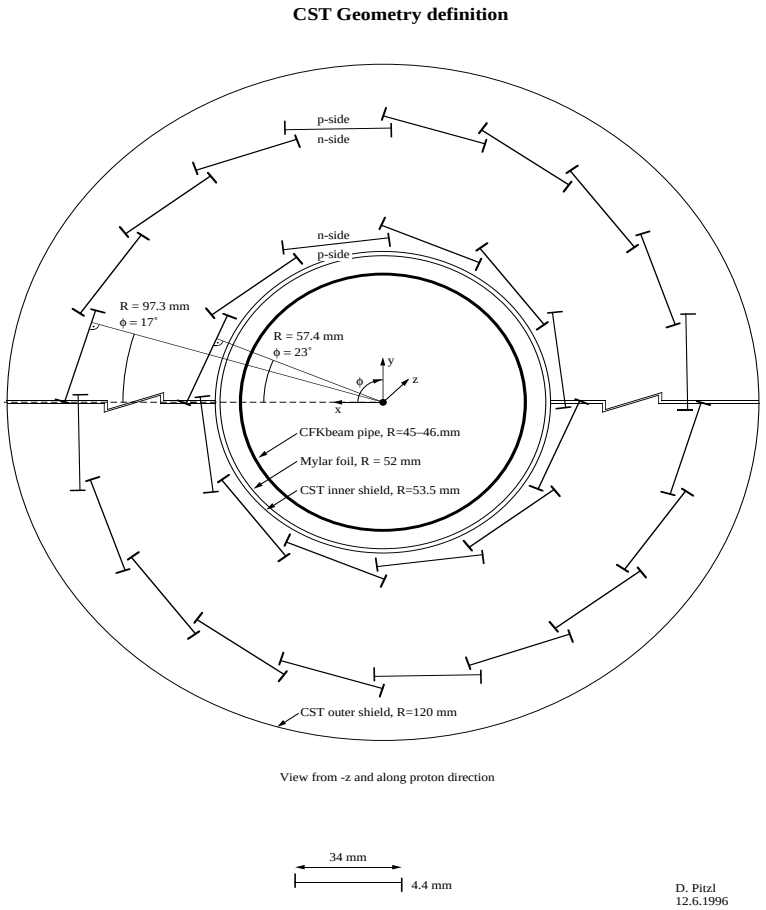

Figure 3.5: *A schematic radial view of the vertex detector CST.*

lengths, X_0, while the depth of the hadronic calorimeter lies between 5 and 8 interaction length, λ. The energy resolution is $\sigma_E/E = 12\%/\sqrt{E(GeV)}$ in the electromagnetic part and $\sigma_E/E = 50\%/\sqrt{E(GeV)}$ for the hadronic measurements.

The SpaCal is a warm calorimeter with optical read out, where scintillating fibers are immersed in a lead absorber. It covers a polar angular region up to $\vartheta = 178^o$. The electromagnetic section with a depth of roughly 25 radiation lengths consist of small cells ($4cm \times 4cm$) resulting in a high spatial resolution. The hadronic part has coarser granularity. The energy resolution of the SpaCal is about $\sigma_E/E = 7.5\%/\sqrt{E(GeV)}$ in the electromagnetic part

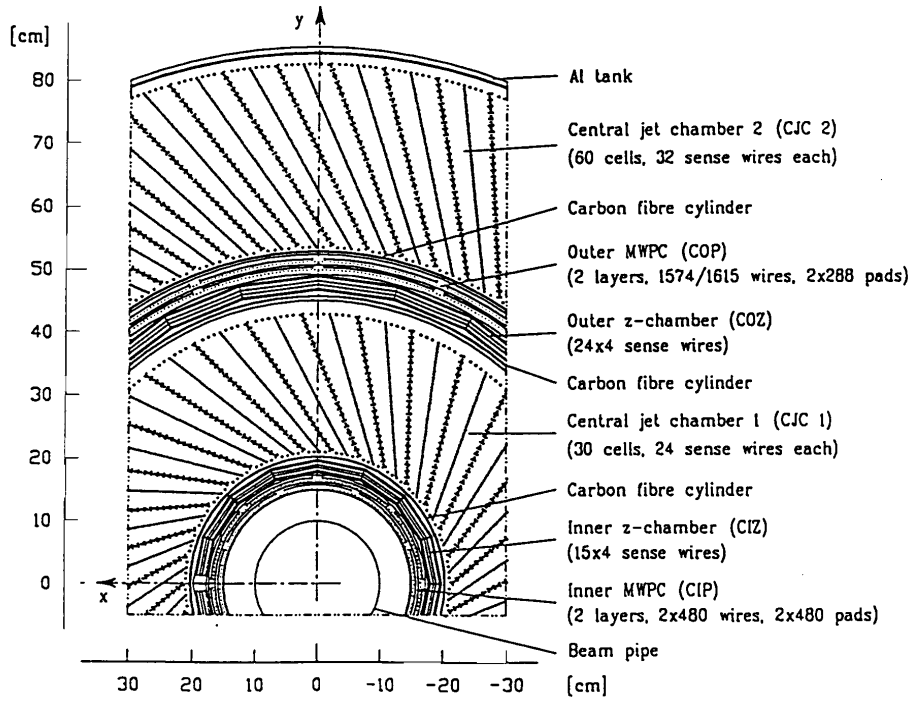

Figure 3.6: *Radial view of the Central Tracking Detector.*

and $\sigma_E/E = 30\%/\sqrt{E(GeV)}$ for the hadronic measurements.

3.2.3 Central Muon Detector

The instrumented iron of the H1 detector is not only used as the return yoke for the magnetic flux but also as the Central Muon Detector (CMD) and a back up calorimeter. The Central Muon Detector is divided into four regions: the backward endcap, the barrel and the forward endcap. For readout and trigger purposes the entire detector is separated into 64 modules, see figure 3.7.

Each module consist of ten 7.5cm thick iron plates sandwiching ten layers of streamer tubes. 16 streamer tubes build an element and several elements form a plan, which is equipped on the outside with strip or pad electrods. The elements are oriented such that the sense wires are strung parallel to the x-axis in the endcaps and the z -direction in the barrel region.

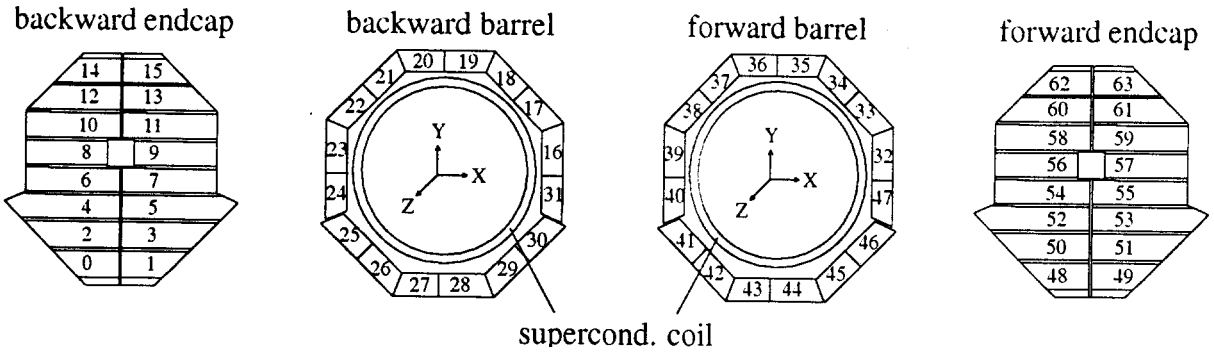

Figure 3.7: *The Central Muon Detector*

3.3 Synchrotron Radiation Collimation System

As mentioned before, HERA is operated with a head-on collision geometry. The electron beam is guided by a final bend of 10 mrad to the proton beam at the interaction regions. This requires strong bending and focusing magnets in the electron ring at the interaction regions, which lead to high synchrotron radiation emission, as discussed in the second chapter. In the present HERA configuration, a radiation collimation system shields the H1 detector from the synchrotron radiation caused by the electron beam in the interaction region. Figure 3.8 shows a schematic view of the H1 interaction region with the present radiation collimation system. The collimators $C1, C2$, and $C3$ scrape the synchrotron radiation fan in front of the H1 detector, while the collimators $C4$ and $C6$ shield the detector from backscattered synchrotron radiation. Each collimator is equipped with an anti reflection coating to minimize the edge scattering and backscattered radiation in the H1 detector. More detailed information can be found in [21]

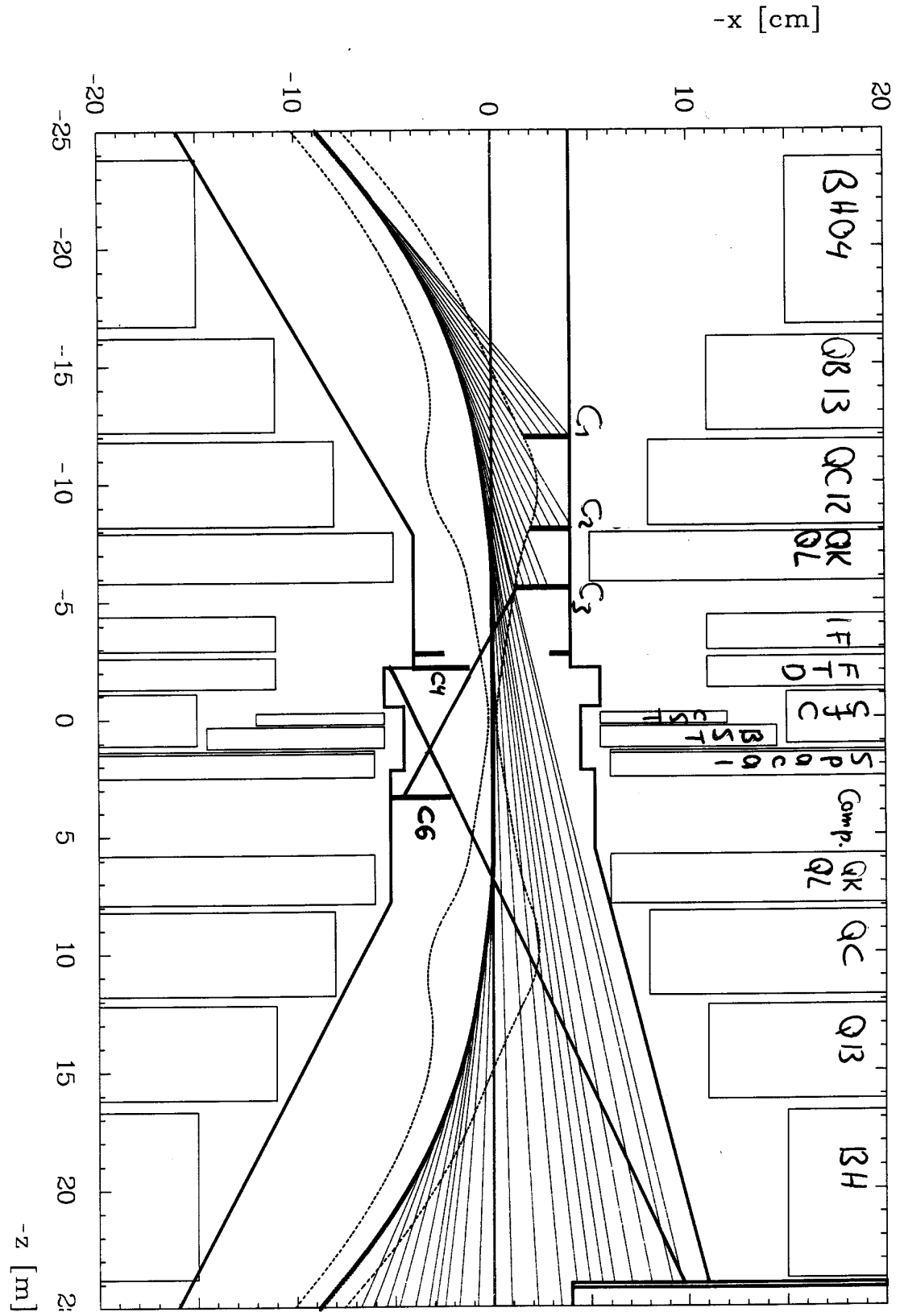

Figure 3.8: *The synchrotron radiation collimation system for the H1 detector. The H1 interaction region is shown in x-z plane. The elements denotes by BHs are dipoles and the QB, QC, QK and the QL are quadrupole magnets*

Chapter 4

HERA Upgrade Project and the New H1 Detector

The data accumulated by the HERA experiments H1 and ZEUS are used to explore the structure of the proton and to make precise tests of QCD. In this connection, the luminosity is an important parameter. The luminosity is the rate of events for a process of unit cross section. An increase in the HERA luminosity makes new unique and sensitive tests for the QCD and the Standard Model possible and enables the experiments to look for new physics beyond the Standard Model.

The HERA luminosity is proportional to the electron and the proton beam currents. It is inversely proportional to the root of the emittances of both beams and to the root of the beta functions of the beams at the interaction point. Due to the limitations in the proton pre-accelerator chain, it is difficult to increase the proton bunch intensity or to decrease the proton emittances [6]. The electron current is limited by the available electron RF power. Therefore an increase in the HERA luminosity can be achieved best by the reduction of the transverse beam dimensions at the interaction point, i.e. by the reduction of the electron emittance and the beta functions of both beams. An increase in the phase advance per FODO cell combined with a shift of the RF frequency can be used to reduce the electron emittances [28, 31]. A reduction of the beta functions of both beams is possible by modifications of the magnet structure in the interaction region.

In order to increase the luminosity, an upgrade of the HERA electron proton collider is planned, which contains improved interaction sections for the experiments. The luminosity, the electron emittance and the beta functions

Table 4.1: The electron emittances and the beta functions of both beams at the interaction point for the present and upgraded HERA configuration

HERA configuration	Hor. electron emittance in m rad	Proton β_x in m	Proton β_y in m	Electron β_x in m	Electron $\beta_y$in m	luminosity in $cm^{-2}s^{-1}$
present	$4.2 \cdot 10^{-8}$	7.00	0.50	1.00	0.70	$1.5 \cdot 10^{31}$
upgraded	$2.2 \cdot 10^{-8}$	2.45	0.18	0.63	0.26	$7 \cdot 10^{31}$

of both beams for the present and upgraded HERA configuration at the interaction point are given in table 4.1. In this chapter the new planned magnet structure of the H1 interaction region and its consequences for the upgraded H1 detector are investigated by simulation programs. A collimation system to shield the detector from the backscattered synchrotron radiation is also designed using simulation programs.

4.1 Magnet Structure at the H1 Interaction Region

The reduction of the beta functions of both beams at the interaction point is performed by a so called *mini beta insertion structure.* [7, 8]

Since the maximum beta function β_{max} in the first so called *final focus quadrupole* is essentially inversely proportional to the beta function $\beta^\star$ at the interaction point:

$$\beta_{max} \approx \frac{s^2}{\beta^\star}$$

the reduction of the beta functions is limited by the mechanical aperture in the final focus quadrupoles. This mechanical limitation can be reduced by installing the final focus quadrupoles closer to the interaction point, i.e. to decrease the distance s of these elements from the interaction point. But for constant β_{max}, the contribution to the chromaticity $\Delta\xi$, which is undesirable, increases with the decreasing distance s:

$$\Delta\xi \simeq \frac{\beta_{max}}{2\pi s}.$$

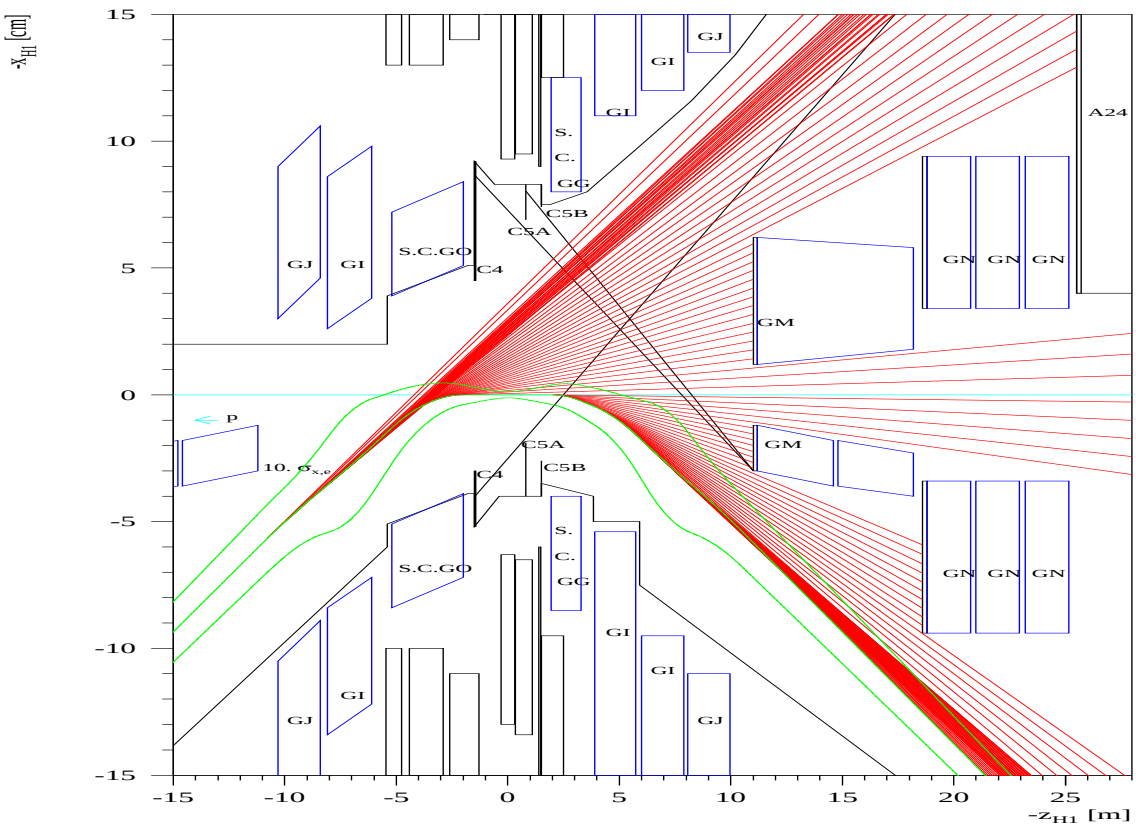

Figure 4.1: *A schematic view on the H1 interaction region from above. The GG and the GO are superconducting combined function magnets, which separate the two beams. The GIs and the GJs are electron quadrupoles while the GM and GN are proton quadrupoles.*

This gives rise to a limitation for the decreasing distance s and consequently for the beta function β^* at the interaction point.

An additional limitation of the decreasing distance in the case of the proton final focus quadrupoles is caused by the fact that the electron beam cannot be exposed to the strong focusing fields of the proton magnets. This means that an early separation of the beams is necessary. The strong magnetic separation fields has to be located as close as possible to the interaction point to ensure that the proton final focus quadrupoles can also be installed as close as possible to the interaction point. Therefore the separation fields for the upgraded HERA lattice are generated by superconducting magnets,

GO and GG, inside the detector, which have a distance of 2 m from the interaction point, see figure 4.1. Their bending radius of 400 m is reduced by a factor of three compared to the present design. On the one side of the interaction point the GO deflects the electron beam by about 8 mrad and on the other side the GG and the quadrupole GI deflect together the electron beam also about 8 mrad. In order to avoid large chromatic effects in the focusing of the electron beam, the separator magnets also have a noticeable gradient field to provide early focusing [6].

At both sides of the interaction point, there are two further final focus quadrupoles, GI and GJ, outside the detector, which provide additional focusing of the electron beam in the horizontal or the vertical plane respectively (figure 4.1). Both beams pass through the final focus triplets consisting of the superconducting magnets inside the detector and the quadrupoles outside the detector.

The first exclusive proton focusing magnet, GM, is installed at 11m distance from the interaction point. It is a half quadrupole with mirror plates. The following proton magnet is of the same type. Three further quadrupoles, named GN, follow these two. The first five proton final focus quadrupoles are designed as septum magnets. They form the first vertically focusing lens of a double-doublet structure with two vertically and two horizontally focusing lenses [7, 8].

4.2 Simulation Program and the Results of the Simulation

The final focus triplets which provide the early separation and the strong focusing of the electron beam, are also the source of strong synchrotron radiation.

In order to investigate the synchrotron radiation in the H1 interaction region and its consequences for the detector, a simulation program is used [21]. This program consists of three subprograms. The first one simulates the motion of an electron beam with a Gaussian distribution for a given energy through the magnet structure. It simulates also the emission of the synchrotron radiation and the radiation hits on the beam pipe and the magnets. The second subprogram treats the interactions of the incident photons with the pipe or the magnet material respectively. The backscattered radiation

from the beam pipe and the magnets into the H1 direction is simulated in a third subprogram.

In the first subprogram, the magnets and the drift paths are represented by matrices. The initial coordinates of the Gaussian distributed electrons are given by a random number generator. The electrons are tracked through the magnet structure using a matrix formalism. In intervals of 1 cm, a further random generator decides which electrons emit synchrotron photons. The critical energy of the emitted photons is calculated from the energy of the electron beam and the total bending fields at the positions of the emitting electrons, according to the equation 2.9. The second program simulates the interactions of the incident photons with the absorber material with regard to the photon energies, the angle of incidence, and the properties of the material. The simulation is carried on until the photons are absorbed or leave the absorber. In the third subprogram the photons which hit the components of the H1 detector are tracked and counted as well as the energies which they deposit in each component are calculated. For more details see [21]. In the following the results of the simulations are discussed.

As already mentioned, the planned electron final focus triplets will cause strong synchrotron radiation. Compared to the present HERA design, the total radiation power in the H1 interaction region will increase by a factor of three to about 30 kW in the nominal case of an electron beam with 27.5 GeV energy and 58 mA beam current. Because of the geometry of the upgraded interaction region as well as the high radiation power and the critical energies of about 150 keV at the edge of the radiation fan, it will no longer be possible to shield the H1 experiment by the collimation of synchrotron radiation upstream of the detector. Therefore the beam pipe inside the H1 detector has to be large enough to pass the direct synchrotron radiation fan through the detector, see figure 4.1. After the passage through the detector, the direct radiation impinges on the following components: the absorber in the radiation pipe, the absorbers on the first proton magnets which are equipped with special cooling systems, and on the beam pipe inside the down stream separation magnet GG. For a Gaussian electron beam with nominal parameters the numbers of incident photons on the absorbers and the beam pipe are given in the tab.4.2.

The absorbers and beam pipe segments are strong sources of backscattered synchrotron radiation, as it can be concluded from table 4.2 .

Table 4.2: Number of incident and backscattered photons,at an electron energy of 30 GeV and 58 mA beam current

Absorber	Distance from the IP (m)	Hor. Width 0f the absorber (cm)	Number of incident photons per second	Number of backscattered photons per second
GM_{inn}	11.00	1.80	$2.70 \cdot 10^{17}$	$9.44 \cdot 10^{13}$
GM_{out}	11.00	5.00	$4.14 \cdot 10^{17}$	$1.45 \cdot 10^{13}$
GN_{inn}	19.00	6.00	$2.40 \cdot 10^{17}$	$8.39 \cdot 10^{13}$
$A24$	24.00	21.00	$6.16 \cdot 10^{17}$	$2.16 \cdot 10^{14}$
GG-Beam *Pipe*	3.30	1.50	$3.59 \cdot 10^{12}$	$1.26 \cdot 10^{9}$

4.3 The H1 Radiation Shielding

In order to protect the central part of the H1 detector from the backscattered radiation, a system of collimators had to be designed, which leaves an aperture large enough to pass the direct radiation but small enough to shield the detector from the backscattered synchrotron radiation. Using the simulation program an optimum collimation system for the H1 detector is designed in the scope of this thesis. Figure 4.2 shows the future H1 collimation system consisting of three Tungsten collimators, which have a thickness of $1 - 2$cm. The collimators $C4$ and $C5A$ are horizontal collimators while the collimator $C5B$ is *keyhole* shaped to achieve a better shielding for the H1 detector, see figure 4.11.

Table 4.3: The H1 collimation system

Collimator	Distance from the IP z (m)	horizontal distance of collimator from beam axis x (cm)
C4	-1.50	4.5
C5A	0.81	6.9
C5B	1.50	7.4

Since the distance of the collimators from the beam axis is determined by the dimensions of the direct synchrotron radiation fan (tab. 4.3) the central

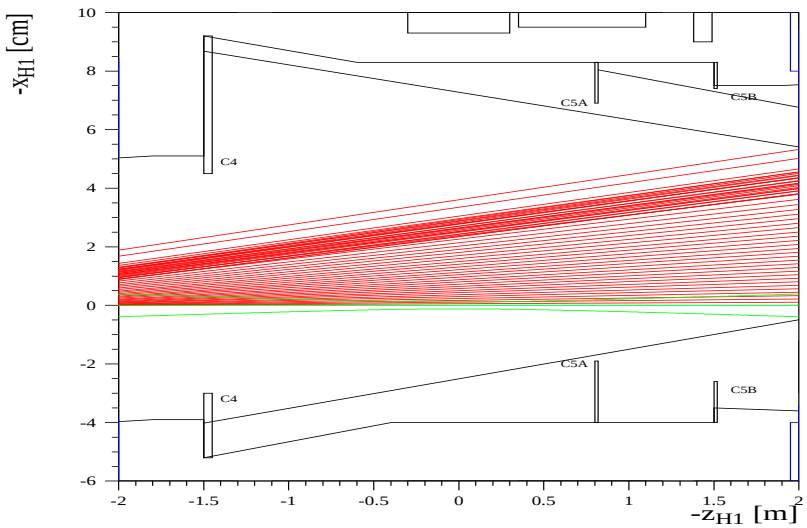

Figure 4.2: *A schematic view of the central beam pipe of the H1 detector with the direct synchrotron radiation fan. The H1 collimation system consisting of the horizontal collimators C4 and C5A as well as the keyhole shaped collimator C5B is shown.*

pipe inside the H1 detector has to be enlarged to an extent that the it is totally shaded from the backscattered radiation by the collimation system, as shown in figure 4.2.

The collimation system is hit by the backscattered photons and is therefore itself a source of radiation which is twice backscattered and impinges on the H1 detector. In the table 4.4, the simulated hits in the H1 detector per bunch crossing, BC, and the limits for the sensitive components of the H1 detector are shown.

The twice backscattered radiation in the detector can be reduced by using an anti reflection coating of 200 μm copper on 400 μm silver. The reduction factor increases with the angle of incidence. For example, a reduction factor of 1000 occurs for an angle of incidence of $\pi/2$, whereas the reduction factor for an angle of incidence of 100 mrad is only by 20. The reduction of backscattered radiation caused by the coating is not included in the simulations for the table 4.4.

Table 4.4: Synchrotron Radiation: Limits and Expected Hit/BC

	CJC Pattern Recognition	BST	FST	CST
Limits	$< 8 Hits/BC$	$< 60 Hits/BC$	$< 60 Hits/BC$	$< 60 Hits/BC$
Expected	$< 3 Hits/BC$	$< 1 Hits/BC$	$< 1 Hits/BC$	$< 1 Hits/BC$

4.4 The Contribution of the Tails of the Electron Distribution to the Radiation Fan

The synchrotron radiation fan in the H1 interaction region is emitted by the electron beam while it passes the final focus triplet magnets. The photons on the edge of the radiation fan are emitted by the electrons which have an oscillation amplitude lager than 4σ. These electrons are denoted as tail electrons in the present section.

Figure 4.3 shows the simulated transverse profiles of the radiation fans at the position of the collimator $C5B$ for a Gaussian electron beam. At the top of the figure, the radiation emitted by the electrons in the core is shown while at the bottom the radiation caused by the whole distribution is shown. Obviously the radiation from the tail electrons causes the edge of the radiation fan with $x > 6\,\mathrm{cm}$.

The electrons in the tails of the distribution have large betatron oscillation amplitudes. They experience an additional bending field inside the final focus quadrupoles GIs and GJs and emit therefore photons with higher energies. In figure 4.4, the horizontal profile of the critical energy of the radiation fan in the H1 interaction region at the position of the collimator $C5B$ is shown. The edge of the radiation fan at $x \approx 7cm$, which is caused by the final focus quadrupole GI, has a critical energy of about 150 keV. The higher critical energies of about 220 keV for $x < 5cm$ is caused by the combined function magnet GO.

In the case of the Gaussian distributed electrons, the population of the tails is by some orders of magnitude smaller than the core population (fig.4.5). Consequently the number of photons in the edge of the radiation fan is by some order of magnitude smaller than in the central part, as shown in figure 4.6. Therefore the electrons in the tails beyond 7 standard deviations can be ignored, in spite of the fact that the tail electrons emit photons with

very high energies. Whereas in the case of an electron distribution with non Gaussian tails, the tails can be of importance, if they are strongly populated.

An example for an electron distribution with non Gaussian tails is shown in figure 4.7. The Figures 4.8, 4.9 and 4.10 show the radiation fan, the critical energy profile and the photon distribution profile caused by this non Gaussian electron distribution.

The comparison of the critical energies and the populations of the photons on the edge of the radiation fans for the Gaussian and the non Gaussian electron distribution, explains the major importance of the knowledge of the electron distribution for the design of the beam pipe inside the H1 detector. The very high critical energies and population of the photons on the edge of the radiation fan, which are possible in the case of non Gaussian electron distribution, are a challenge to the design of the detector.

From the evaluation of the H1-luminosity measurements [52] as well as a dedicated measurement of the electron distribution [25], where the connection between the beam lifetime and the aperture, equation 2.24, was used to investigate the electron distribution, it can be concluded that the core of the electron distribution in HERA is Gaussian. But because of the nonlinear forces, one would expect non Gaussian tails of the electron distribution. In order to investigate the tails of the electron distribution, tail scan experiments at the HERA electron ring were carried out which are discussed in the next chapter.

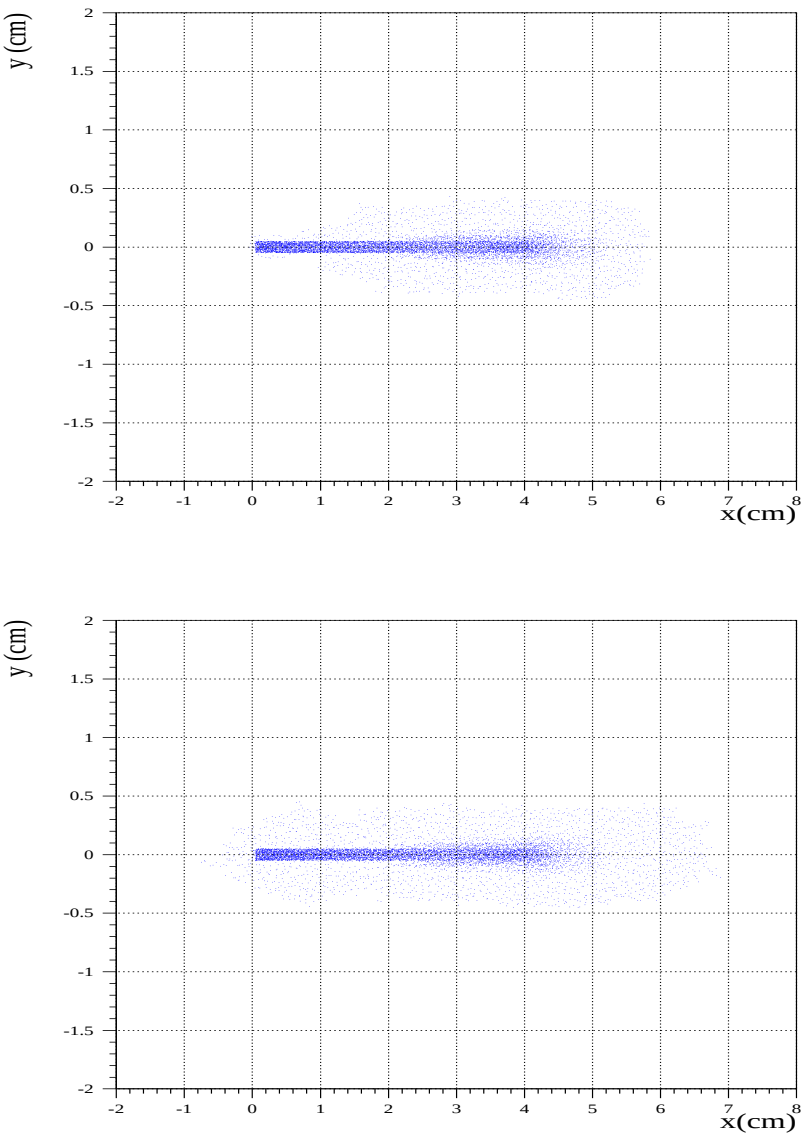

Figure 4.3: *The transverse profiles of the radiation fan at the position of the collimator C5B, top: the radiation caused by the core, bottom: the radiation caused by the whole electron distribution. The number of photons at the edge of the radiation fan in the top figure is by 5 order of magnitude larger than the number of photons at the edge of the radiation fan in the bottom figure.*

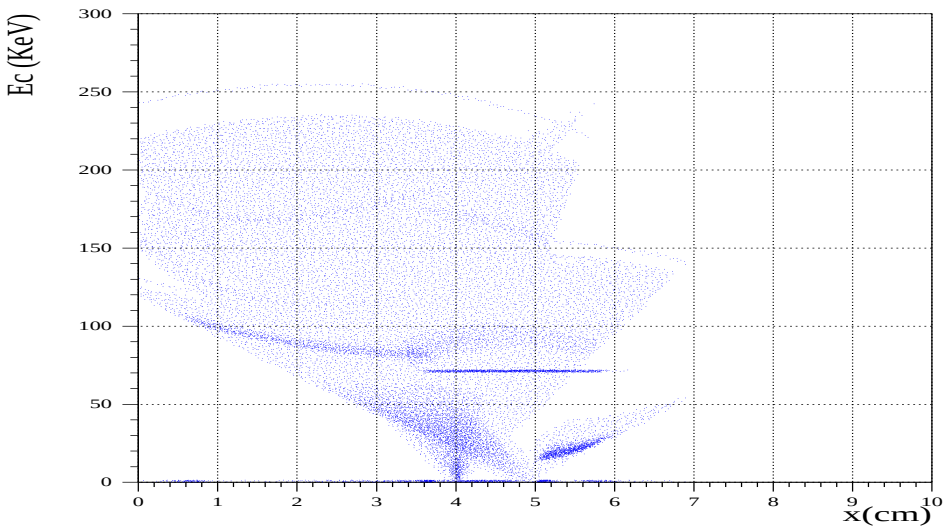

Figure 4.4: *The horizontal profile of the critical energy of the radiation fan at the position of the collimator C5B.*

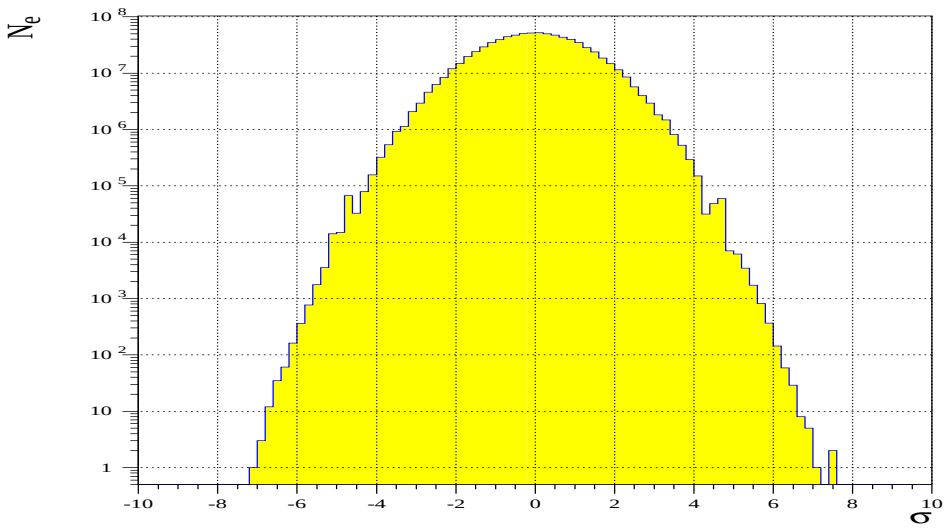

Figure 4.5: *Gaussian Electron Distribution*

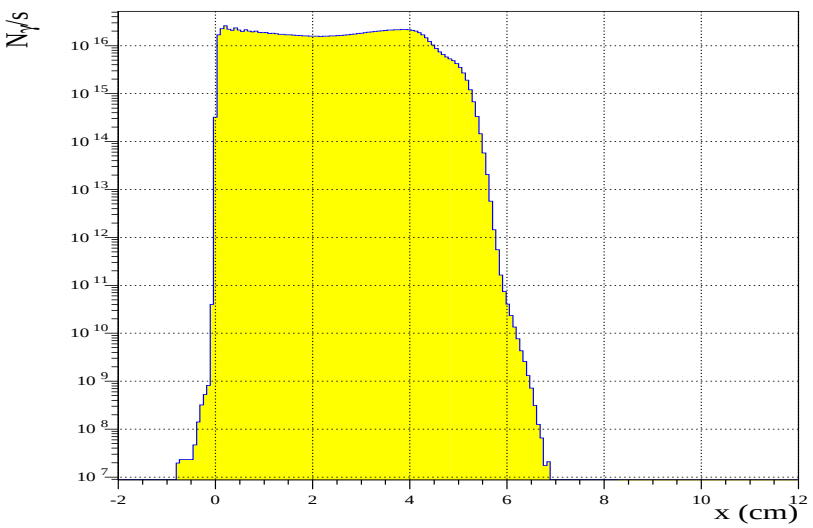

Figure 4.6: *The horizontal profile of the photon distribution at the position of the collimator C5B, for the electron distribution of the figure 4.5 .*

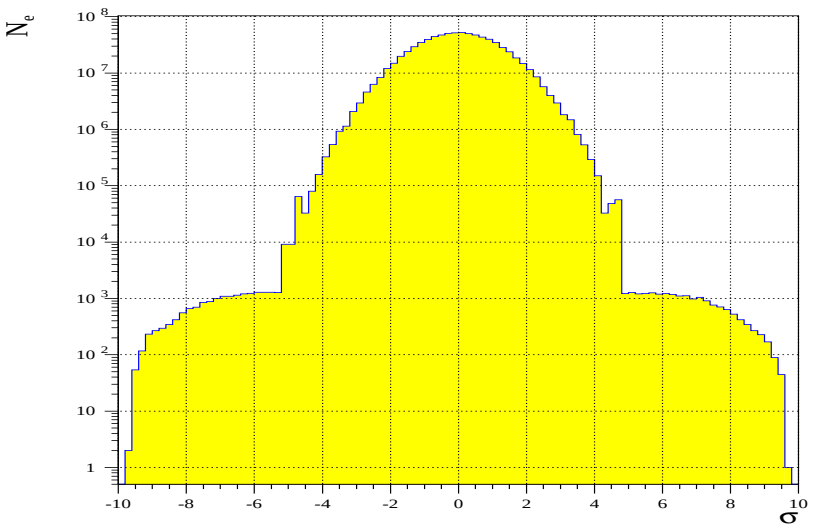

Figure 4.7: *An example for an electron distribution with non Gaussian tails. The core up to* 4 *standard deviation is Gaussian, the tail electrons are box-shaped distributed*

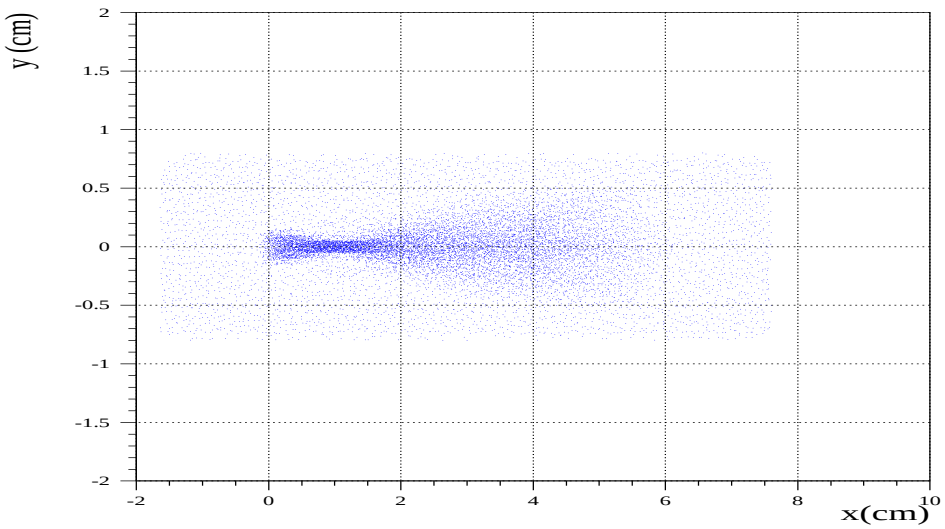

Figure 4.8: *The transverse profile of the radiation fan caused by the non Gaussian electron distribution of the figure 4.7 at the position of the collimator C5B.*

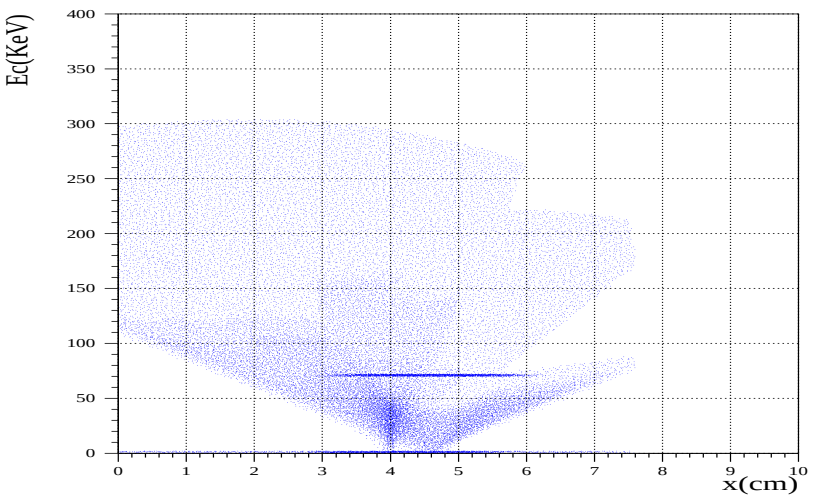

Figure 4.9: *The horizontal profile of the critical energy caused by the non Gaussian distribution of the fig. 4.7 at the position of the collimator C5B.*

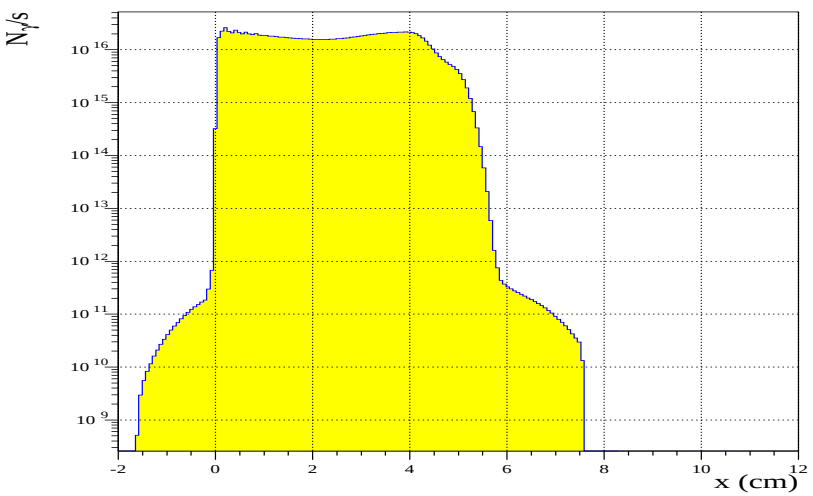

Figure 4.10: *The horizontal profile of the photon distribution caused by the non Gaussian distribution of the fig. 4.7 at the position of the collimator C5B.*

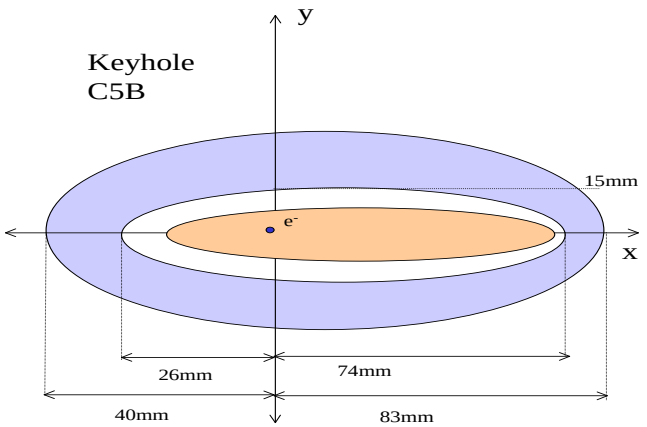

Figure 4.11: *A cross sectional view on the keyhole collimator C5B, with the electron beam and radiation fan. The collimator is designed such that the direct radiation fan of the figure 4.8 can pass.*

Chapter 5

Tail Scan Experiments at the HERA Electron Ring

During the luminosity operation of the HERA, protection of the detectors from the synchrotron radiation caused by the electron beam is necessary. In the present HERA configuration, a collimation system, which scrapes the direct radiation fan in front of the detector, is used to shield the H1 detector from the synchrotron radiation (see section 3.3).

After the luminosity upgrade, it will no longer be possible to collimate the radiation fan upstream the H1 detector. Therefore the synchrotron radiation fan has to pass through the experiment and the transverse dimensions of the beam pipe inside the H1 detector will be determined by the edge of the radiation fan, as already discussed in the section 4.2. Since the photons on the edge of the radiation fan are emitted by the electrons in the tail of the electron distribution, the tail distribution of the electron beam becomes more important than in the present configuration (see section 4.3).

It is possible to study the tail distribution by tail scan experiments. During a tail scan experiment the physical aperture is reduced by moving a scraper toward the beam in small steps. At each step the beam lifetime and the beam loss rate are measured. Such a tail scan yields information about particles which oscillate with an amplitude larger than the position of the scraper. In scope of this work, several tail scan experiments at the present HERA electron ring were carried out [29, 30]. These measurements were taken not only with the current focussing scheme of 60° phase advance per FODO cell in the arcs but also with the focussing scheme of 72° phase advance foreseen for the upgrade [28, 31].

The tail scan experiments are discussed in this chapter. The first section describes the measuring equipment. The measured results and the measurement errors are discussed in the second section. The last section of this chapter treats the evaluation of the tail scan measurements.

5.1 Measuring Equipment

During the tail scan experiments, the physical aperture is reduced by moving the scrapers gradually and the beam lifetime and the loss rates are measured by using the HERA beam current measurement and the Beam Loss Monitors, BLMs.

5.1.1 The Scrapers

In order to carry out the tail scan experiments, two scrapers were installed in the east section of the HERA electron ring in June 1999. Each of the scrapers has a horizontal and a vertical scraper jaw, so that it is possible to scrape the beam from above, below, the right side, and the left side. The cylindrical scraper jaws are made of copper and have a diameter of 30.0 mm. Figure 5.1 shows a technical drawing of such a device.

The scraper jaws are equipped with stepping motors so that they can be moved by remote control from the accelerator control room (BKR) in steps of 0.1 mm or 0.01 mm respectively.

5.1.2 The Beam Lifetime

The beam current measurement in the electron ring is a standard diagnostic tool in HERA, which is carried out by direct-current monitors. The beam current measurement is used to determine the beam lifetime in HERA [54]. Assuming a constant beam lifetime during the measuring time interval $t_2 - t_1 = 1\,\text{sec.}$, which is a good approximation for the time intervals of HERA beam current measurement of 1 sec, the lifetime τ_q can be obtained from the following formula:

$$\tau_q = \frac{t_2 - t_1}{\ln(I(t_1)) - \ln(I(t_2))},$$

where $I(t_1)$ and $I(t_2)$ are the electron beam currents at the times t_1 and t_2.

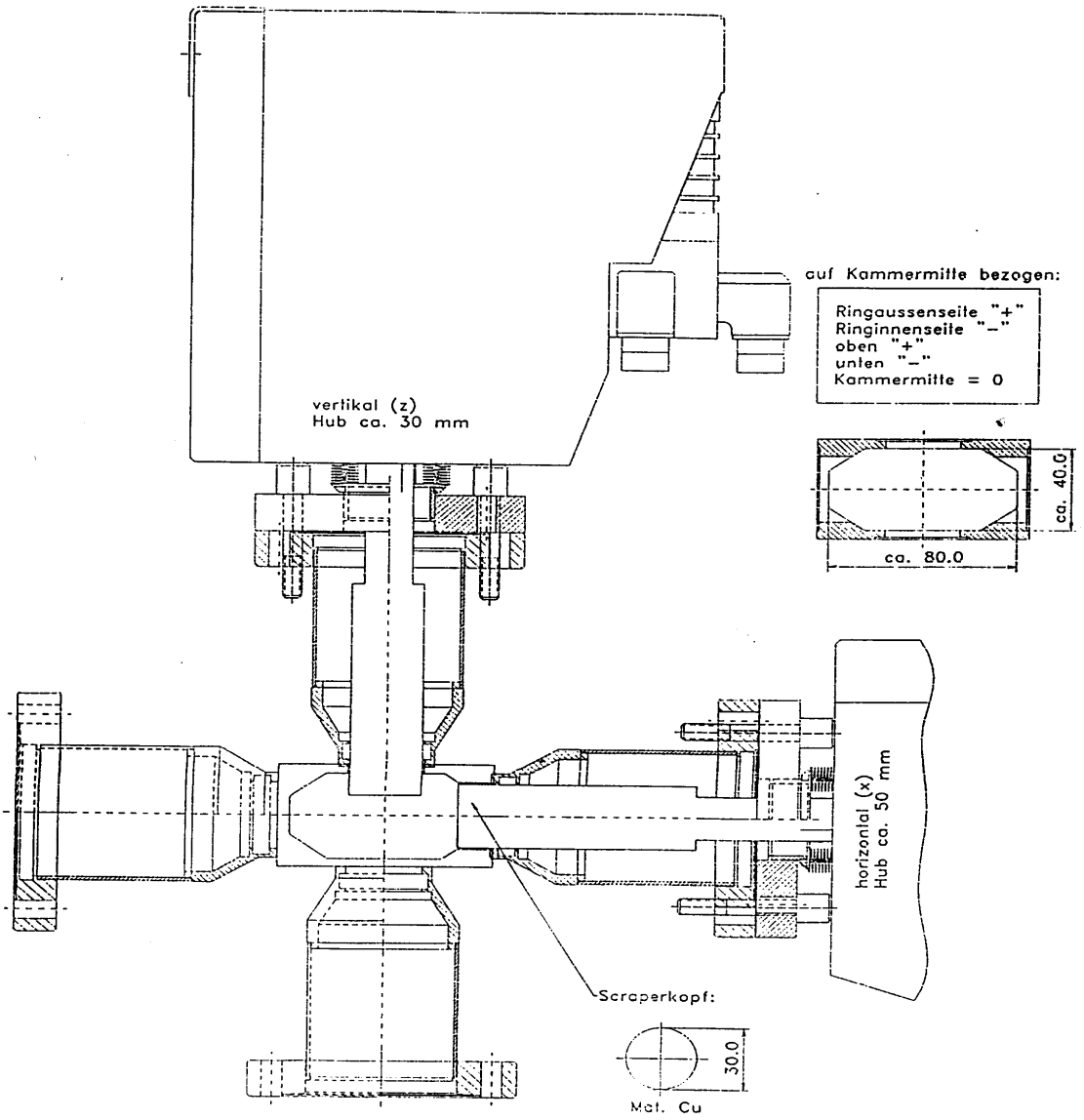

Figure 5.1: *A cross sectional view of the scraper in the HERA electron ring.*

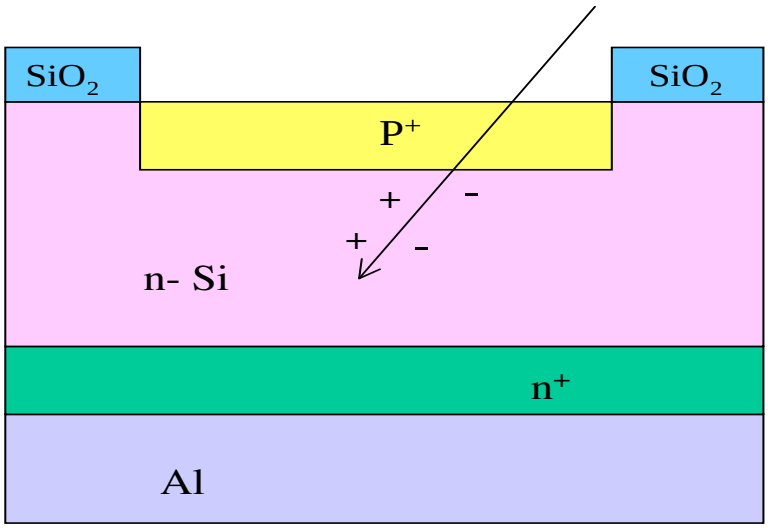

Figure 5.2: *A schematic cross section of a PIN photodiode. A voltage of +24 V is applied to the PIN photodiode. The PIN photodiodes have a surface of* $7,34\,mm^2$ *(large model) or* $150,mm^2$ *(small model) respectively.*

5.1.3 The Beam Loss Monitors

During the experiments the beam loss rates were measured by beam loss monitors, BLM. A HERA BLM consists of two face to face mounted PIN photodiodes, which are sensitive to charged particles and to the photons. A PIN photodiode is made of different layers of silicon. A voltage of +24 V is applied to the PIN photodiode. Figure 5.2 shows a schematic view of a PIN photodiode. If a charged particle passes through such a PIN photodiode, it ionizes the material along its track and produces a charge signal. In order to suppress electronic noise and the background from soft synchrotron radiation photons, which produce a signal in only one of the two PIN photodiodes, only a coincidence signal from both PIN photodiodes of the BLM is counted as a loss signal.

A maximum rate of about 13 MHz can be measured by the PIN photodiodes, which has to be compared with the HERA bunch separation corresponding to 10.5 MHz.

The sensitivity of the BLMs for detecting a lost electron is dependent on the solid angle which they cover, i.e. it is dependent on their locations with respect to the scraper jaws. The sensitivity of the BLMs which were used during the experiments was obtained from the beam current measurement and the measured data of the BLMs, as described in the next subsection.

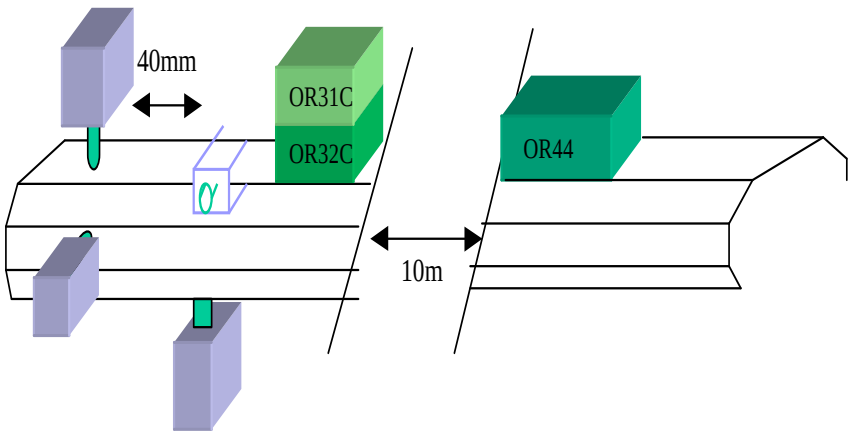

Figure 5.3: *A schematic view of the measurement device. The distance between the scrapers amounts to* 40 *mm; OR*44 *is the nearest regular electron ring BLM and has a distance of* 10 *m from the scrapers; the BLMs OR*44*, OR*31*C and OR*32*C have different sensitivity*

5.1.4 Measurement Device

The scrapers were installed in the east section 35 m downstream of the IP in a region with very small dispersions of $D_x = -24.5$ mm in the horizontal plane and $D_y = -14.1$ mm in the vertical plane. The distance between both scrapers amounts to 40 mm.

The nearest regular electron ring BLM, $OR44$, has a distance of 10 m from the scrapers. For the case that a saturation is reached in this BLM, two further BLMs, $OR31C$ and $OR32C$, were installed next to the scraper in addition to the regular HERA electron ring BLMs. These two BLMs have different sensitivity and are dedicated to the scraping experiments. Figure 5.3 shows a schematic view of the experiment setup.

For each measurement the date, the time, the beam lifetime, the beam current, the scraper position, and the counting rates of the BLMs were recorded in a file. During the measurements the scrapers were moved until lifetimes of the order of one hour were reached. In this regime the beam life-

time is determined by the losses on the scraper. Using the beam current and the data of the BLMs and taking into account the statistical background due to the accidental coincidence, the sensitivity of the BLMs can be calculated by the following formula:

$$N_{dplp} = \frac{N_{BLM} - N_{BLM_0}}{N_{I0} - N_I},$$

where N_{dplp} is the number of the detected particles per lost particle, N_{BLM} is the loss rate of the BLMs measured at a lifetime of one hour, N_{BLM_0} is the measured loss rate of the BLMs by totally removed scraper jaws corresponding to lifetimes of the order of fifteen hours, N_I is the total number of lost electrons obtained from beam current measurements at the lifetime of one hour, and N_{I0} is the total number of lost electrons by totally removed scraper jaws. The sensitivity of the BLMs is given in the table 5.1.

Table 5.1: Detected particles per lost particles

Scraper Position	Monitor OR44	Monitor OR32C	Monitor OR31C
Outside	$3.9 * 10^{-5}$	$3.2 * 10^{-6}$	$2.6 * 10^{-7}$
Inside	$3.6 * 10^{-5}$	$3.2 * 10^{-6}$	$2.6 * 10^{-7}$
Top	$4.5 * 10^{-5}$	$6.8 * 10^{-6}$	$4.1 * 10^{-7}$
Bottom	$4.0 * 10^{-5}$	$4.4 * 10^{-6}$	$2.1 * 10^{-7}$

5.2 Results and the Measurement Errors

At the present HERA electron ring, where the focussing scheme of 60° phase advance per FODO cell in the arcs is used, the following tail scan measurements were carried out:

- horizontal and vertical tail scans on a 27.5 GeV positron beam. The magnets of the proton ring had luminosity conditions, i.e they had the fields which are necessary for a 920 GeV proton beam. But the protons were not filled, i.e. without beam-beam interaction.

- horizontal and vertical tail scan measurements on a 27.5 GeV positron beam under regular luminosity conditions with a proton current of 101,3 mA, i.e. with beam-beam interaction.

In view of the luminosity upgrade project, tail scan experiments were carried out in two cases, where the upgrade focussing scheme of 72° phase advance per FODO cell in the arcs was used:

- horizontal and vertical tail scraping on a 27.5 GeV positron beam. In this case the magnets of the proton ring had luminosity conditions but the protons were not filled, i.e. no beam-beam interaction acted.
- horizontal and vertical tail scraping on a 27.5 GeV positron beam under luminosity conditions with a proton current of 64.33 mA, i.e. with beam-beam interaction.

The figure 5.4 shows the loss rates of the BLM $OR44$ as a function of the horizontal scraper position for the case of the 60° focussing scheme with and without beam-beam interaction. In the figure 5.5 the loss rates as a function of the vertical scraper position with and without beam-beam interaction are shown. The figures 5.6 and 5.7 show the results of the measurements with the 72° focussing scheme. The loss rates of the BLMs $OR32C$ and $OR31C$ as functions of the scraper positions can be found in the Appendix D.

From the figures 5.4 - 5.5, it can be seen, that the loss rates increase first very slowly with the decreasing scraper position. This increase becomes stronger before the connection between the loss rates and the scraper position becomes exponential.

In order to interpret the measured data, the experimental errors on the measurements have to be taken into account. The most important sources of errors for the tail scan experiments in the HERA electron ring are: the uncertainty in the determination of the scraper jaw position, the inaccuracy of the beam lifetime, the errors caused by the different geometrical positions of the scraper jaws, the background caused by synchrotron radiation, and the orbit movement.

The uncertainty in the determination of the distance between the scraper jaw and the vacuum chamber wall amounts to 2 μm [43]. Compared with the expected standard deviations of the order of several 100 μm in the electron ring, this uncertainty can be neglected.

The uncertainty in the distance determination for two opposite scraper jaws amounts to 100 μm [43]. In order to obtain the standard deviation, the scraping experiments were carried out from both sides in each plane.

The beam lifetime measurement in the electron ring relies on the beam current measurement, which is taken by integration of the beam losses during

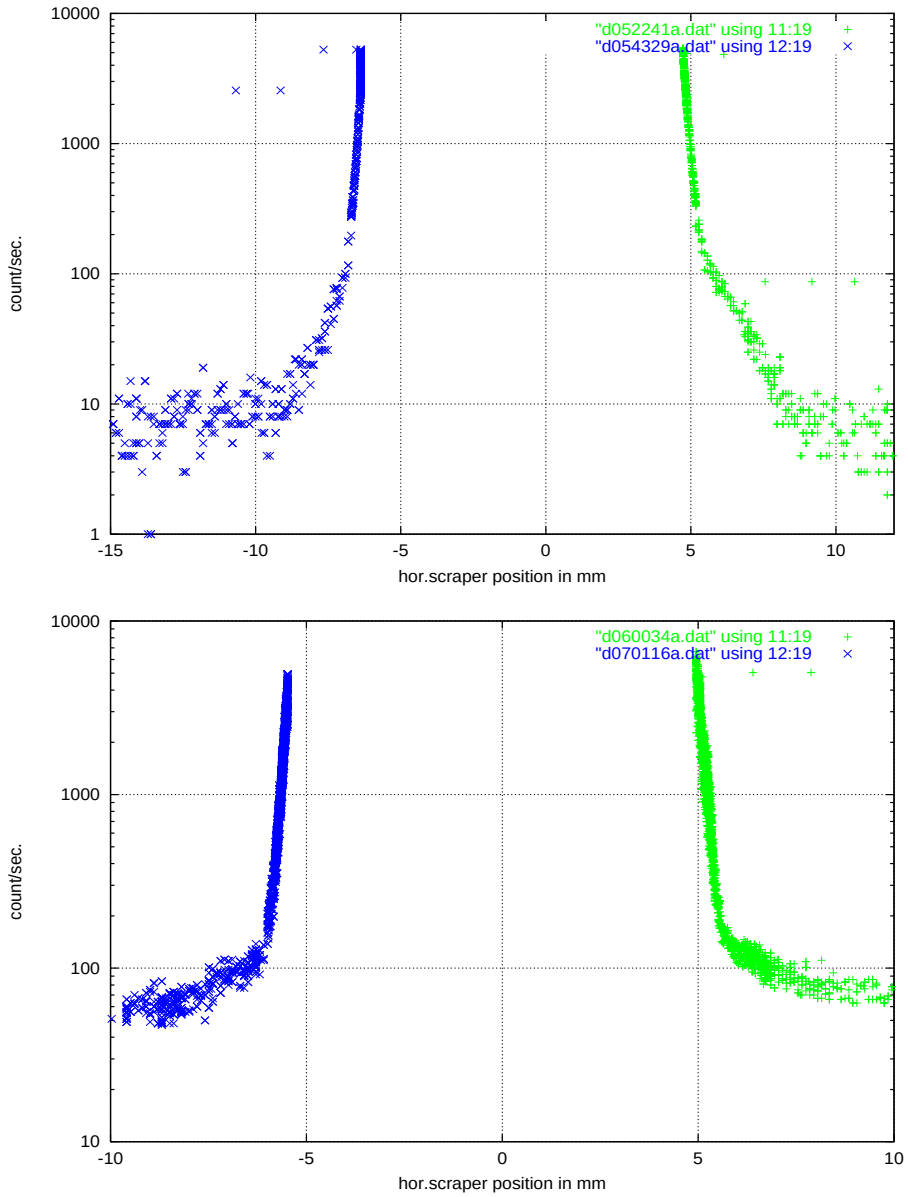

Figure 5.4: *Beam loss rates of monitor OR44 in counts per second versus horizontal scraper position in mm, with* 60° *focussing scheme, top: without beam-beam interaction, bottom: with beam-beam interaction.*

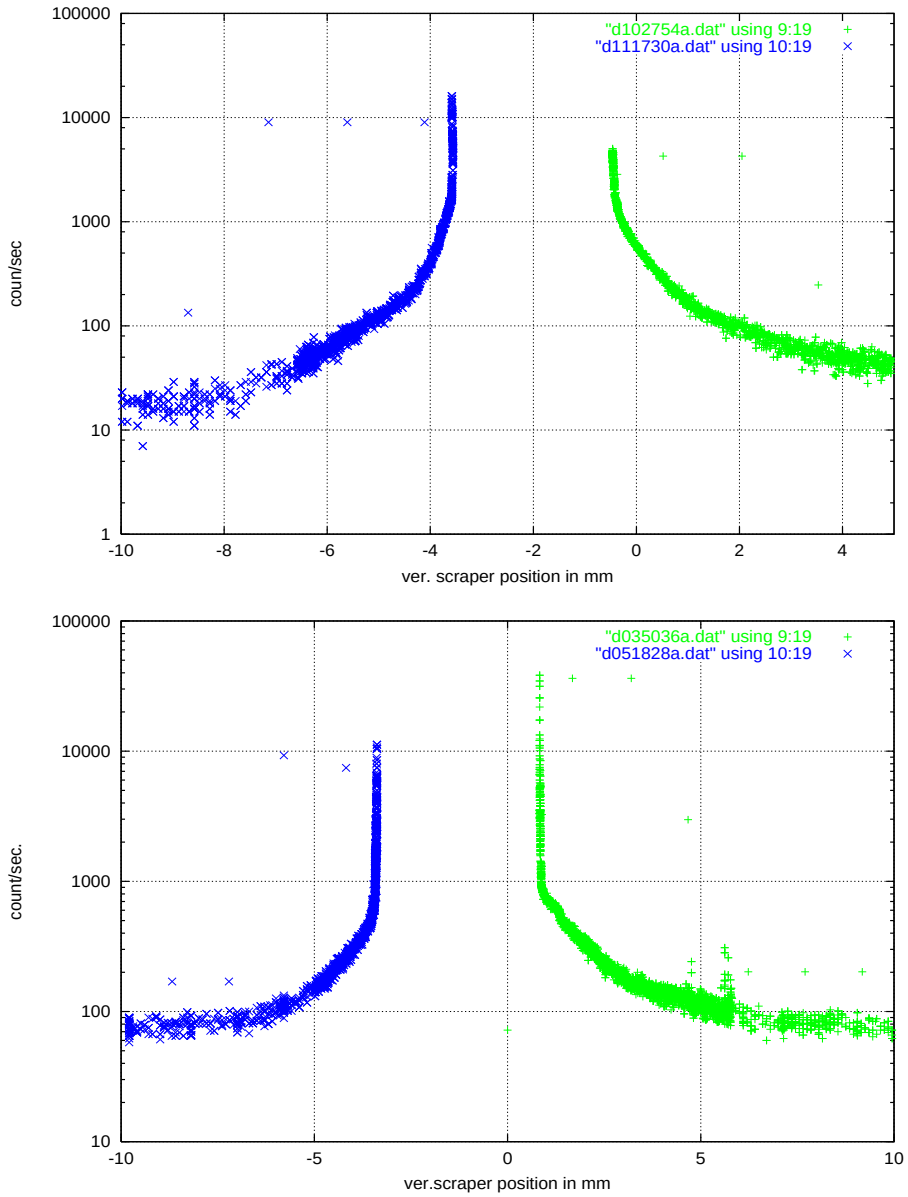

Figure 5.5: *Beam loss rates of monitor OR44 in counts per second versus vertical scraper position in mm, with 60° focussing scheme, top: without beam-beam interaction, bottom: with beam-beam interaction.*

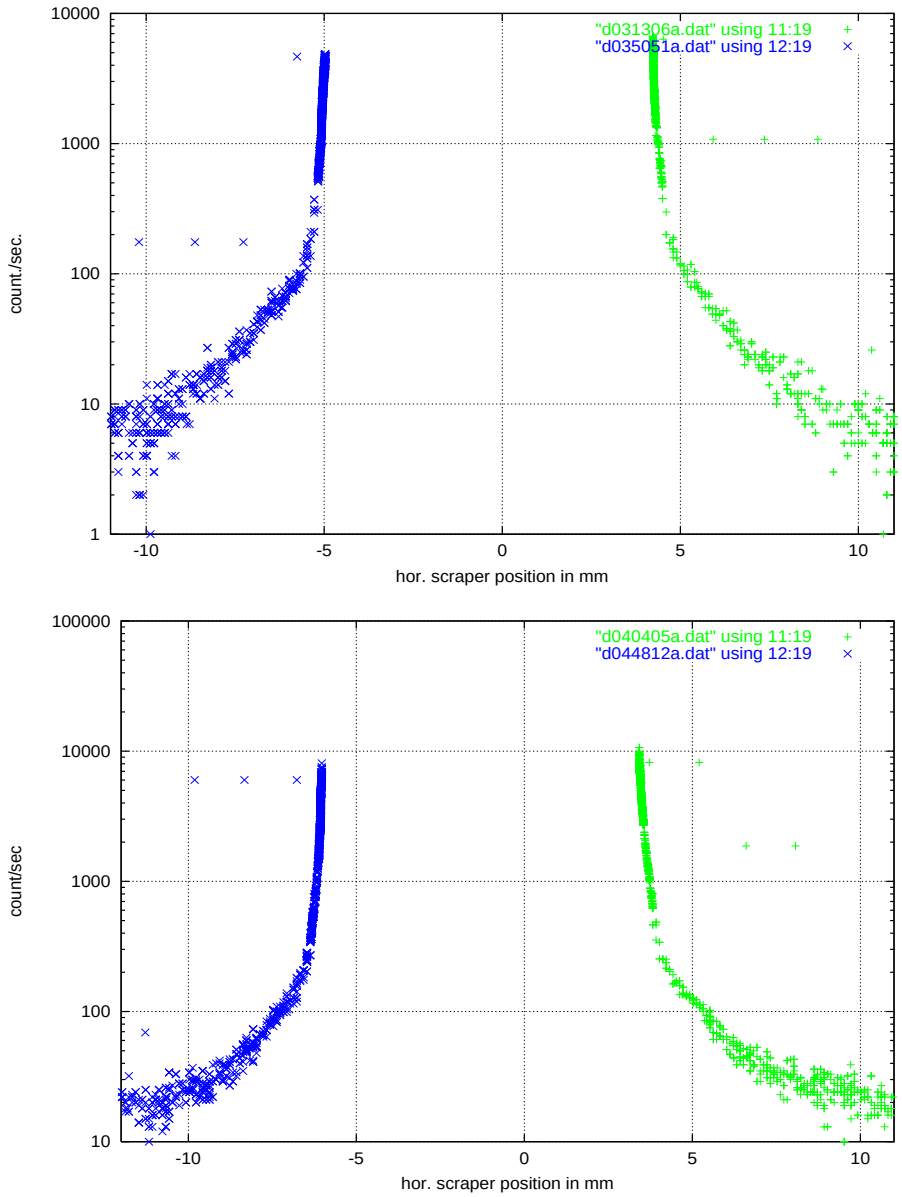

Figure 5.6: *Beam loss rates of monitor OR44 in counts per second versus horizontal scraper position in mm, with 72° focussing scheme, top: without beam-beam interaction, bottom: with beam-beam interaction.*

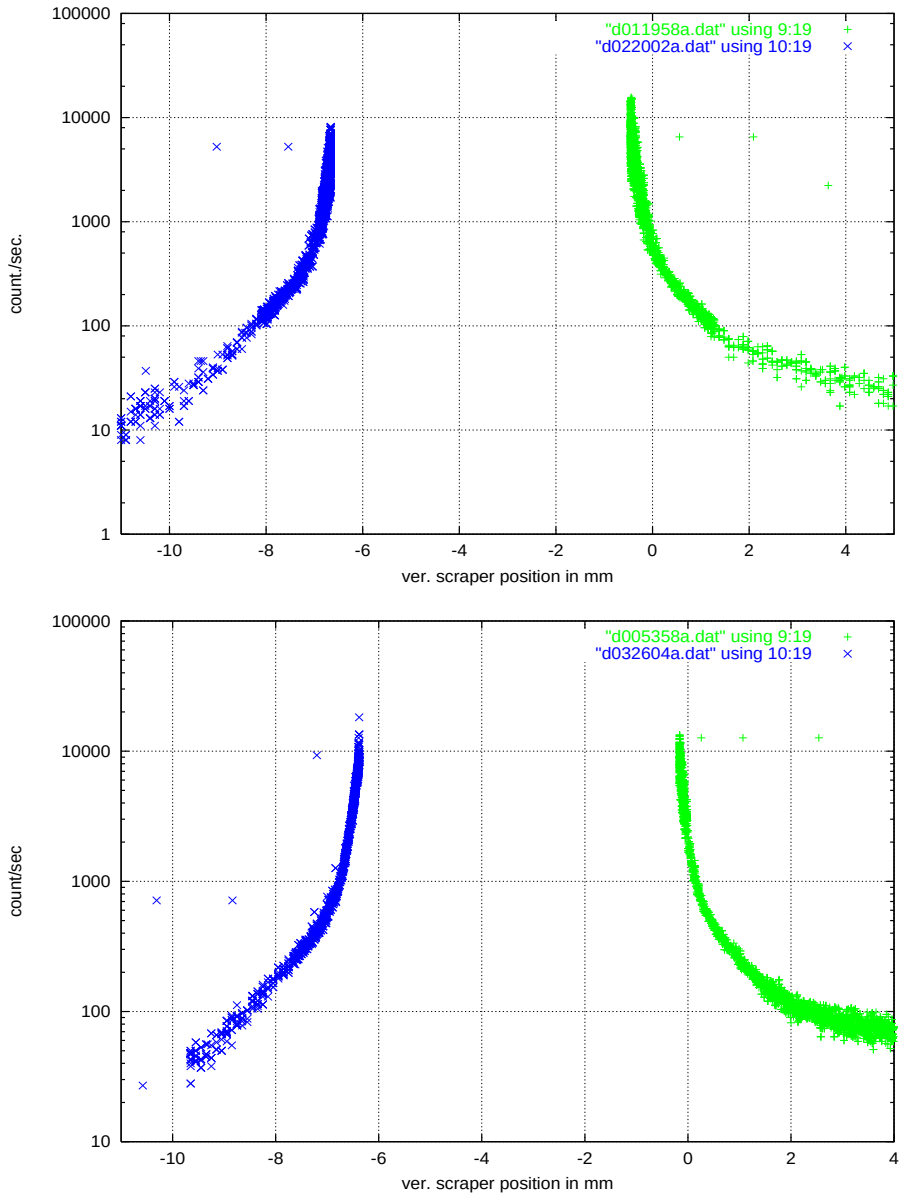

Figure 5.7: *Beam loss rates of monitor OR44 in counts per second versus vertical scraper position in mm, with 72° focussing scheme, top: without beam-beam interaction, bottom: with beam-beam interaction.*

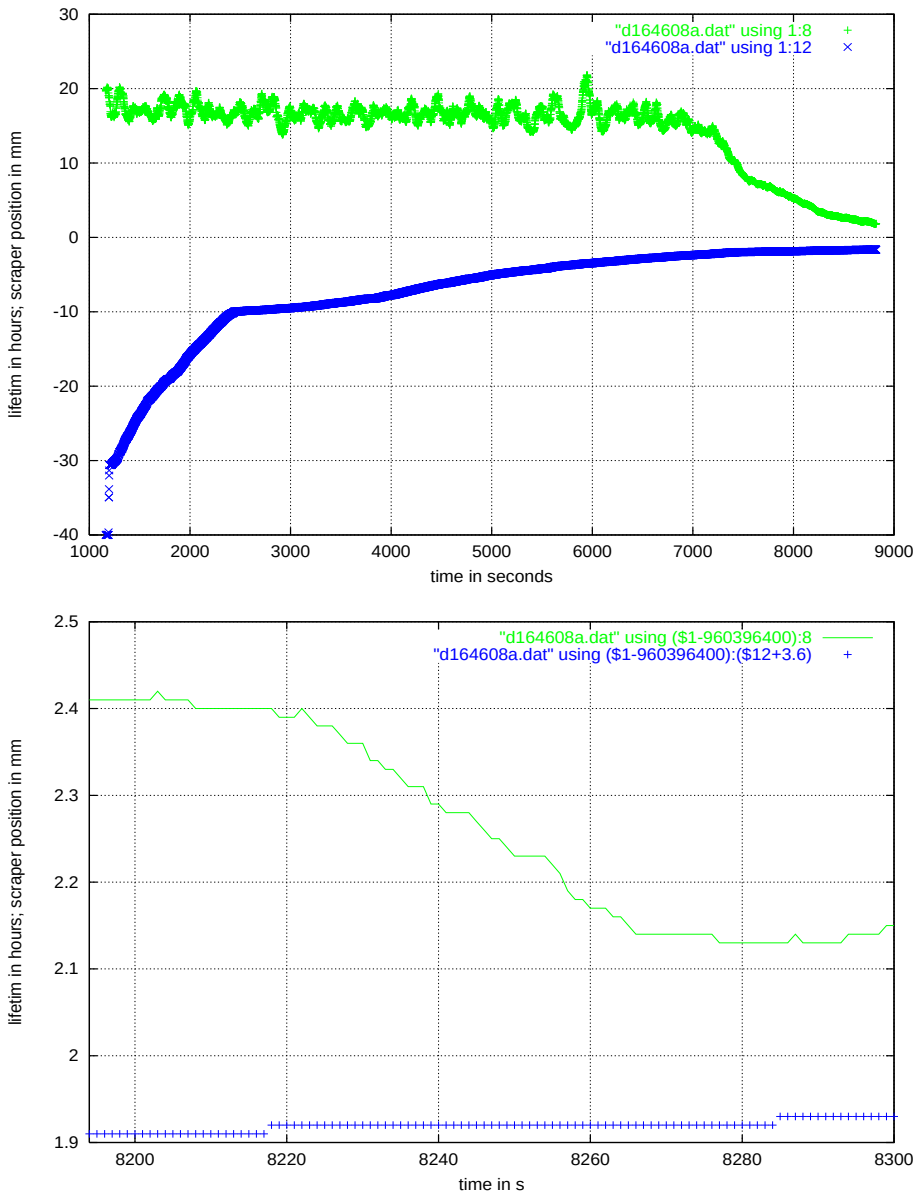

Figure 5.8: *Black(++): Scraper position versus time; grey(–): beam lifetime versus time. In the bottom figure, a part of the top figure is zoomed in. The scraper position was kept until the lifetime measurement stabilized, as shown in the figure below.*

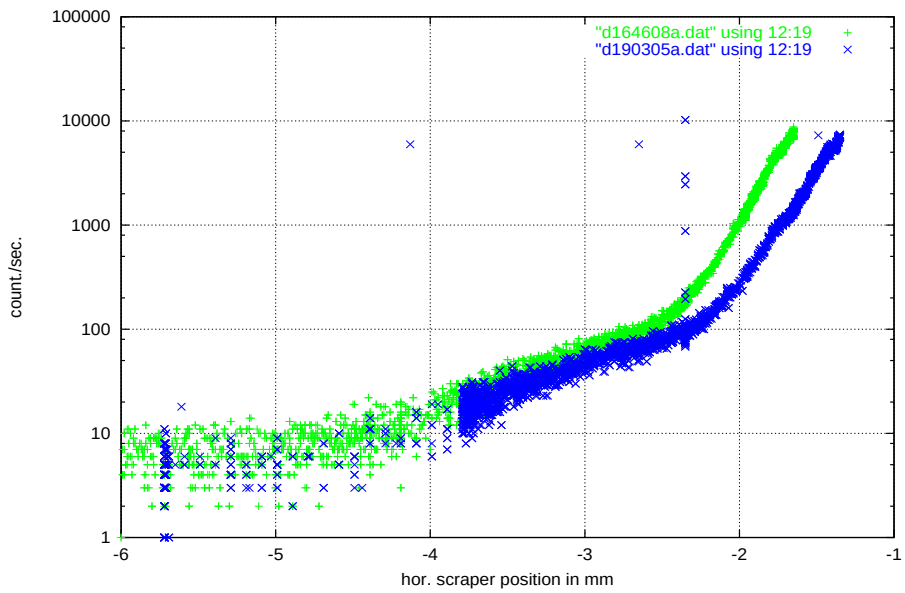

Figure 5.9: *Beam loss rates versus scraper position, black: first measurement, grey: second measurement. During the second measurement the orbit moved about* 0.30 *mm in* 4721 *s.*

a short time interval [54]. This led to jitters of the beam lifetime about a mean value during the measurements, as shown in figure 5.8. In order to minimize the errors caused by this effect, the scraper position was kept until the lifetime measurement was stabilized (see fig. 5.8). The remaining uncertainty of the lifetime measurement amounts to 0.1 hour, which give rise to an error in order of 0.001 mm in the standard deviation. This error is negligible.

Since the sensitivity of the BLMs is experimentally determined, as described in the last section, the errors caused by the different location of the scraper jaws with respect to the BLMs are already taken into account in the determination of the BLM sensitivity.

The accidental coincidence can lead to errors in the loss rates. Since this is a statistical effect, the errors caused by it are inversely proportional to the square root of the loss rates. Therefore they are relevant only for small loss rates, i.e. in the tail region. The experiment setup was installed in a straight section far away from the sources of synchrotron radiation to minimize the number of photons which can lead to a accidental coincidence signal.

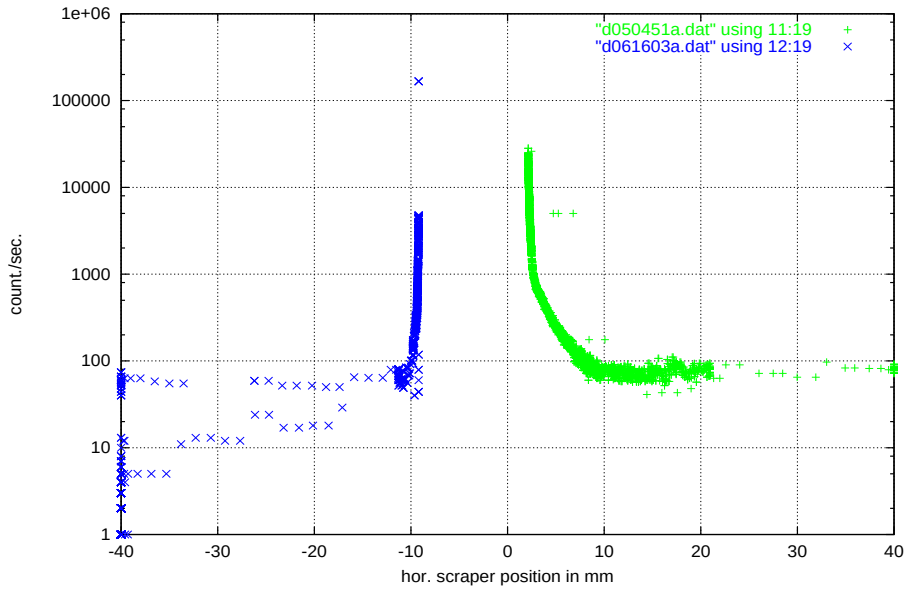

Figure 5.10: *Beam loss rates versus scraper position. The orbit movement causes an artificial asymmetry in the measurement results*

The change of beam orbit with time is a known effect in the HERA electron machine. Thermal effects are the probable cause of the orbit motion. For more details see [26]. Figure 5.9 shows a good example for such an orbit movement. Two successive tail scan measurements are shown, where the measurements were carried out with the same scraper on the same electron beam. During this experiment the orbit moved by about 0.30 mm in 4721 sec., i.e. $1.34 \cdot 10^{-12}$ m per turn. The orbit movement can cause an artificial asymmetry in the measurement results (see figure 5.10).

A tail scanning in a plane takes about 3 hours, i.e. 1.5 hour for each side. For the time interval of 1.5 hour, orbit movements in the order of 0.01 mm are observable. In order to avoid artificial asymmetries, the orbit was carefully observed during the measurements, so that measurements with orbit movements larger than 0.03 mm per hour were sorted out.

The uncertainty of the distance determination of the opposite scraper jaws, the synchrotron radiation background (only in the tail region), and the very small orbit movement are the essential sources of the measurement errors.

5.3 Evaluation

In the absence of nonlinear forces, beam-gas scattering, and aperture limitations, the electron density distribution would be a Gaussian, as already discussed in chapter 2.

In the experiments the closest distance between scraper and beam was chosen to yield a lifetime of about 1 hour. In this lifetime regime not only the tails but also the core of the transverse beam distribution is scraped.

Neglecting the very small dispersions of $D_x = -24.5\,\mathrm{mm}$ and $D_y = -14.1\,\mathrm{mm}$ at the location of the scraper, the equation 2.24 , which connects the beam lifetime, the scraper position corresponding to the physical aperture, and the standard deviation of the transverse beam distribution, can be used to calculate the variance of the transverse distribution.

Figure 5.11 shows the beam calculated lifetime as a function of the aperture limitation in units of the horizontal or the vertical standard deviation respectively. For these plots the damping times $\tau_x = 1.43 \cdot 10^{-2}\,\mathrm{sec.}$ and $\tau_y = 1.33 \cdot 10^{-2}\,\mathrm{sec.}$ are used, which are computed by the program MAD for the nominal center frequency $f_{RF} = 499667973\,\mathrm{Hz}$ of the RF system for the 60° and the 72° focussing scheme. When the frequency of the RF system is 154 Hz lower, as the central frequency measurements in 1998 suggest [27], the computed damping times are $\tau_x = 1.75 \cdot 10^{-2}\,\mathrm{sec.}$ and $\tau_y = 1.33 \cdot 10^{-2}\,\mathrm{sec.}$ for both focussing schemes. From figure 5.11, it is concluded that in the case of the 60° focussing scheme a lifetime of two hours corresponds to a horizontal aperture of $5.77\sigma_x$. Comparing this value with the measured scraper position at which the beam lifetime is two hours, the standard deviation of the horizontal beam distribution can be obtained. For example in the bottom plot of the figure 5.4, the measured scraper positions at which the beam lifetime is two hours are 4.95 mm and −5.49 mm respectively:

$$2 \times 5.77\sigma_x = (|-5.49|+4.95)\,mm \pm 0.1\,mm, \quad \Rightarrow \sigma_x = 0.905\,mm \pm 0.009\,mm.$$

The error of ±0.1 mm is the uncertainty in the distance determination of the opposite scraper jaws. Because of the very high loss rates in this lifetime regime, the loss rate errors caused by the radiation background can be ignored. The errors caused by the orbit movements in order of about 0.01 mm per hour are also neglected. In this way the standard deviations of the horizontal and vertical beam distributions are obtained for the 60° and the 72° focussing scheme.

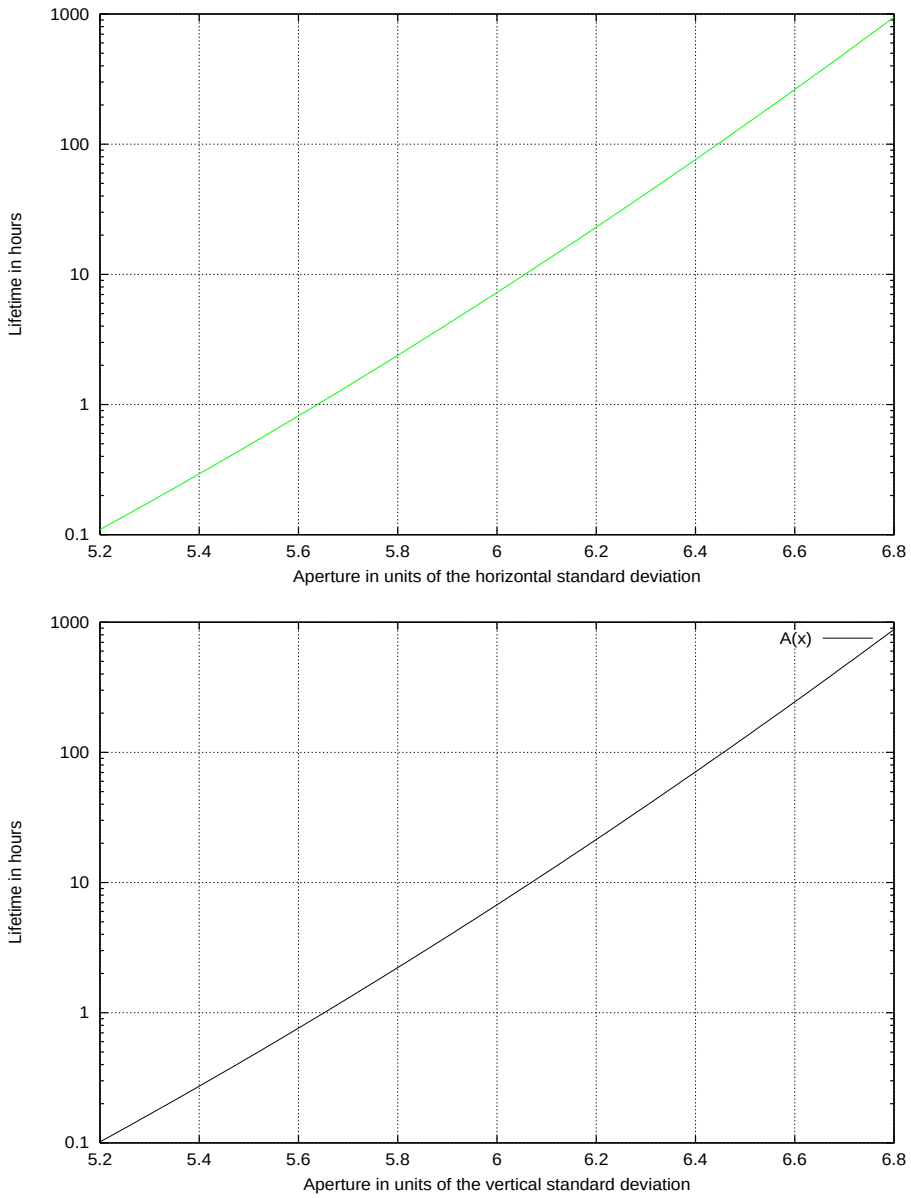

Figure 5.11: *Lifetime versus aperture limitation in units of the horizontal or the vertical standard deviation respectively, for the* 60° *focussing scheme, with beam-beam interaction*

Table 5.2: The theoretical and the measured standard deviation of the transverse beam distribution, without beam-beam interaction

with focussing scheme	σ_x 60°	σ_y 60°	σ_x 72°	σ_y 72°
theoretical with $\Delta f_{RF} = 0Hz$	0.843mm	0.089mm	0.731mm	0.089mm
theoretical with $\Delta f_{RF} = 154Hz$	0.953mm	0.089mm	0.810mm	0.089mm
measured	0.950mm $\pm$0.009mm	0.268mm $\pm$0.009mm	0.800mm $\pm$0.009mm	0.537mm $\pm$0.009mm

Table 5.3: The theoretical and the measured standard deviation of the transverse beam distribution, with beam-beam interaction

with focussing scheme	σ_x 60°	σ_y 60°	σ_x 72°	σ_y 72°
theoretical with $\Delta f_{RF} = 0Hz$	0.841mm	0.085mm	0.746mm	0.085mm
theoretical with $\Delta f_{RF} = 154Hz$	0.950mm	0.091mm	0.827mm	0.085mm
measured	0.905mm $\pm$0.009mm	0.370mm $\pm$0.009mm	0.822mm $\pm$0.009mm	0.539mm $\pm$0.009mm

The table 5.2 gives the measured and the theoretical standard deviations for the cases, where no beam-beam interaction acts, while the table 5.3 gives the measured and theoretical standard deviations with beam-beam interaction. The theoretical values for the standard deviation of the electron distribution were determined by the program MAD, where the β-beat due to the linear beam-beam force is taken into account. The table 5.4 shows the calculated beta functions at the scraper position for both focussing schemes with and without beam-beam interaction. Since the measurements in 1998 [27] suggest that the frequency of the RF system is roughly 154 Hz lower than the central frequency, $f_{RF} = 499667973$ Hz, corresponding to the design orbit, the theoretical values for the standard deviation were also simulated with this frequency shift.

Table 5.4: The beta functions at the position of the scrapers for both focussing schemes with and without beam-beam interaction

with focussing scheme	β_x 60°	β_y 60°	β_x 72°	β_y 72°
without beam-beam interaction	17.31m	30.58m	15.24m	30.29m
with beam-beam interaction	17.26m	31.10m	15.90m	29.21m

For the 60° and the 72° focussing schemes, the measured horizontal standard deviations agree well with the simulated values which have a frequency shift of 154Hz without beam-beam interaction. In the case of the 72° focussing scheme and with beam-beam interaction the measured horizontal standard deviation agrees with the simulated value for a frequency shift of 154 Hz. For the 60° focussing scheme with beam-beam interaction, the measured horizontal standard deviation does not agree with the simulated values. It is smaller than the simulated standard deviation with frequency shift and it is also smaller than the measured standard deviation without beam-beam interaction. This is surprising, since one would not expect a reduction of the horizontal emittance due to the beam-beam interaction. A beat of the beta function caused by the nonlinear beam-beam interaction could lead to this discrepancy.

For both focussing schemes the measured vertical standard deviations are larger than the simulated values. The nonlinear forces and the magnet misalignments can lead to a coupling between the horizontal and vertical betatron oscillations, which can explain the large vertical standard deviations. Note that vertical standard deviation in the case of the 60° focussing scheme is with beam-beam interaction larger than without beam-beam interaction. A coupling of the betatron oscillations due to the nonlinear component of the beam-beam force can be the cause for this.

The electrons suffer energy changes or deflection due to the collisions inside the bunch or by the collision with the residual gas molecules. These can lead to a reduction of the beam lifetime, as discussed in the section 2.4. The connection between the beam lifetime contribution due to the Touschek and the beam-gas scattering and the transverse aperture is given by the equations 2.27, 2.37.

The lifetime τ of the electron beam is determined by the lifetime τ_{qz} of a Gaussian distribution inside the physical aperture and the lifetime τ_{gas} due

to the beam-gas scattering as well as the lifetime τ_{Tou} due to the Touschek scattering if the transverse aperture limits the momentum acceptance as discussed in section 2.4.:

$$\frac{1}{\tau} = \frac{1}{\tau_{qz}} + \frac{1}{\tau_{gas}} + \frac{1}{\tau_{Tou}}.$$

The connection between the total electron losses ΔN and the lifetime τ is given by:

$$\Delta N = N_0 \cdot \left(1 - e^{\frac{\Delta t}{\tau}}\right)$$

where N_0 is the initial number of electrons, and $\Delta t = 1$ sec is the time interval during which the electron losses are accumulated.

Using the above formulas, the loss rates as functions of the scraper positions are calculated. The contribution of the Touschek scattering to the beam lifetime is in order of 1000 hours and it is taken into account only in those cases, where the transverse aperture limitation due to the scraper limits the momentum acceptance.

The measured and calculated loss rates as functions of the corresponding scraper positions are shown in the figures 5.12 - 5.15.

From the figures 5.12 - 5.15 it is to be seen that the measured loss rates can not be explained only by a Gaussian distribution with additional tail population due to the scattering processes. The nonlinear resonances in particular of third order excited by the sextupoles, can also give rise to additional non Gaussian tails. The higher order resonances depend on the distribution of the sextupoles around the accelerator.

In order to investigate the influence of the nonlinear resonances on the electron distribution, tracking simulations with the program MAD are performed. Thereby a *chromaticity* of $\xi_x = \xi_y = 2$ in both planes are chosen and the tunes which were adjusted during the measurement are put in. Each of the figures 5.16 - 5.19 shows the simulated electron distribution in the phase space (x, p_x) and its projection on the x-axis, as well as the matching measured data.

The simulated tails in the figures 5.16 and 5.17 are symmetric and populated already at large x-values. The simulated tails in the figure 5.19 are also symmetric but they are very small at large x-values, whereas the simulated tails in the figure 5.18 form two symmetric shoulder next to the main distribution.

From figures 5.16 and 5.17, it can be concluded that in the case of the 72° focussing scheme, the discrepancies between the calculated and the measured

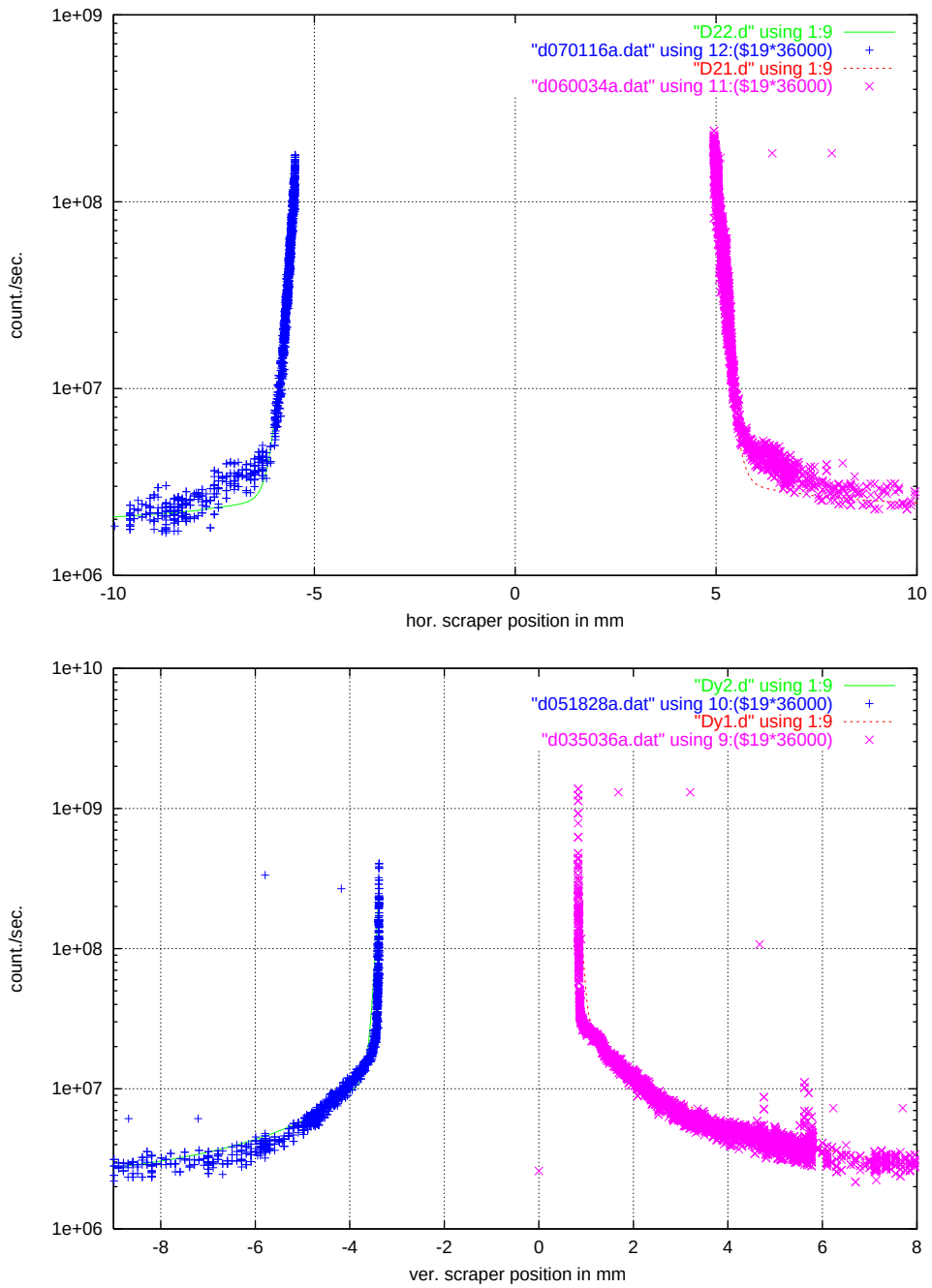

Figure 5.12: *Measured (+,×) and the calculated (line) beam loss rates versus scraper position, with the* 60° *focussing scheme and with beam-beam interaction*

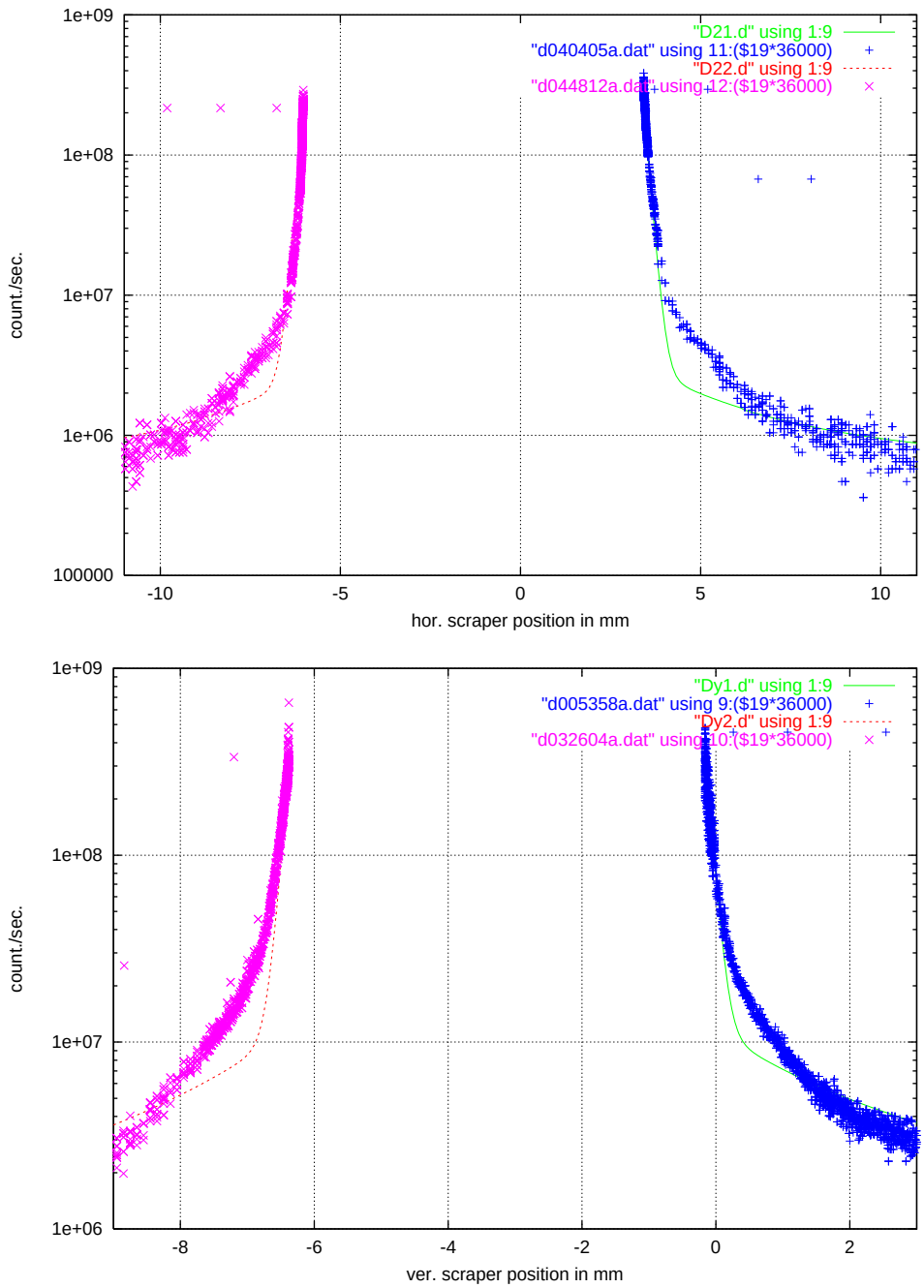

Figure 5.13: *Measured (+,×) and the calculated (line) beam loss rates versus scraper position, with the 72° focussing scheme and with beam-beam interaction*

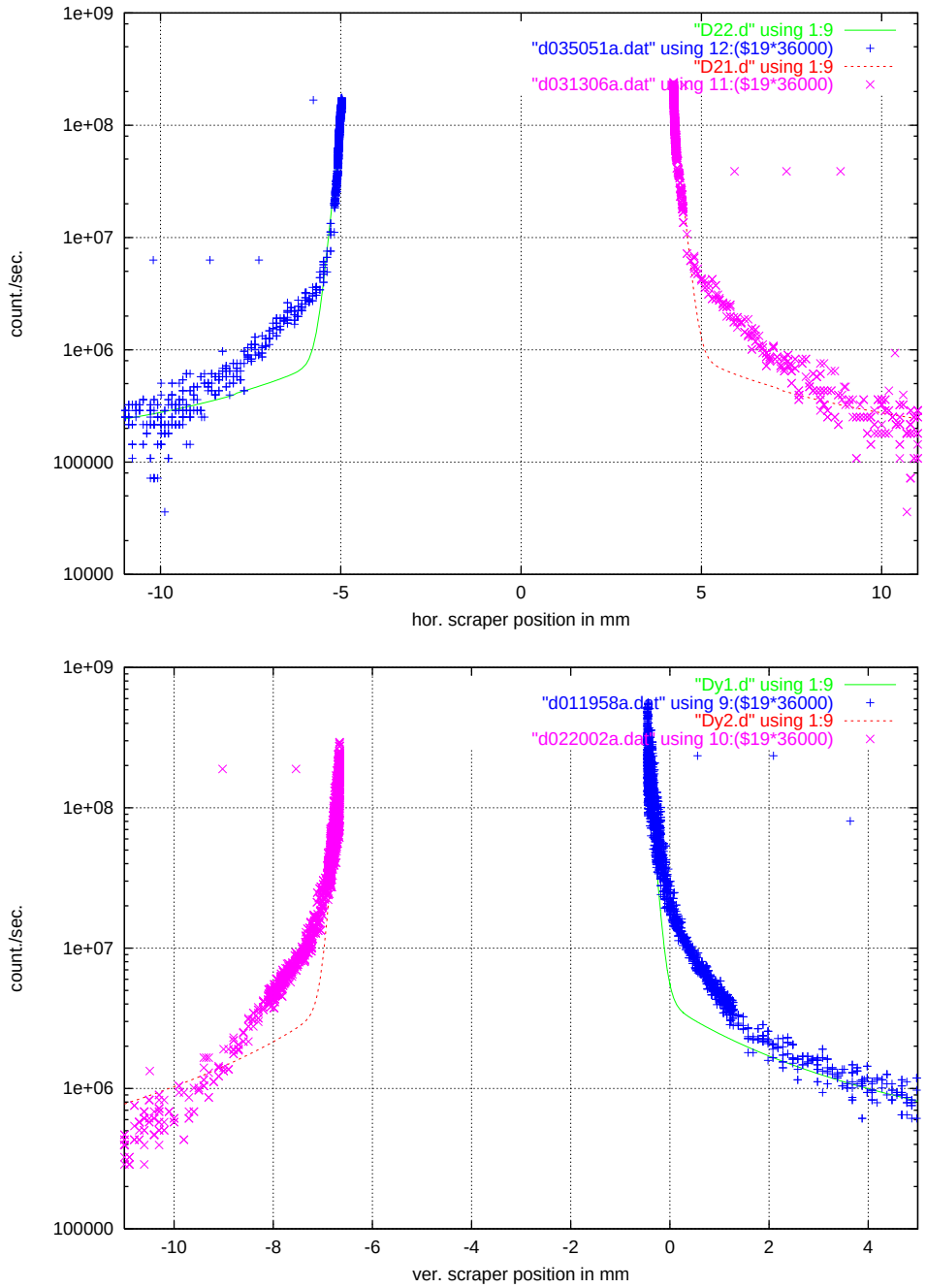

Figure 5.14: *Measured (+,×) and the calculated (line) beam loss rates versus scraper position, with the 72° focussing scheme without beam-beam interaction*

loss rate might be explained by the nonlinear resonances. This is also the case for the 60° focussing scheme with beam-beam interaction, see figure 5.19. In the case of the 60° focussing scheme without beam-beam interaction, figure 5.18, there exists an asymmetric shoulder about $x = +5\,\mathrm{mm}$, which could not be reproduced in the simulation. In the program MAD only the dipoles, quadrupoles and sextupoles of the HERA electron ring are taken into account. Additional nonlinear fields, for example due to the common electron proton magnets in the interaction sections, are not included. Such nonlinear field which exists in the real HERA, but is not included in the simulation program might lead to the asymmetric shoulder.

Note that the horizontal tune in the case of the 72° optic without the beam-beam interaction, figure 5.16, is next to $Q_x = 1/6$, which lead to the star shaped phase space distribution. The edge of the star are given by the unstable fixed points in the phase space. In the program MAD only the sextupol magnets can lead to nonlinear resonances, which cause fixed points in the phase space. Since the fractional horizontal tune of $Q_x = 0.1668$ is far away from the $1/3$, the effect of the sextupoles can not be treated with the first order perturbation theory described in the section 2.5. The second order perturbation theory, which has to be used in such cases, is more complicated. Tracking simulations are therefore a good alternative to the theoretical treatment

A measurable influence of the beam-beam interaction on the electron tails could not be observed. It might be that the non Gaussian tails caused by the other processes, which are described above, mask the effect of the beam-beam interaction.

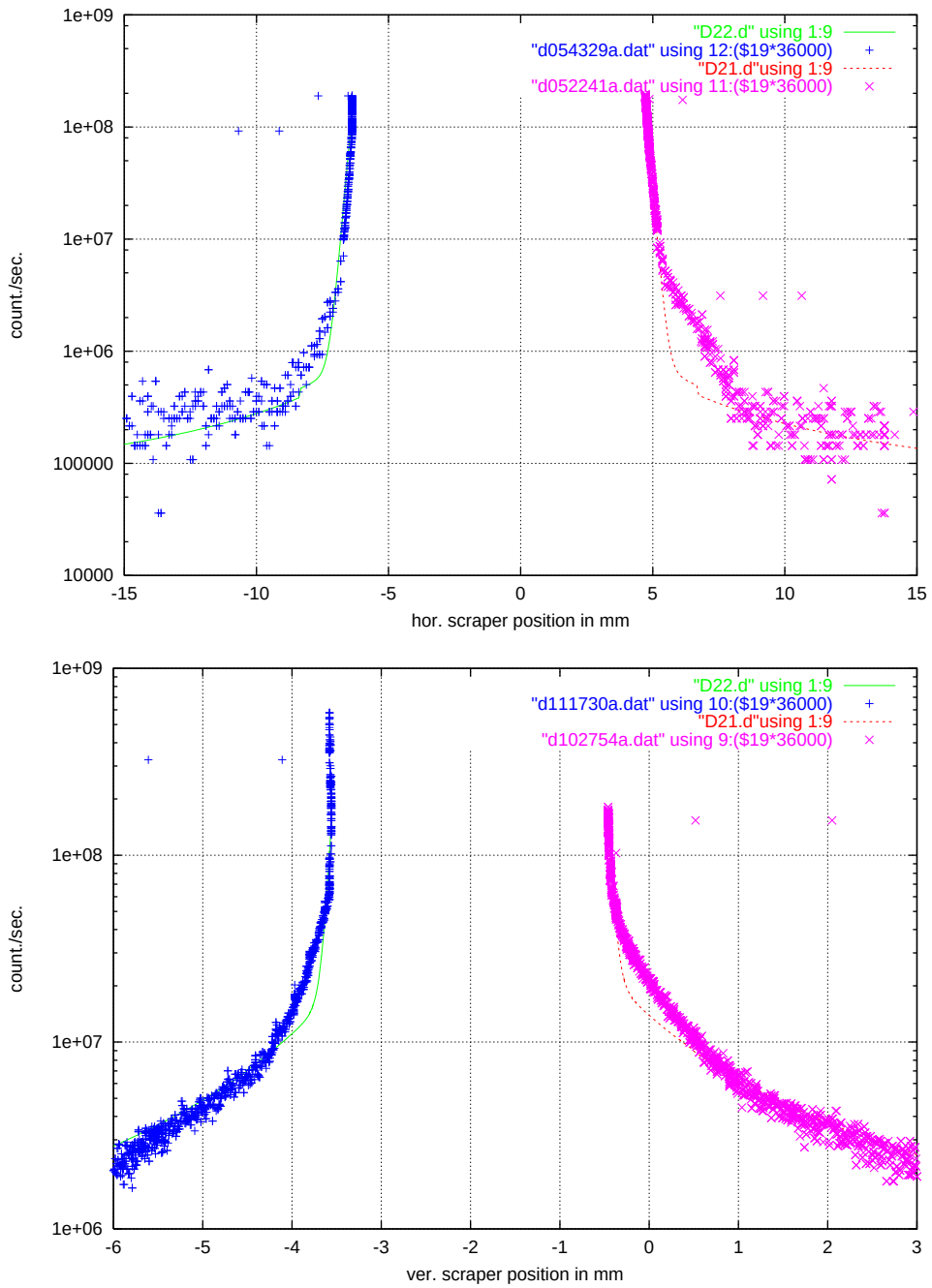

Figure 5.15: *Measured (+,×) and the calculated (line) beam loss rates versus scraper position, with the* 60° *focussing scheme and without beam-beam interaction*

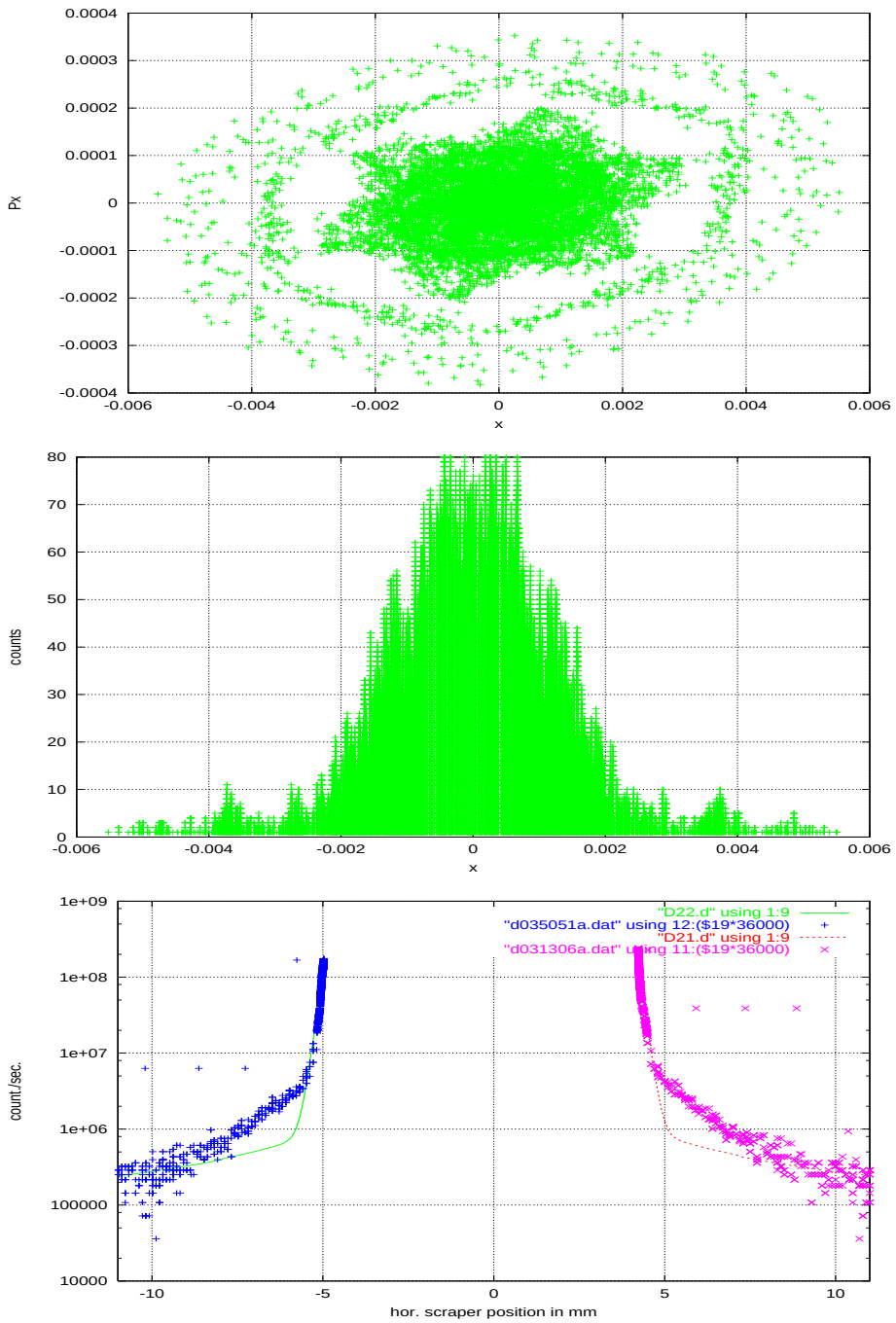

Figure 5.16: *Simulated electron distribution in the phase space* (x, p_x)*(top), the simulated horizontal electron distribution (middle), and the measured data (bottom), for the* $72°$ *focussing scheme without beam-beam interaction,* $\xi_x = \xi_y = 2$*;* $Qx = 0.1668, Qy = 0.2325$*.*

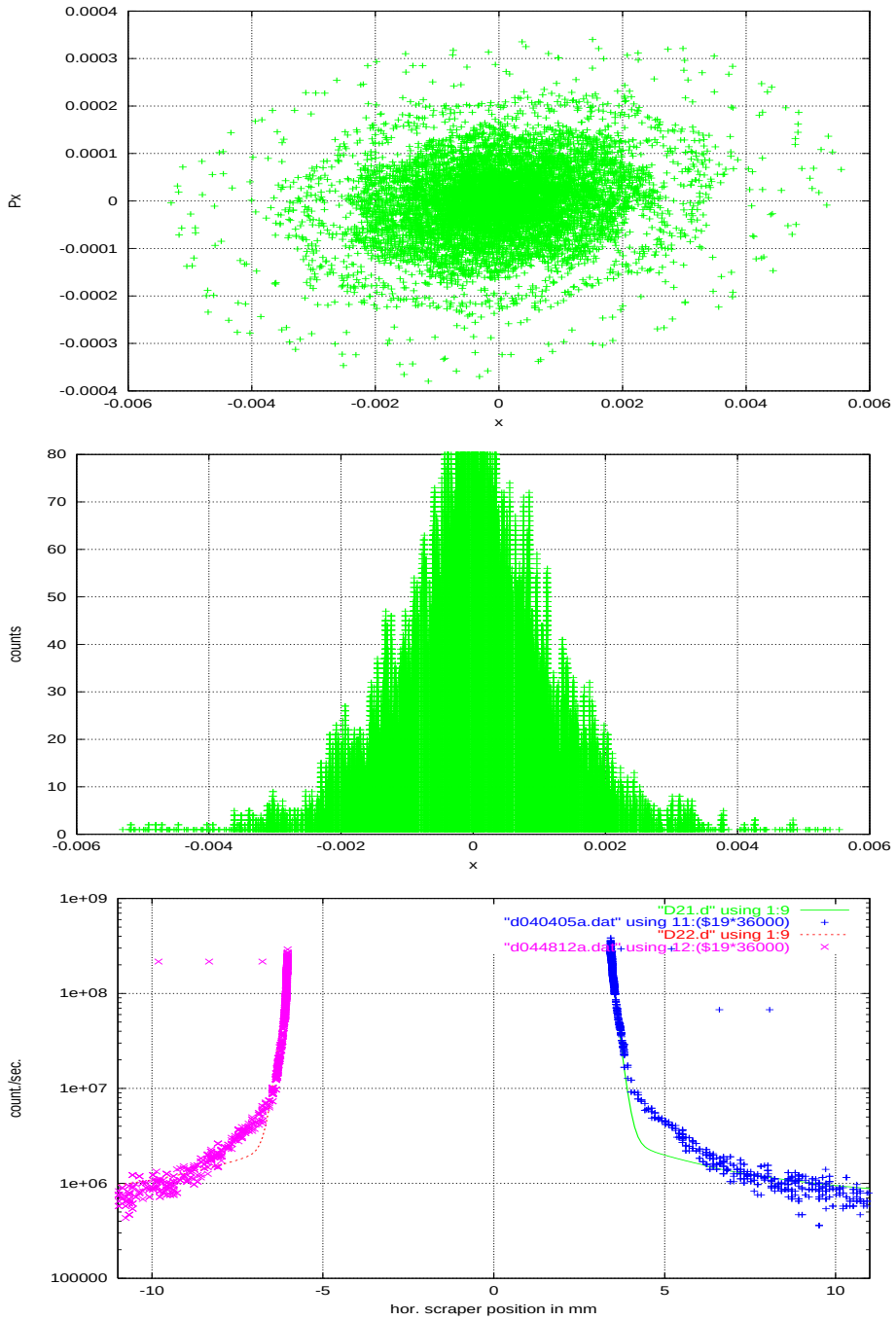

Figure 5.17: *Simulated electron distribution in the phase space* (x, p_x)*(top), the simulated horizontal electron distribution (middle), and the measured data (bottom), for the* $72°$ *focussing scheme with beam-beam interaction,* $\xi_x = \xi_y = 2$*;* $Qx = 0.1416, Qy = 0.2113$*.*

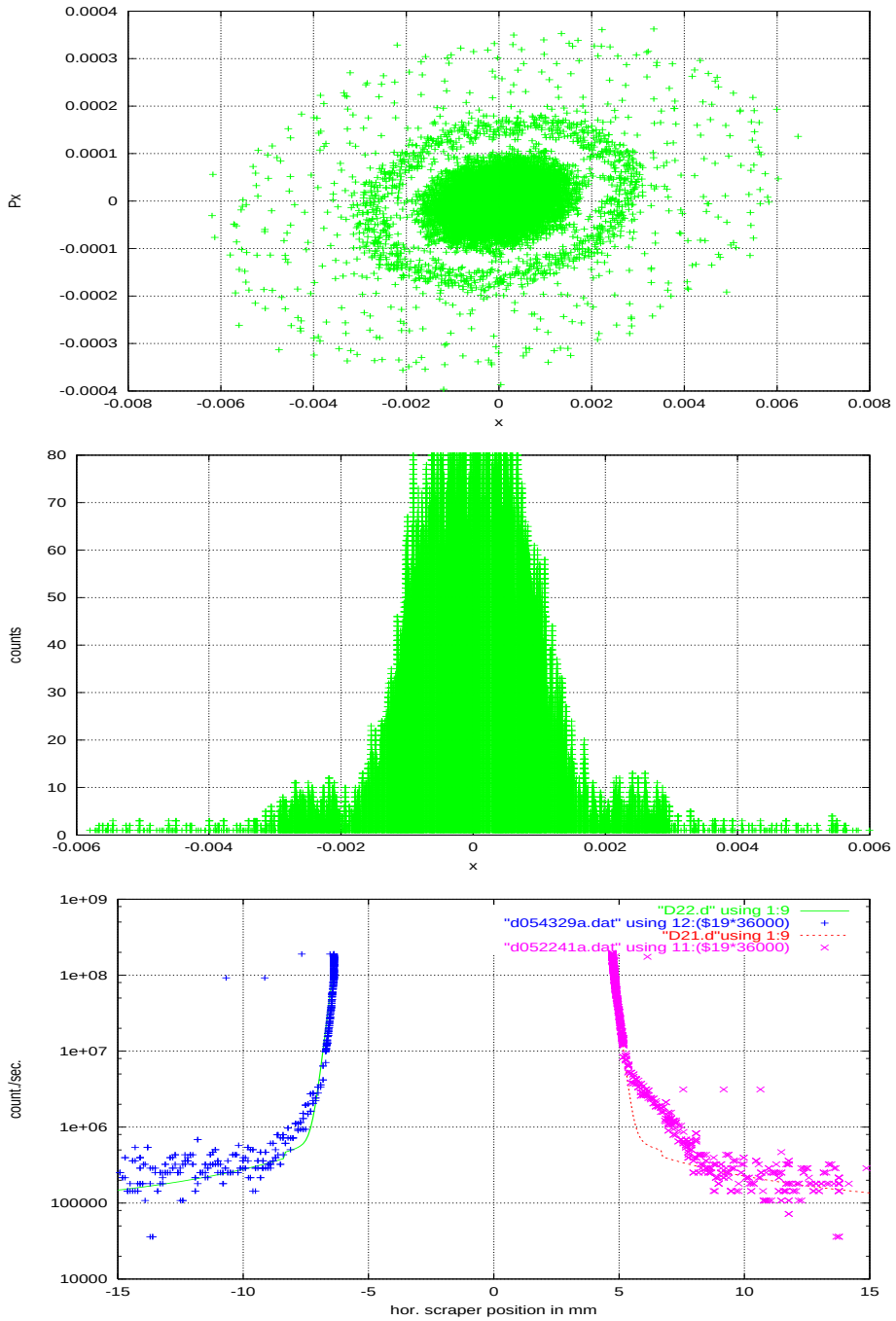

Figure 5.18: *Simulated electron distribution in the phase space* (x, p_x)*(top), the simulated horizontal electron distribution (middle), and the measured data (bottom), for the* 60° *focussing scheme without beam-beam interaction,* $\xi_x = \xi_y = 2$*;* $Qx = 0.1416, Qy = 0.2113$*.*

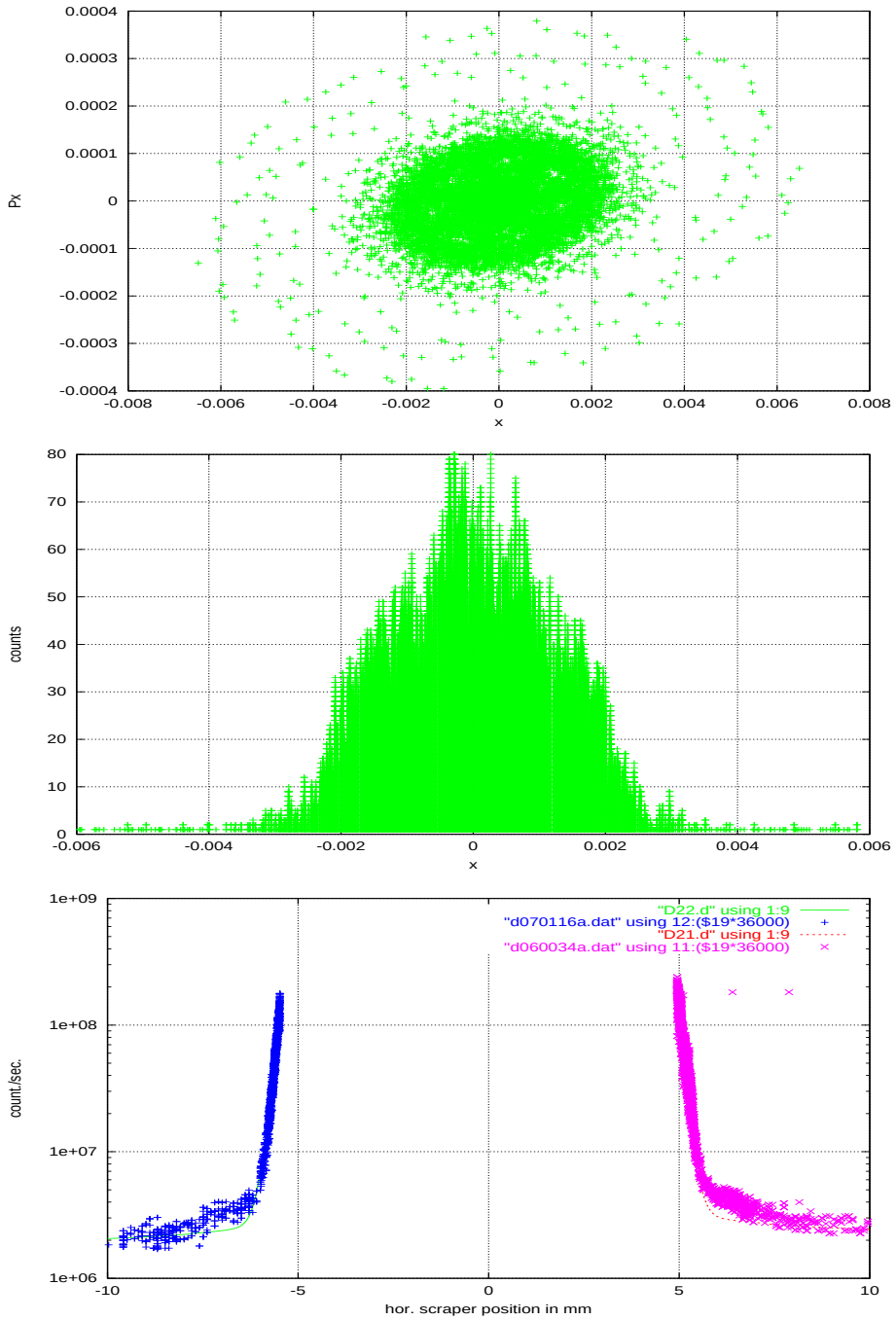

Figure 5.19: *Simulated electron distribution in the phase space* (x, p_x)*(top), the simulated horizontal electron distribution (middle), and the measured data (bottom), for the* $60°$ *focussing scheme with beam-beam interaction,* $\xi_x = \xi_y = 2$*;* $Qx = 0.1395, Qy = 0.2092$*.*

Chapter 6

Estimation of Radiation Background after the Luminosity Upgrade

The non Gaussian tails of the electron distribution can lead to a high synchrotron radiation background in the HERA experiments. The knowledge of the tails and their influence on the synchrotron radiation fan is therefore of importance for the design of the collimation system and the beam pipe of the detectors.

The information about the electron tails obtained from the tail scan measurements is used to form an electron distribution which is used as input in the simulation programs described in chapter 3. This electron distribution and the results of the simulation are treated in this chapter.

6.1 Electron Distribution

A Gaussian core is expected for the electron distribution. The tails of the electron distribution used in the simulation program are formed according to the measured tails. The ratio of tail population to core population in the case of the 72° focussing scheme with beam-beam interaction is used, see fig. 5.6.

Figure 6.1 shows the electron distribution used in the simulation program to investigate the synchrotron radiation background in the H1 detector. The Gaussian electron distribution extends to 6 standard deviations.

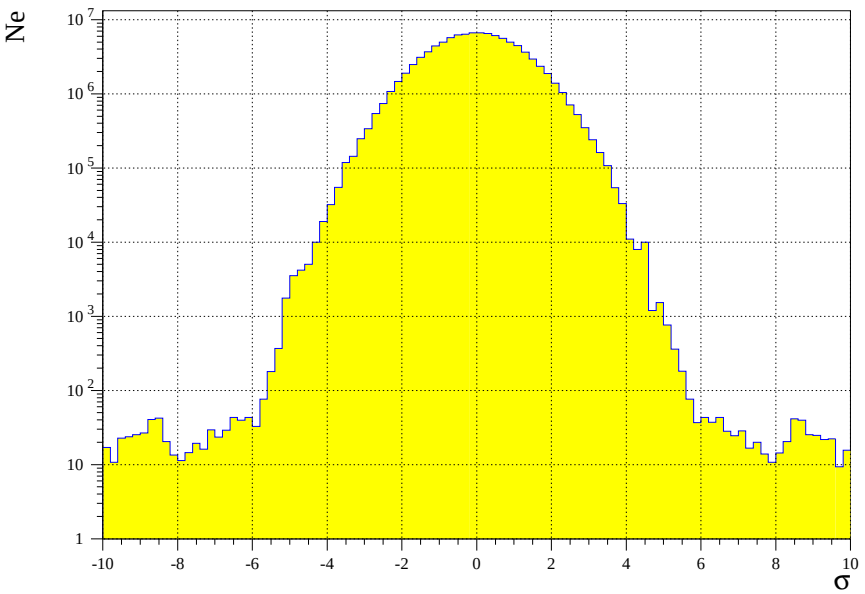

Figure 6.1: *Electron Distribution at the IP in units of standard deviation*

6.2 Radiation Background

The non Gaussian electron tails of the figure 6.1 cause an increase in the number of incident photons on the absorbers compared with the Gaussian distributed case in the table 4.2. In the table 6.1 the increase of the numbers of incident photon as well as the increase of the numbers of backscattered photons are given.

From the table 6.1, it can be concluded that the increase of the numbers of the photons caused by the non Gaussian electron tails is in the order of 10^{12} photons per second for the incident photons and of 10^{9} photons per second for the backscattered photons.

The transverse profile of the synchrotron radiation and the horizontal profile of the critical energy caused by the electron distribution of figure 6.1 at the position of the collimator C5B are shown in the figures 6.2 and 6.3. The figure 6.4 shows the simulated horizontal profile of the radiation fan at the position of the collimator $C5B$.

From the comparison of the figure 4.2, which shows the central beam pipe and the collimation system of the H1 detector designed for a Gaussian electron distribution with the figure 6.4, it can be concluded that the central

Table 6.1: Number of incident and backscattered photons caused by the non Gaussian electron tails, at an electron energy of 30 GeV and 58 mA beam current

Absorber	Distance from the IP (m)	Hor. Width 0f the absorber (cm)	Number of incident photons per second	Number of backscattered photons per second
GM_{inn}	11.00	1.80	$3.73 \cdot 10^{12}$	$1.31 \cdot 10^{9}$
GM_{out}	11.00	5.00	$4.87 \cdot 10^{12}$	$1.71 \cdot 10^{9}$
GN_{inn}	19.00	6.00	$5.29 \cdot 10^{12}$	$1.85 \cdot 10^{9}$
$A24$	24.00	21.00	$1.41 \cdot 10^{13}$	$4.92 \cdot 10^{9}$
GG-Beam *pipe*	3.30	1.50	$7.37 \cdot 10^{11}$	$2.58 \cdot 10^{8}$

pipe and the collimation system are still large enough to pass the direct synchrotron radiation fan in spite of the non Gaussian tails of the electron distribution.

As already mentioned, the number of the backscattered photons in the case of the electron distribution of the figure 6.1 is increased compared with a Gaussian distributed beam. These photons can impinge on the H1 collimation system and scatter in the detector, so that the H1 collimation system is a source of twice backscattered photons in the detector. The simulated hits per bunch crossing and the tolerances for the sensitive components of the H1 detector are shown in the table 6.2. From this table, it can be concluded that the radiation background in the H1 detector after the luminosity upgrade will be well below the tolerances.

Table 6.2: Synchrotron Radiation: Limits and Expected Hit/BC after the Upgrade Project

	CJC Pattern Recognition	BST	FST	CST
Limits	$< 8 Hits/BC$	$< 60 Hits/BC$	$< 60 Hits/BC$	$< 60 Hits/BC$
Expected	$< 3 Hits/BC$	$< 1 Hits/BC$	$< 1 Hits/BC$	$< 1 Hits/BC$

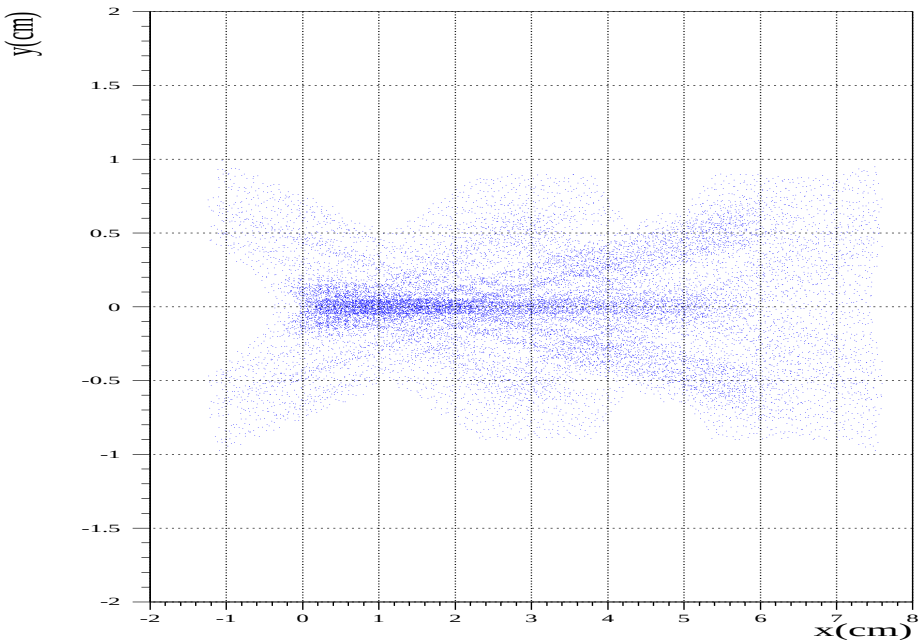

Figure 6.2: *The transverse profile of the synchrotron radiation caused by the electron distribution of the figure 6.1 at the position of the collimator C5B.*

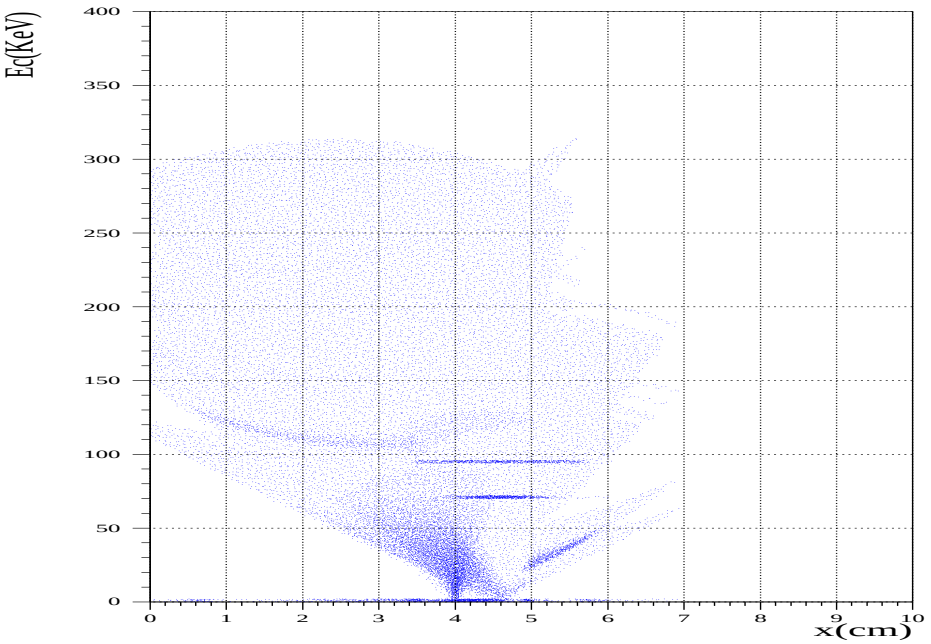

Figure 6.3: *The horizontal profile of the critical energy caused by the electron distribution of the figure 6.1 at the position of the collimator C5B.*

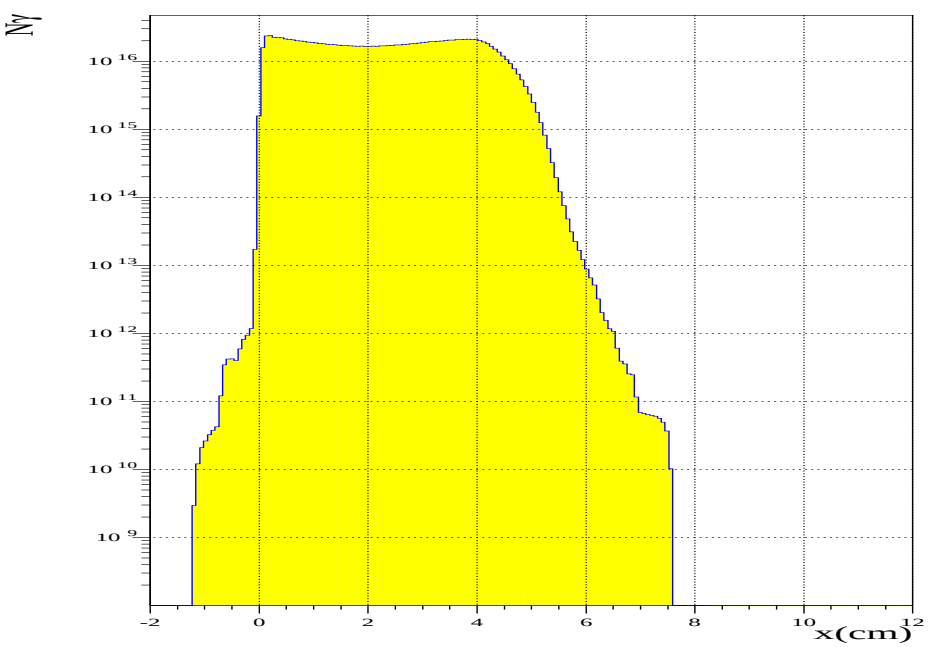

Figure 6.4: *The horizontal profile of the synchrotron radiation caused by the electron distribution of the figure 6.1 at the position of the collimator C5B.*

Chapter 7

Conclusion and Outlook

The planned luminosity upgrade of HERA which enables the experiments to make sensitive tests for QCD and the Standard Model and to look for new physics beyond the Standard Model, includes improved interaction sections for the experiments. The planned interaction regions are designed such that contrary to the present configuration the collimation of direct synchrotron radiation in front of the detectors will no longer be possible. A new enlarged central beam pipe and a collimation system for backscattered synchrotron radiation, which have been designed in the scope of this thesis, will provide the necessary protection of the H1 detector after the upgrade.

Since the electrons in the tail of the electron distribution emit the photons in the edge of the radiation fan, which determines the dimension of the central beam pipe of the H1 detector, the tails of the electron distribution were investigated by tail scan experiments. The tail scan measurements were carried out not only with the current focussing scheme of 60° phase advance per FODO cell in the arcs but also with the upgrade focussing scheme of 72° phase advance per cell. The measurements were taken with and without beam-beam interaction.

Non Gaussian tails were observed in all cases and could be explained by scattering processes and nonlinear resonances. It has been demonstrated, that the scattering of electrons on the residual gas molecules causes non Gaussian tails far away from the main electron distribution, whereas the nonlinear resonances give rise to the tails close to the core of the distribution.

The influence of the nonlinear resonances on the electrons distribution lead to tune-dependent non Gaussian tails next to the distribution core, which can produce high background in the detectors, if they are strongly

populated. This effect has to be taken into account for the choice of the electron tunes after the luminosity upgrade. Also tail scan experiments after the luminosity upgrade could be useful to verify that the chosen tunes do not drive such nonlinear resonances which cause strong electron tails.

Appendix A

The Fokker-Planck Equation

The evolution of the particle density distribution ψ in phase space is used to study the development of a multiparticle beam in an accelerator. Thereby a volume element of the phase space is considered which is small enough to assume a constant particle density distribution within the element.

In a conservative deterministic multiparticle system, the particle trajectory in phase space is completely determined by the initial conditions. The single particle equations of motion are [10]:

$$\frac{dq}{dt} = f(q,p,t)$$

$$\frac{dp}{dt} = g(q,p,t),$$

where q and p are the normalized canonical coordinates.

If the trajectory of the particle in phase space depends only on its *instantaneous physical parameters* and not on its history, a term describing the statistical process has to be added to the equations of motion:

$$\begin{aligned} \frac{dq}{dt} &= f(q,p,t) \\ \frac{dp}{dt} &= g(q,p,t) + \sum_k \varepsilon_k \delta(t - t_k), \end{aligned}$$

where the ε_ks represent the sudden changes in momentum of the particle at the times given by t_k.

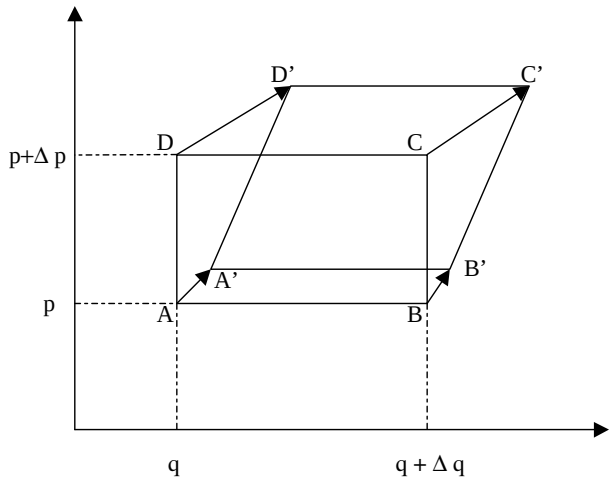

Figure A.1: *A rectangle ABCD containing a distribution of particles is drawn in the phase space at the time t. As particles move in time, the rectangle deforms. At time $t + \Delta t$, the rectangle has deformed into a parallelogram A'B'C'D'.*

Consider a beam distribution in the rectangle $\Delta q \Delta p$ drawn at the time t. At the time $t + \Delta t$, the rectangle deforms into a parallelogram, as shown in figure A.1.

Designating the total sudden changes accumulated in the time increment Δt as E and the probability density of having a particular accumulated kick of magnitude E as $P(E)$, the following equations are valid:

$$\int P(E)dE = 1,$$

$$\int EP(E)dE = 0,$$

$$\int E^2 P(E)dE = \left\langle \dot{N}\varepsilon^2 \right\rangle \Delta t,$$

where $\left\langle \dot{N}\varepsilon^2 \right\rangle$ is the rate of increase of the second momentum with $\dot{N}$ interpreted as the average rate of occurrence of the sudden changes.

The fact that the number of particles found in area $A'B'C'D'$ at the time $t + \Delta t$ has to be accounted for particles in area $ABCD$, yields [10]:

$$\int dEP(E)\psi(q, p - E, t)area(ABCD) = \psi(q+f\Delta t, p+g\Delta t, t+\Delta t)area(A'B'C'D'), \tag{A.1}$$

with

$$area(A'B'C'D') = area(ABCD)\left(1 + \left(\frac{\partial f}{\partial q} + \frac{\partial g}{\partial p}\right)\Delta t\right).$$

The other quantities in equation A.1 can be expanded to first order in Δt to give:

$$\psi(q + f\Delta t, p + g\Delta t, t + \Delta t) = \psi + f\Delta t\frac{\partial \psi}{\partial q} + g\Delta t\frac{\partial \psi}{\partial p} + \Delta t\frac{\partial \psi}{\partial t}$$

and

$$\int dEP(E)\psi(q, p - E, t) = \int dEP(E)\left(\psi - E\frac{\partial \psi}{\partial p} + \frac{E^2}{2}\left(\frac{\partial^2 \psi}{\partial p^2}\right) + ...\right)_{q,p,t}$$

$$= \psi(q, p, t) + \frac{1}{2}\left\langle \dot{N}\varepsilon^2 \right\rangle \Delta t\frac{\partial^2 \psi}{\partial p^2} + ...$$

which, when substituted in equation A.1 yields the *Fokker-Planck equation*:

$$\frac{\partial \psi}{\partial t} + f\frac{\partial \psi}{\partial q} + g\frac{\partial \psi}{\partial p} = -\left(\frac{\partial f}{\partial q} + \frac{\partial g}{\partial p}\right)\psi + \frac{1}{2}\left\langle \dot{N}\varepsilon^2 \right\rangle \frac{\partial^2 \psi}{\partial p^2} + ... \tag{A.2}$$

The damping term of the Fokker-Planck equation is proportional to ψ:

$$\left(\frac{\partial f}{\partial q} + \frac{\partial g}{\partial p}\right)\psi = -2\alpha\psi,$$

where $\alpha = -\frac{1}{2}\left(\frac{\partial f}{\partial q} + \frac{\partial g}{\partial p}\right)$ is called the damping decrement, whereas the diffusion term is proportional to the second derivative of ψ:

$$\frac{1}{2}\left\langle \dot{N}\varepsilon^2 \right\rangle \frac{\partial^2 \psi}{\partial p^2} = D\frac{\partial^2 \psi}{\partial p^2},$$

where $D = \frac{1}{2}\left\langle \dot{N}\varepsilon^2 \right\rangle$ is called the diffusion coefficient.

The electron beam in a storage ring is an example of a multiparticle system under the influence of statistic processes. The sudden changes come from

the emission of quantized synchrotron radiation photons. In the stationary case, where the damping and the excitation are in equilibrium, the motion of the electrons in phase space can be considered as a damped simple harmonic motion:

$$f = \omega p, \qquad g = -\omega q - 2\alpha p.$$

In this case the Fokker-Planck equation A.2 reduces to

$$\frac{\partial \psi}{\partial t} + \omega p \frac{\partial \psi}{\partial q} + (-\omega q - 2\alpha p)\frac{\partial \psi}{\partial p} = -2\alpha\psi + D\frac{\partial^2 \psi}{\partial p^2} \tag{A.3}$$

The equilibrium solution of the Eq. A.3 is a Gaussian distribution:

$$\psi_0(q,p) = \frac{\alpha}{\pi D} \exp\left(\frac{-\alpha}{D}(q^2 + p^2)\right),$$

where the standard widths of q and p are

$$\sigma_p = \sigma_q = \sqrt{\frac{D}{2\alpha}}.$$

"The equilibrium is reached as a result of balancing the damping and the diffusion effects, and the Gaussian distribution is the only distribution that achieves such a balance at all points in the phase space" [10].

Appendix B

Non Gaussian Tails of Electron Distribution

Using the Fourier transform, the probability distribution of discrete stochastic processes can be found, as it is discussed by K. Hirata and K. Yokoya [11]. In the following, this effective method and its application to the tails of the electron distribution are briefly described.

Consider a discrete stochastic process: a dice is thrown with the probability $n_i \ll 1$. According to the die, a number w_i is added to W, which has the initial value $W = 0$). The probability of w obeys a density $f(w)$, which is normalized to unity:

$$\int_{-\infty}^{\infty} dw f(w) = 1.$$

The probability distribution of W, $\rho(W)$, can be obtained from the characteristic function of ρ:

$$\tilde{\rho}(k) = \int_{-\infty}^{\infty} dW \rho(W) e^{ikW} = \left\langle e^{ikW} \right\rangle .$$

The characteristic function is the Fourier transform of the probability density. The gain of W at the i-th step, Δ_i, is either 0 with a probability of $1 - n_i$ or w_i with a probability n_i:

$$W = \sum_i \Delta_i.$$

The characteristic function of Δ_i, $\left\langle e^{ik\Delta_i} \right\rangle$, can be evaluated as:

$$\left\langle e^{ik\Delta_i} \right\rangle = \exp\left[n_i \left(\left\langle e^{ikw} \right\rangle_1 - 1 \right) \right],$$

where the subscript 1 indicates that the expectation is evaluated by the probability f:

$$\left\langle e^{ikw} \right\rangle_1 = \tilde{f}(k) = \int dw e^{ikw} f(w).$$

Since each Δ_i is independent, one obtains:

$$\tilde{\rho}(k) = \prod_i \left\langle e^{ik\Delta_i} \right\rangle_1 = \exp\left[\sum n_i \left(\tilde{f}(k) - 1\right)\right]. \tag{B.1}$$

In order to obtain the transverse distribution of an electron beam which collides with residual gas atoms, the above consideration can be used. Introducing the normalized coordinates,

$$X = \frac{x}{\sigma}, \qquad P = \frac{x'}{\sigma'},$$

where x and x' are the position and slope coordinates, and σ and σ' are the nominal rms beam sizes, the equilibrium beam distribution $\psi_0(X, P)$ is a Gaussian given by:

$$\psi_0(X, P) = \frac{1}{2\pi} \exp\left(-\frac{X^2 + P^2}{2}\right).$$

A collision with a gas atom at the time t_1 causes a transverse kick θ. Since θ is a stochastic variable, the following stochastic equation for $\vec{X} = (X, P)$ is valid:

$$\vec{X}(t) = \vec{X}_0(t) + \vec{X}_f(t), \qquad t > t_1$$

where $\vec{X}_0(t)$ contains the coordinates without the collision, and $\vec{X}_f(t)$ is the contribution of the kick caused by the collision.

The characteristic function of $\psi(\vec{X}, t)$ is

$$\tilde{\psi}(\vec{K}, t) = \left\langle e^{i\vec{K}\vec{X}} \right\rangle = \left\langle e^{i\vec{K}(\vec{X}_0 + \vec{X}_f)} \right\rangle = \tilde{\psi}_0(\vec{K})\tilde{\psi}_f(\vec{K}, t) \tag{B.2}$$

with

$$\tilde{\psi}_0(\vec{K}) = \exp\left[-\frac{K^2}{2}\right].$$

Using the characteristic function $\tilde{f}(u)$ of the one kick probability density $f(\theta)$:

$$\tilde{f}(u) = \int d\theta e^{i\theta u} f(\theta),$$

and evaluating the equilibrium distribution $\tilde{\psi}_f(\vec{K}, t = \infty)$, one obtains

$$\tilde{\psi}_f(\vec{K}) = \exp\left[N \int_0^\infty dt \left(\tilde{f}(Ke^{\alpha t} \sin(\varphi + \omega t)/\sigma') - 1\right)\right], \qquad \text{(B.3)}$$

where N is the number of the kicks (collisions) per unit time, α is the

betatron damping rate, and $\varphi = \tan^{-1}(K_2/K_1)$. Assuming that the number of betatron oscillations is very large during one damping time $1/\alpha$, which is the case in HERA, the betatron oscillation can be replaced by an average over each betatron period. In this case the complex function $\tilde{f}(u)$ simplifies to its real part and one obtains:

$$\tilde{\psi}_f(\vec{K}) = \exp\left(\frac{N}{\alpha} \hat{f}\left(\frac{K}{\sigma'}\right)\right), \qquad \text{(B.4)}$$

with

$$\hat{f} = \frac{2}{\pi} \int_0^1 dx \frac{\Re(\tilde{f}(ux)) - 1}{x \cos x}.$$

In order to obtain the beam distribution $\psi(\vec{X})$, the inverse Fourier transformation has to be performed:

$$\psi(\vec{X}) = \int \frac{d\vec{K}}{(2\pi)^2} e^{-i\vec{K}\vec{X}} \tilde{\psi}_0(\vec{K}) \tilde{\psi}_f(\vec{K}).$$

The beam distribution $\psi(\vec{X})$ has the rotational invariance in the phase space so that it is a function only of the action $I = |\vec{X}|^2/2$:

$$\psi(I) = \int_0^\infty dK K J_0(K\sqrt{2I}) \exp\left[-\frac{K^2}{2} + \frac{N}{\alpha} \hat{f}\left(\frac{K}{\sigma'}\right)\right]. \qquad \text{(B.5)}$$

The projection of ψ to the X axis is given by

$$\varrho(X) = \int dP \psi(X).$$

In the case of the elastic beam-gas scattering, the probability density of one collision $f(\theta)$ is given by:

$$f(\theta) = \frac{1}{\sigma_{tot}} \frac{d\sigma}{d\theta} = \theta_l^2 (\theta^2 + \theta_l^2)^{-\frac{3}{2}},$$

where θ_l is the minimum scattering angle. Note that in opposition to section 1.4, the maximum possible scattering angle due to the aperture limitation is ignored here.

The characteristic function of the one collision probability density $\tilde{f}(u)$ can be expressed by the modified Bessel function K_1 of the first order:

$$\tilde{f}(u) = uK_1(u) \equiv C(u),$$

and $\hat{f}(K/\sigma_0')$ is given by:

$$\hat{f}(K/\sigma_0' = \hat{C}(\frac{\theta_{min}}{\sigma'}K)$$

with

$$\hat{C}(K) = \frac{2}{\pi}\int_0^1 dx \frac{C(Kx)-1}{x\cos x}.$$

Assuming that the number of collisions during one damping time $N/\alpha \ll 1$, which is reasonable in HERA, the distribution of the electron bunch can be approximated as:

$$\psi(\vec{X}) = \psi_0(\vec{X}) + \psi_1(\vec{X}),$$

$$\psi_1(\vec{X}) = \frac{N}{\alpha}\int \frac{d\vec{K}}{(2\pi)^2} e^{-i\vec{K}\vec{X}} e^{-K^2/2} \hat{C}(\frac{\theta_{min}}{\sigma'}K))$$

Since only the tail distribution is interesting here, the factor $e^{-K^2/2}$ is set at unity. After some mathematical manipulations [] one obtains for the tail distribution in the phase space:

$$\psi_1(I) = \frac{N}{\alpha \cdot 2I}\left(1 - \frac{\sqrt{(\sigma_0')^2 2I}}{\sigma_0' 2I + \theta_l}\right). \tag{B.6}$$

Appendix C

Basic Notions of Accelerator Physics

Some basic notion of accelerator physics are briefly explained here. In an ideal circular accelerator, where no field and no alignment errors of the magnets exist, there is a closed curve through the centers of all magnets, on which a particle with the nominal energy moves. This curve is called the *nominal* or *design orbit*.

In a real circular accelerator there exist errors of the magnetic guide fields which give rise to deviations from the nominal orbit. The closed curve goes no longer through the centers of all magnets. This closed curve is called the *closed orbit*.

Due to the quadrupole fields, particles which are not on the closed orbit perform oscillations around it. They are termed *betatron oscillations*. The amplitudes and phases of these oscillations depend on the arrangement and the strength of the quadrupole fields. The largest betatron oscillation amplitude which is still stable in the presence of nonlinear fields is called *dynamic aperture*. The number of betatron oscillations per turn is called *betatron tune*. The set of the horizontal and vertical betatron tunes is the *working point*.

Due to the fact that the strength of the bending and the focussing fields which a particle in an accelerator experiences is momentum dependent, particles with different momenta are bent and focused differently, and have therefore different closed orbits. The difference of the closed orbits devided by the relative momentum deviation is called *dispersion*.

The momentum dependence of the focussing has a further consequence:

particles with a lower momentum are focused stronger whereas particles with a higher momentum are focussed less by the same quadrupole magnet. Therefore particles with different momenta have different betatron tunes. The ratio between the tune deviation and the relative momentum deviation is called the *chromaticity*.

In general the particles are accelerated by radio frequency, RF fields which are generated in cavities. The RF cavities are adjusted, so that a particle with nominal energy experiences the same accelerating voltage each time it passes through the cavities. Particle with higher or lower energy with respect to the nominal energy experience a lower or higher accelerating voltage, called *phase focussing* .

Appendix D

The Measured Data

At the present HERA electron ring, where the focussing scheme of 60° phase advance per FODO cell in the arcs is used, the following tail scan measurements were carried out:

- horizontal and vertical tail scans on a 27.5 GeV positron beam, where the magnets of the proton ring had luminosity conditions but without beam-beam interaction.
- horizontal and vertical tail scan measurements on a 27.5 GeV positron beam under regular luminosity conditions with a proton current of 101.3 mA, i.e. with beam-beam interaction.

In view of the luminosity upgrade project, tail scan experiments were carried out in two cases, where the upgrade focussing scheme of 72° phase advance per FODO cell in the arcs was used:

- horizontal and vertical tail scraping on a 27.5 GeV positron beam. In this case the magnets of the proton ring had luminosity conditions but without beam-beam interaction.
- horizontal and vertical tail scraping on a 27.5 GeV positron beam under luminosity conditions with a proton current of 64.33 mA, i.e. with beam-beam interaction.

For the tail scan experiments, the loss rates of the BLMs $OR32C$ and $OR31C$ as a function of the horizontal and vertical scraper position are shown in the figures D.1 - D.8.

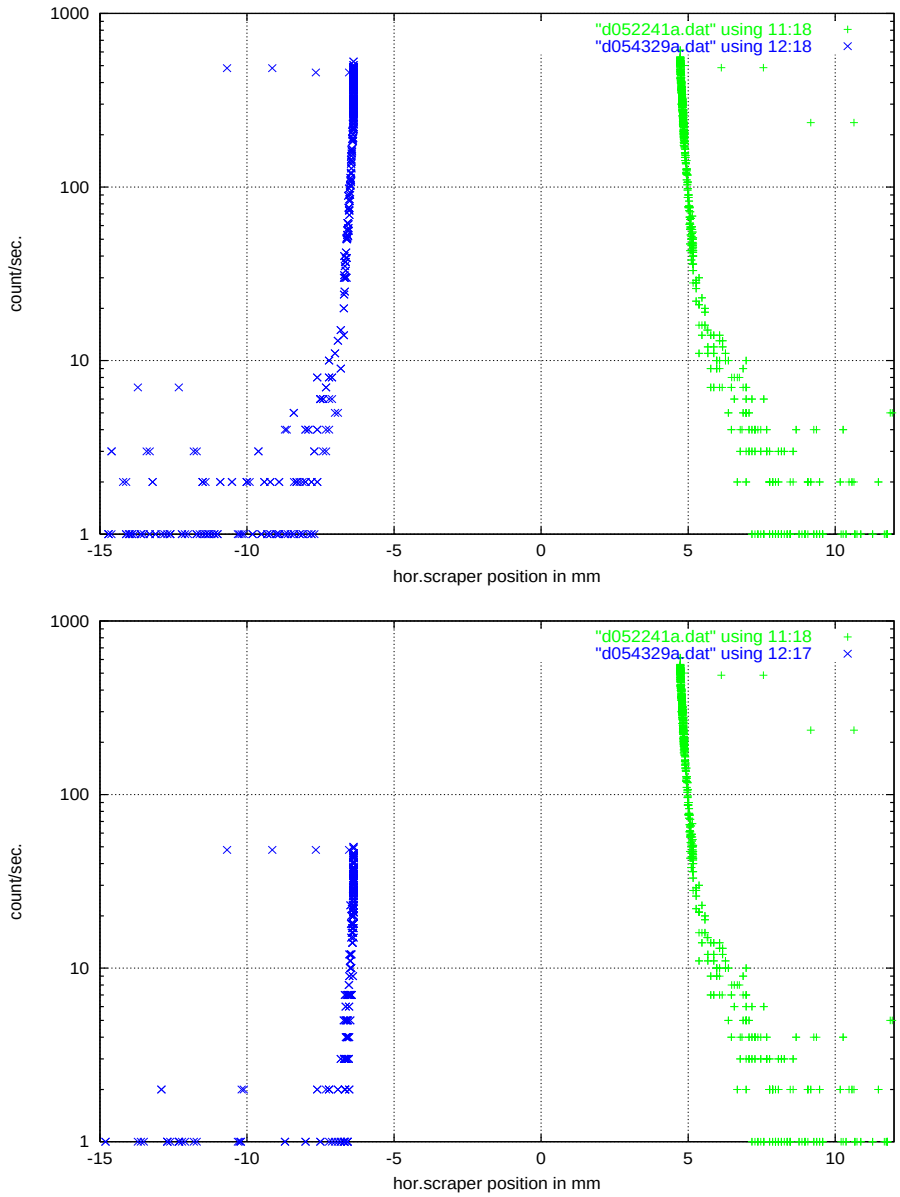

Figure D.1: *Beam loss rates in counts per second versus horizontal scraper position in mm ,with* 60° *focussing scheme and without beam-beam interaction; top: monitor* $OR32C$*, bottom: monitor* $OR31C$

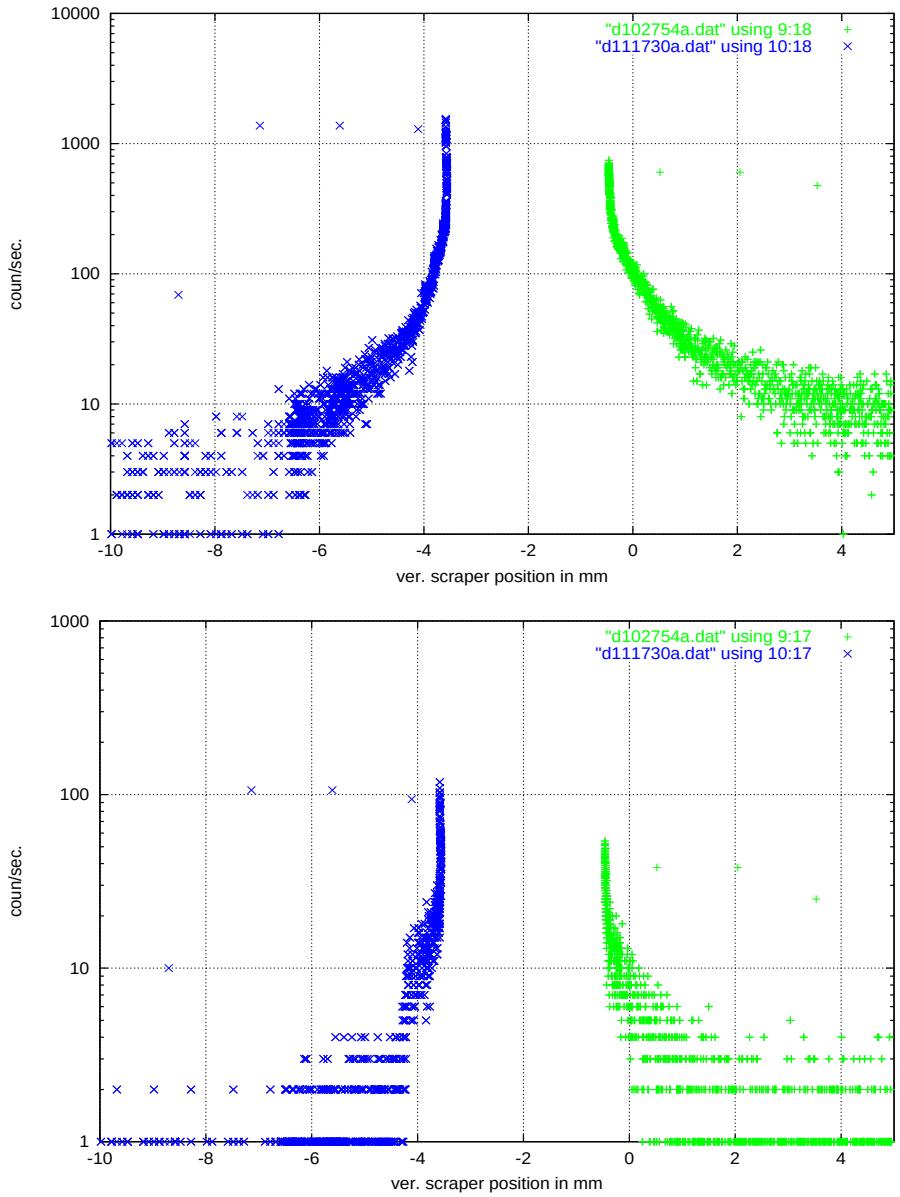

Figure D.2: *Beam loss rates in counts per second versus vertical scraper position in mm, with* $60°$ *focussing scheme and without beam-beam interaction; top: monitor* $OR32C$*, bottom: monitor* $OR31C$

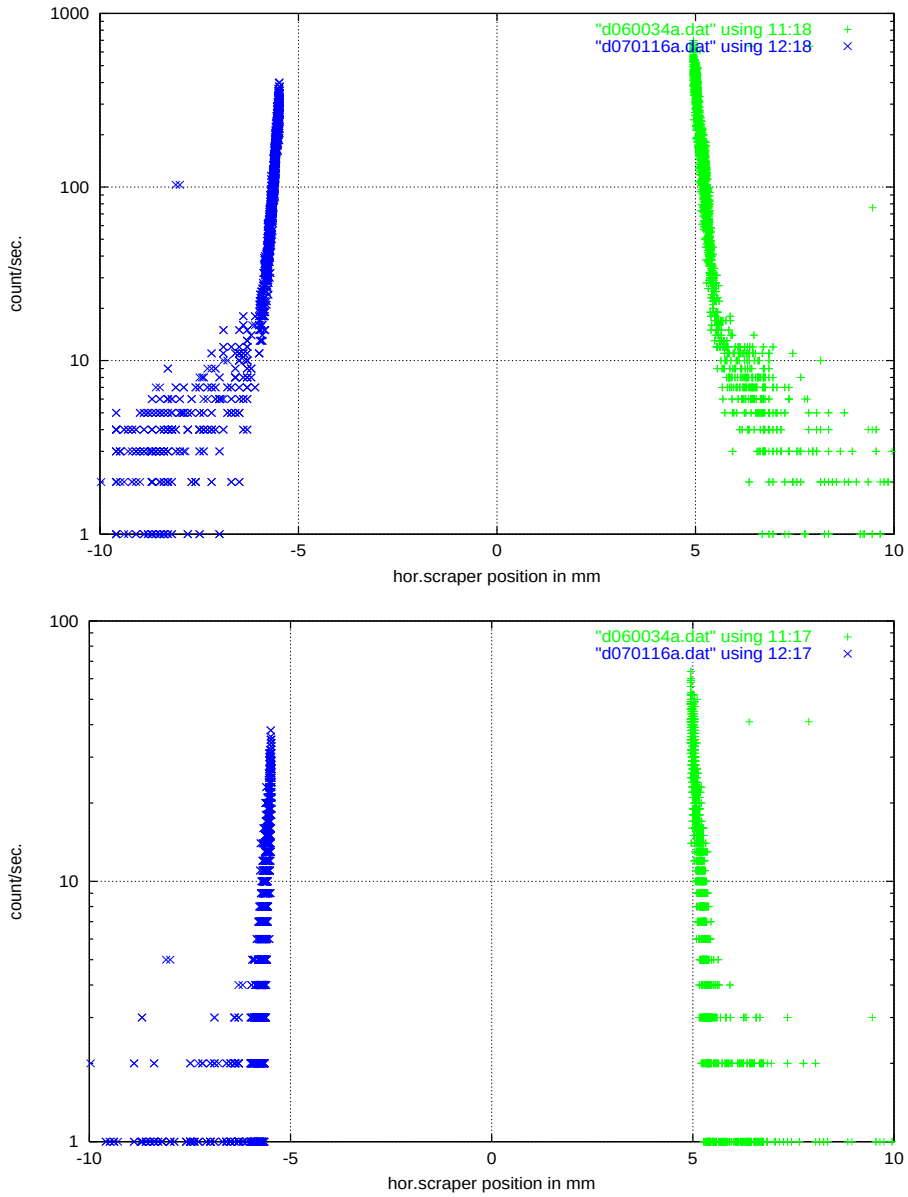

Figure D.3: *Beam loss rates in counts per second versus horizontal scraper position in mm, with* $60°$ *focussing scheme and with beam-beam interaction; top: monitor* $OR32C$*, bottom: monitor* $OR31C$

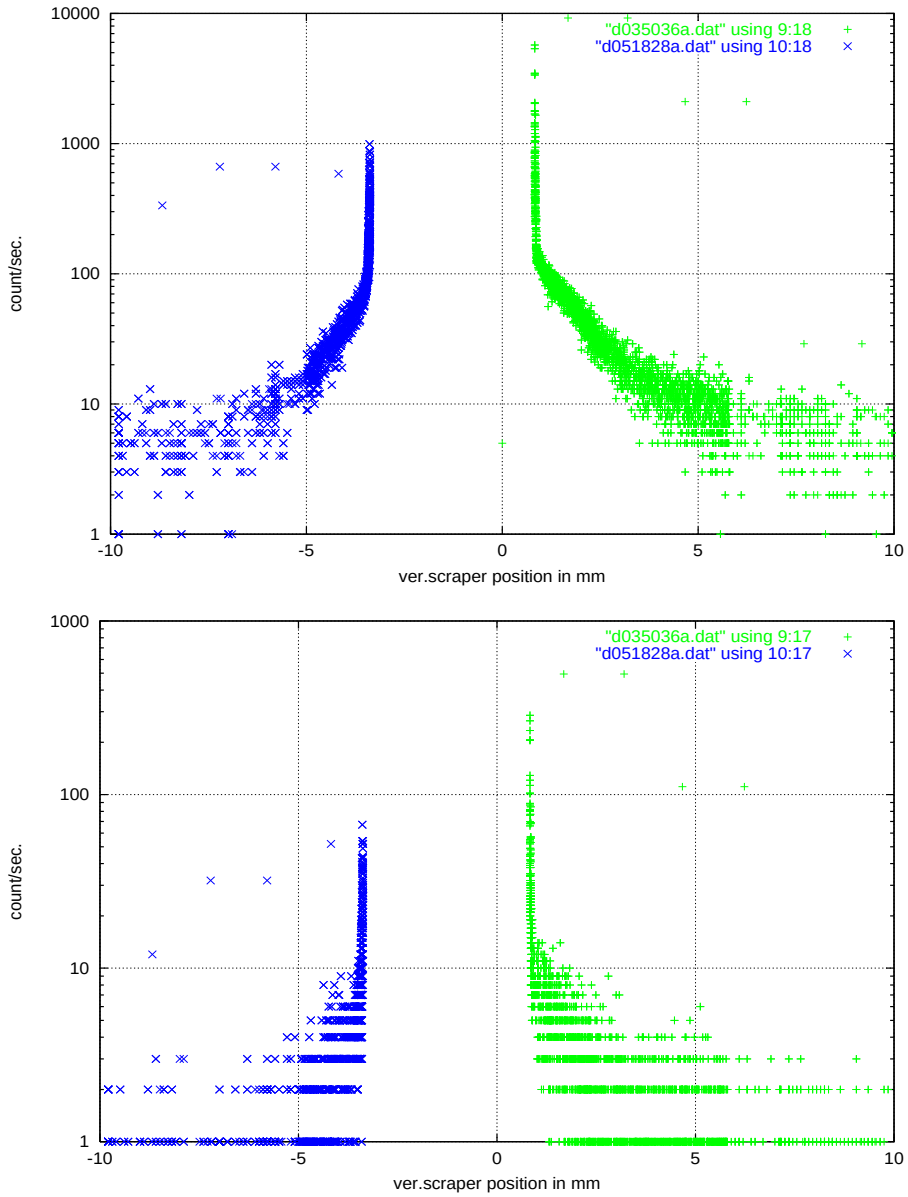

Figure D.4: *Beam loss rates in counts per second versus vertical scraper position in mm, with* $60°$ *focussing scheme and with beam-beam interaction; top: monitor* $OR32C$*, bottom: monitor* $OR31C$

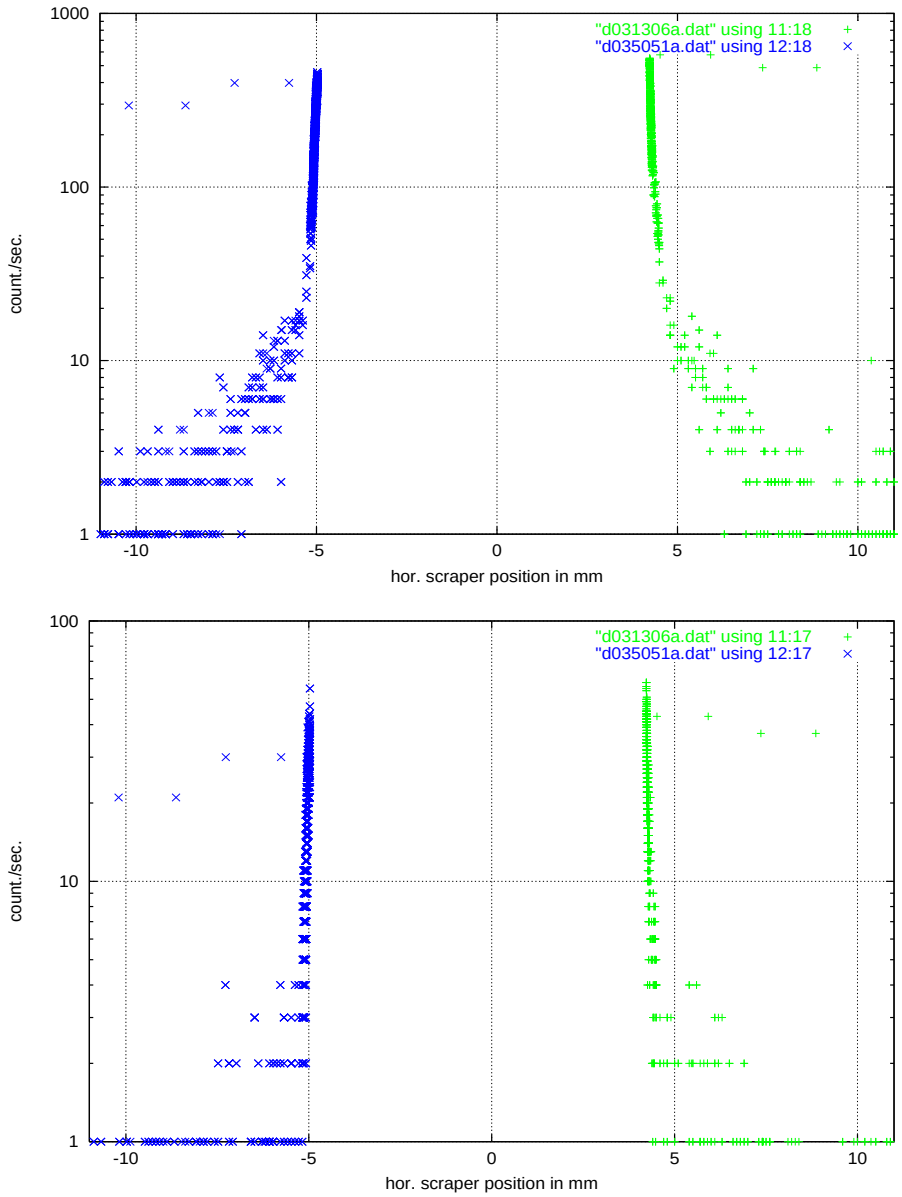

Figure D.5: *Beam loss rates in counts per second versus horizontal scraper position in mm ,with 72° focussing scheme and without beam-beam interaction; tope: monitor OR32C, bottom: monitor OR31C*

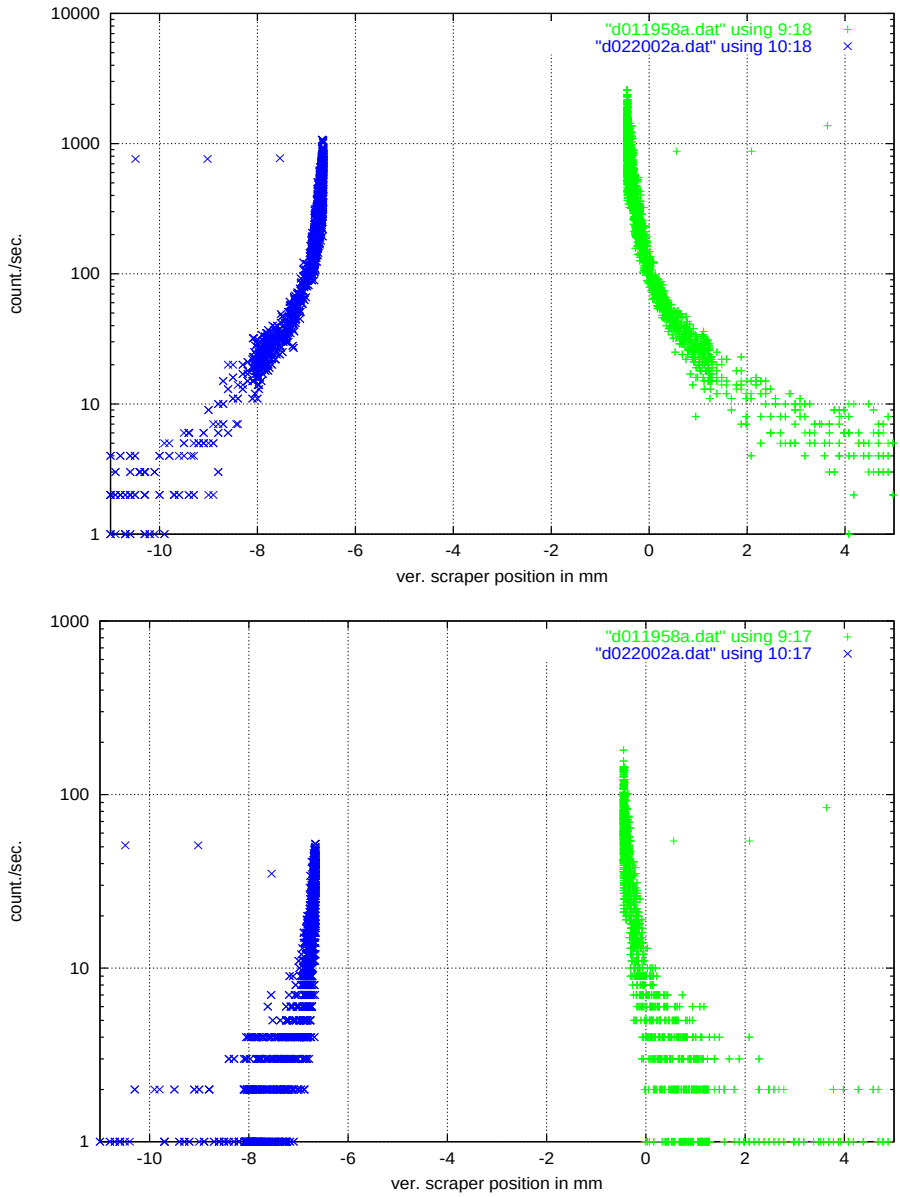

Figure D.6: *Beam loss rates in counts per second versus vertical scraper position in mm, with 72° scheme and without beam-beam interaction; top: monitor OR32C, bottom: monitor OR31C*

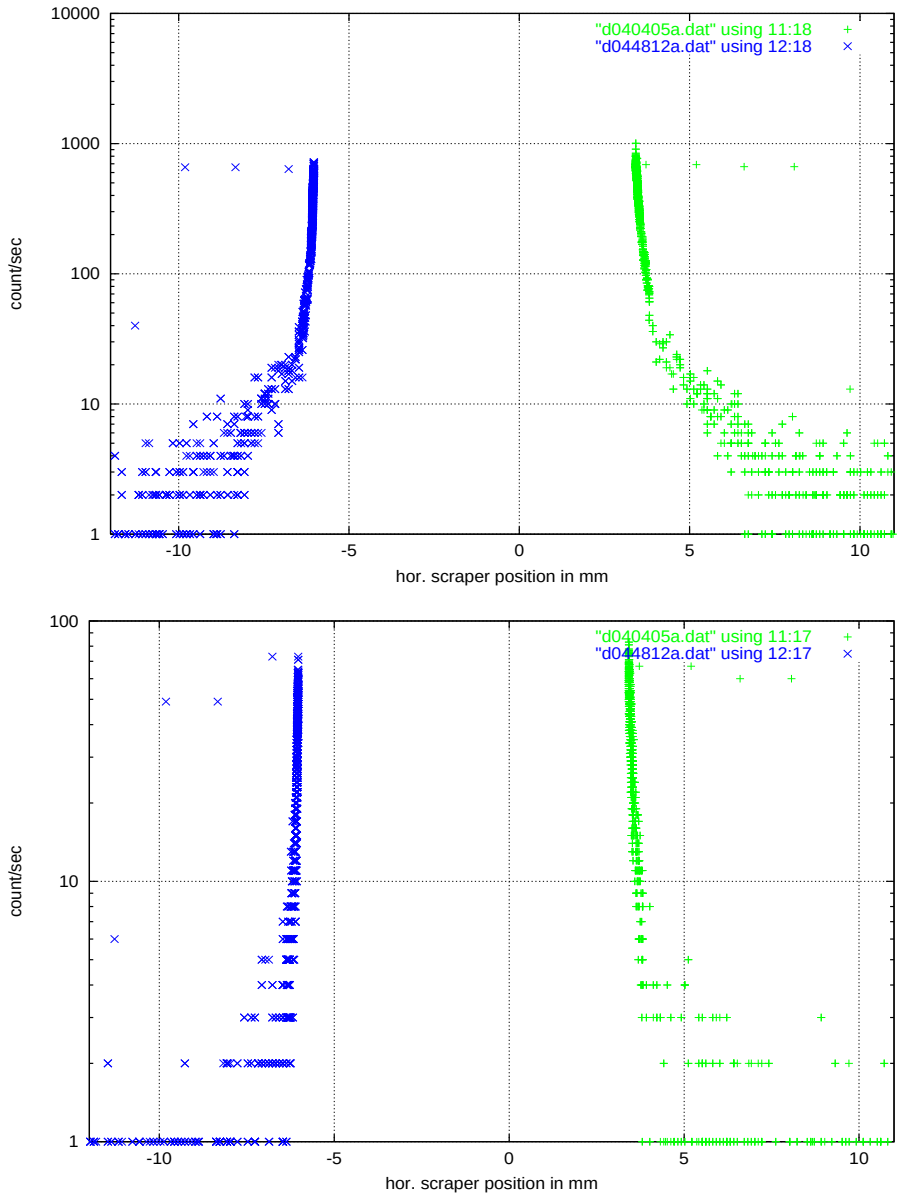

Figure D.7: *Beam loss rates in counts per second versus horizontal scraper position in mm, with 72° focussing scheme and with beam-beam interaction; top: monitor OR32C, bottom: monitor OR31C*

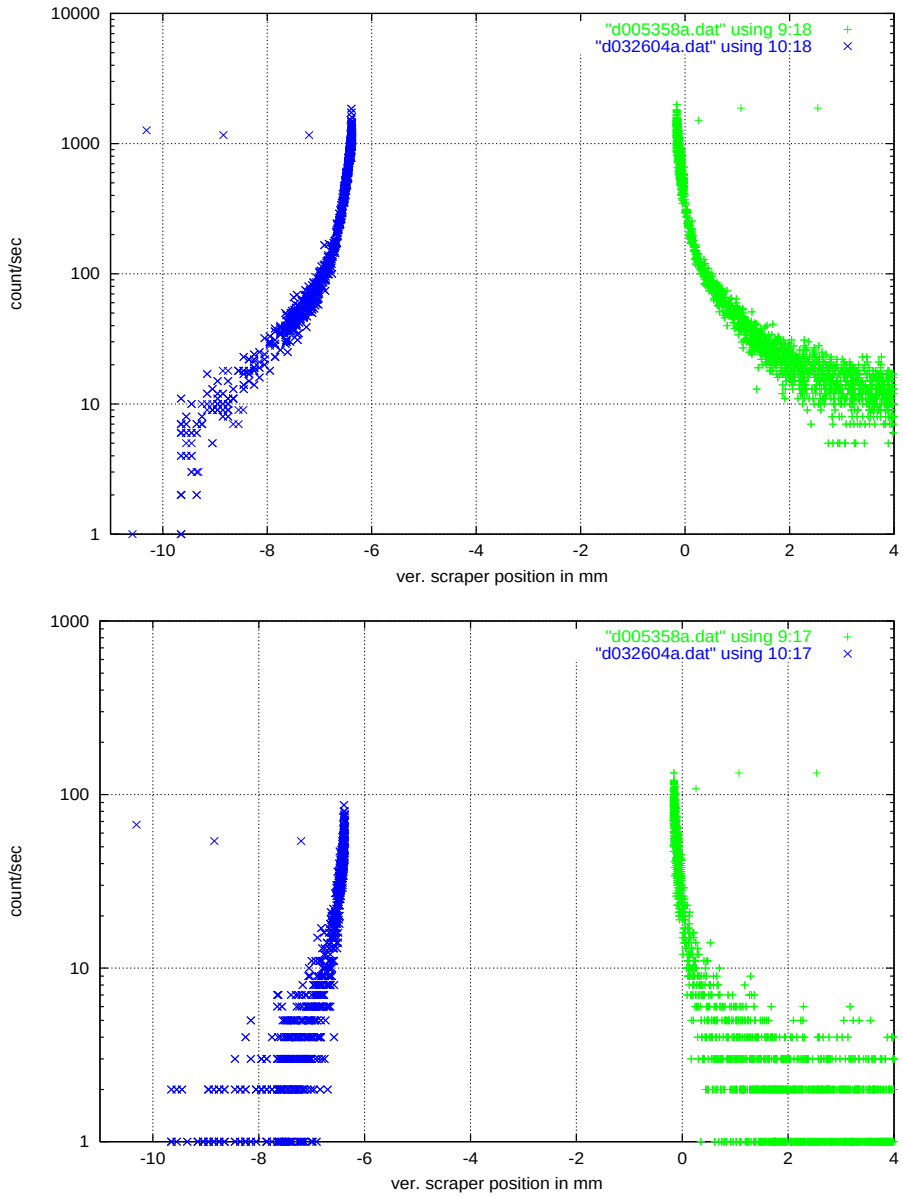

Figure D.8: *Beam loss rates in counts per second versus vertical scraper position in mm, with 72° scheme and with beam-beam interaction; top: monitor OR32C, bottom: monitor OR31C*

Bibliography

[1] R. P. Walker, Radiation Damping, CERN Accelerator School Proceedings, CERN-94-01, 1994

[2] R. P. Walker, Beam Properties, CERN Accelerator School Proceedings, CERN-94-01, 1994

[3] R. P. Walker, Synchrotron Radiation, CERN Accelerator School Proceedings, CERN-94-01, 1994

[4] P. Schmüser, Skript der Vorlesung 'Beschleunigerphysik', 1993

[5] K. Wille, Physik der Teilchenbeschleuniger und Synchrotronstrahlungsquellen, Teubner Studienbücher, 1992

[6] U. Schneekloth (Editor), The HERA Luminosity Upgrade, DESY-HERA-98-05, 1998

[7] M.Seidel, Overview on the HERA Luminosity Upgrade Project, Proc. HERA seminar 99, Report DESY-HERA-99-04, 1999

[8] M. Seidel, HERA Luminositätsupgrade, Proc. HERA seminar 98, Bad Lauterberg, Report DESY-HERA-98-04, 1998

[9] A. Wrulich, Single-Beam Lifetime, CERN Accelerator School Proceedings, CERN-94-01, 1994, p 416

[10] A. W. Chao, In Frontiers of Particle Beams, ed by M. Month, S. Turner,Lect. Notes Phys. Vol.296 p. 51, Springer (1988)

[11] K. Hirata, K. Yokoya, Non-Gaussian Distribution of Electron Beam ddue to Incoherent Stochastic Processes, Particle Accelerators, 1992, Vol. 39, pp.147-158

[12] H. Wiedemann, Particle Accelerator Physics, Springer-Verlag, 1993

[13] H. Wiedemann, Particle Accelerator Physics II, Springer-Verlag, 1995

[14] M. Sands, The Physics of Electron Storage Rings - an Introduction, Report SLAC-121, 1970

[15] M. Seidel, The Proton Collimation System of HERA, DESY 94-103, 1994

[16] H.Bethe, W. Heitler, On the Stopping of Fast Particles and on the Creation of Positive Electrons, Proc. Roy. Soc., A 146, 83, 1934

[17] J. D. Jackson, Klassische Elektrodynamik, Walter de Gruyter

[18] E. Lohrmann, Hochenergiephysik, Teubner Studienbücher, 1986

[19] G. Musiol, J. Ranft, D. Seeliger, Kern- und Elementarteilchenphysik, VCH, 1988

[20] R. D. Kohaupt et al, Physik der Elektronen-Speicherringe, Interner Bericht, DESY H-70/21, 1970

[21] D. D. Pitzl, Abschirmung der HERA-Detektoren gegen Synchrotronstrahlung, Diplomarbeit, Universität Hamburg, 1987

[22] A. Meseck, Upgrade-Projekt: Synchrotronstrahlung im H1-Detektor, Proc. HERA seminar 99, Report DESY-HERA-99-04, 1999

[23] C.Grupen, Teilchendetektoren, B.I., Wissenschaftsverlag, 1993

[24] K. Kleinknecht, Detektoren für Teilchenstrahlung, Teubner Studienbücher, 1984

[25] A. Meseck, The Emittance Measurements at the HERA Electron Ring with and without Beam-Beam Interaction, HERA Machine Studies December 1998, DESY-HERA-99-03, 1999

[26] M. Seidel, Current Dependent Orbit Distortion and Beam-Lifetime Reduction in HERA-e, HERA Machine Studies December 1998, DESY-HERA-99-03, 1999

[27] G. H. Hoffstaetter, The Central Frequency of HERA-e, HERA Machine Studies December 1998, DESY-HERA-99-03, 1999

[28] G. H. Hoffstaetter, New Beam Optics for HERA-e: Theoretical Investigations and Experimental Tests,Proc. HERA seminar 99, Report DESY-HERA-99-04, 1999

[29] A. Meseck, Tail Scan Experiments I at HERA-e, in HERA Accelerator Studies 1999, DESY-HERA-00-02, 2000

[30] A. Meseck, Tail Scan Experiments II at HERA-e, in HERA Accelerator Studies 1999, DESY-HERA-00-02, 2000

[31] G. H. Hoffstaetter, Luminosity and Dynamic Aperture of a 72° HERA-e Optics,in HERA Accelerator Studies 1999, DESY-HERA-00-02, 2000

[32] A. Pauluhn, Stochastic Beam Dynamics in Storage Rings, DESY 93-193, 1993

[33] I. Reichel, Study of the transverse Beam Tails at LEP, PhD Thesis

[34] Y. Alexahin, A Look into Nonlinear Properties of the HERA-e 72/72 Luminosity Upgrade Lattice, DESY-M-99-03, 1999

[35] M. P. Zorzano, Numerical Integration of the Fokker-Planck Equation and Application to Stochastic Beam Dynamics in Storage Rings, PhD Thesis, 1998

[36] H. Grote, F. C. Inselin, MAD User's Reference Manual, Version 8.19, CERN-SL-90-13(Ap), 1996

[37] G. Hoffstaetter, F. Willeke, Electron Dynamics in HERA Luminosity Upgrade Lattice of the Year 2000, Proc. PAC 1999

[38] Y. Alexahin, Closed Orbit Effect on the Equilibrium Emittance in the HERA-e 90/60 Lattice, DESY-HERA-99-02, 1999

[39] T. Chen, J. Irwin, R. H. Siemann, New Physics and Improvements in Beam-Beam Tail Simulation, SLAC-PUB-7193, 1996

[40] W. Decking, J. Byrd, C. Kim, D. Robin, Lifetime Studies at the Advanced Light Source, EPAC 2000 in Wien, 2000

[41] A. Zholentes, W. Decking, Non-Gaussian Beam Tails at the Advanced Light Source, EPAC 2000 in Wien, 2000

[42] J. Le Duff, Current and Current Density Limitations in Existing Electron Storage Rings, Nuc.Ins. and Methods in Phys. A239, 83-101, 1985

[43] Sarau, Priv. Communication

[44] J. A. Wheelers, Influence of Atomic Electrons on Radiation and Pair Production, Phys.Rev.1939, A 55, p 858

[45] A. W. Chao, Evaluation of Beam Distribution Parameters in an Electron Storage Ring, J. Appl. Phys., A 50, p595

[46] M. Bassetti, G. A. Erskin, Closed Expression for the Electrical Field of a Two-Dimensional Gaussian Charge, CERN-ISR-TH-80-06, 1980

[47] H. Mais, C. Mari, Introduction to Beam-Beam Effects, CERN Accelerator School Proceedings, CERN-94-01, 1994

[48] E. Wilson, Non-Linearities and Resonances, CERN Accelerator School Proceedings, CERN-95-06, 1995

[49] E. Wilson, Nonlinear Resonances, CERN Accelerator School Proceedings, CERN-94-01, 1994

[50] G. Guignard, Hamilton Treatment of Synchrobetatron Resonances, CERN Accelerator School Proceedings, CERN-95-06, 1995

[51] D. Pitzl et al, The H1 Silicon Vertex Detector, hep-ex/0002044, submitted to NIM A, 2000

[52] H1 Collabration, Luminosity Measurement in the H1 Experiment at HERA, Warsaw (Poland), July 1996

[53] T.O.Raubenheimer, Emittance Growth due to Beam-Gas Scattering, KEK-Report-92-7, June 1992

[54] W. Schütte, Algorithm for the Lifetime/Loss Measurements with a High Precision DC Transformer, EPAC94, Volume 2,p 1631, 1994

Acknowledgments

I would like to thank Prof. W.Bartel and Dr. F.Willeke for their support and advice as my supervisors. I want to thank Dr. F.Willeke for the possibility to carry out many tail scan experiments and for a careful reading of this manuscript. I would like to thank Prof. W.Bartel for valuable discussions and suggestion and for the careful and fast reading of this manuscript.
I want to thank Prof. P.Schmüser for very careful reading of this thesis and for valuable discussions.
I am grateful to Dr. B.Holzer for his support and advice not only in connection with this thesis.
For valuable discussion and important advice I want to thank Dr. G.Hoffstätter.
I would like to thank Dr. E.Gianfliece-Wendt, Dr. M.Seidel and Dr. W.Decking for help and stimulating discussions.
I want to thank Dr. D.Pitzl for the possibility to use his simulation program and for his support and help in connection with the H1 detector and radiation background.
I would like to thank Mr. B.Sarau for the construction and installation of scrapers in the HERA electron ring.
I want to thank Mr. K.Wittenburg for the installation of BLMs in HERA and for his support and advice in connection with the BLMs.
For the technical support in connection with the design of the H1 beam pipe I also want to thank Mr. K.Gadow.
I would like to thank Dr. M.Lomperski, who wrote the program for the data recoding of the tail scan experiments.
want to thank Prof. E.Lohrmann and Dr. M.Bieler for stimulating discussions about the anti reflection coatings and the radiation absorbers.
I would like to thank Dr.P.Wesolowski, Dr. C.Montag, Dr. F.Brinker, Dr. T.Limberg, Dr. E.Gianfliece, Dr. M.Lomperski, Dr. B.Holzer, Dr. G.Hoffstätter and Dr. M.Bieler for helps and supports during the measuring shifts.
Many thanks to the operation group in BKR for help and support during the measuring shifts.
I want to thank Dr. B.Holzer, Dr. D.Pitzl and Dr. G. Hoffstätter for careful reading of this manuscript.
Further I am grateful to my husband, my parents and my parents-in-law for their encouragements and patience.